Universitat Autònoma de Barcelona

Microscopic description of dielectric thermal transport with memory and nonlocal effects

Lluc Sendra Molins

Microscopic description of dielectric thermal transport with memory and nonlocal effects

Ph.D. thesis

Lluc Sendra Molins

Directors:
Dr. Francesc Xavier Álvarez Calafell
Dr. Juan Camacho Castro

January, 2023

Universitat Autònoma de Barcelona
Physics Department
Physics Ph.D. programme

Als iaios.

«De vegades em sento com un infant al davant d'un tauler d'escacs. Fantàstic, has agafat el peó blanc. Però què fas, ara, per què te'l fiques a la boca? I ara, per què agafes el tauler i l'inclines, perquè totes les peces rodolin per terra?»

– Mircea Cărtărescu. *Solenoide*

Acknowledgements

Since I started my Ph.D. four and a half years ago, I have been lucky to meet many people I didn't know before who have helped me in this process. That is why I want to dedicate a few thanks to each of them.

On the one hand, I thank my thesis supervisors: Xavi and Juan. With two different views of how to approach research and the conception of science, I have extracted many learnings from each. From Juan, I have learned the rigor and the constancy. From Xavi, I have learned the push and the motivation. From both intuition and love for physics. They have shown me their desire to help me become a good scientist. I wonder if they will have succeeded.

On the other hand, I also want to thank Javier for his patience and interest in every query I brought to him from the front office. He makes it possible for physics and mathematics to become a single tool.

And if we talk about mathematics, I would especially like to mention the number 116. I felt lucky to share, within the four walls of our office, the days of my Ph.D. with several people. First, Javi, Axel, and Albert. From a personal perspective, sharing the days with you has been an immense luck, making the hours at the UAB filled with many more things than just physics. I have learned so much from each of you. From a scientific perspective, I would especially like to thank Albert. Talking to you about all the ideas going through our heads, discussing them, and building a common vision of our field is one of the most beautiful processes I have experienced in science. I hope you feel this thesis is also yours.

The 116 has also experienced a new stage, and I feel lucky to have been in both of them. Rosa, Jordi, and now Daniela, I hope I have made the first months of your Ph.D. enjoyable and beautiful. My last ones, indeed, have been this way. And Jordi, I hope I have given you the relief you needed to continue your Ph.D. The group is in good hands!

Finally, in the world of science, I would like to thank Juan for all the conversations apart, some of them in person, which has led us to share, step by step, all the phases from the Master's degree to the culmination of the Ph.D. Thank you very much!

...

Hi havia lletres a banda i banda. Hi eren totes, sense excepció, amb cada un dels seus sons possibles. Una mica més enllà també hi va veure alguns números. «Sort que no hi són tots», va pensar. No es podia imaginar com hi haurien cabut en aquell petit racó del seu pensament. Durant els mesos anteriors, no hi havia entrat gaire. Ja feia temps de l'última vegada.

Rondava entre primers, naturals, enters i molts irracionals. Entre vocals i consonats. Pel camí es va trobar amb lletres que feia anys que no veia. A algunes les saludava i amb d'altres s'hi quedava una estona xerrant. I després seguia rondant.

Al fons, una mica allunyada de la resta, hi havia una petita sala. De dins, en sortia olor de castanyes i moniatos, de canelons i carn d'olla. S'hi va acostar. Va girar el pom i hi va entrar: l'accent era obert. Assegudes al voltant d'una taula hi havia nou lletres. No sabia per què, el seu pensament les havia col·locat apartades en aquella estança. O potser sí que ho sabia. Allà només hi havia la pe, una ema, una hac, una a majúscula, una altra ema, una efa majúscula. També una lletra que no sabia identificar. I juntes, cada una a un costat d'una cantonada de la taula, hi havia dues is. Sí, sí que sabia per què hi eren, allà.

Se les va mirar a totes. No sap quanta estona va estar així. Finalment, va prendre una cadira, es va asseure amb elles i va agafar una castanya. Mentre la feia saltar d'una mà a l'altra per no cremar-se, desistint de pelar-la durant uns instant, se li va dibuixar un somriure.

Declaration of authorship

I, LLUC SENDRA MOLINS, declare that this thesis titled "Microscopic description of dielectric thermal transport with memory and nonlocal effects" and the work presented in it are my own.

LLUC SENDRA MOLINS
Universitat Autònoma de Barcelona, **January 12, 2023**.

Abstract

This thesis provides a new formalism to solve the phonon Boltzmann transport equation for finite Knudsen numbers that supplies a hydrodynamic heat transport equation, the Guyer-Krumhansl equation, similar to the Navier-Stokes equation for general semiconductors. This generalization of Fourier's law is obtained in general cases, from systems dominated by momentum-preserving normal collisions, as is well known, to kinetic materials dominated by resistive collisions, where it captures nonlocal effects. The key feature of our framework is to assume that the nonequilibrium phonon distribution function is described in terms of the heat flux and its first derivatives. We obtain explicit expressions for the nonequilibrium phonon distribution and for the geometry-independent macroscopic parameters as a function of phonon properties that can be calculated from first principles.

This formalism is validated from two different perspectives: theoretical and experimental. From the theoretical perspective, we recover two well-known results in thermal transport. First, we obtain Fourier's law with a general collisions operator. Second, we exactly recover the original results for the Guyer and Krumhansl equation, where it is used that normal collisions dominate. From an experimental point of view, the *ab initio* model predictions agree with a wide range of experiments in silicon and germanium, considering different geometries, temperatures, sizes, or time-dependent and independent situations. Furthermore, in contrast to approaches directly based on the Boltzmann transport equation, the hydrodynamic equation can be solved in arbitrary geometries, thus providing a powerful tool for nanoscale heat modeling at a low computational cost.

Finally, this formalism opens the door to improving its applicability to larger Knudsen numbers by including higher-order derivatives or using effective parameters in the description.

List of publications

- **Hydrodynamic heat transport in dielectric crystals in the collective limit and the drifting/driftless velocity conundrum**
  L. Sendra, A. Beardo, J. Bafaluy, P. Torres, F. X. Álvarez and J. Camacho, *Physical Review B* **106**, 155301 (2022)

- **Hydrodynamic thermal transport in silicon at temperatures ranging from 100 to 300 K**
  A. Beardo, S. Alajlouni, **L. Sendra**, J. Bafaluy, A. Ziabari, Y. Xuan, J. Camacho, A. Shakouri and F. X. Alvarez, *Physical Review B* **105**, 165303 (2022)

- **A General and Predictive Understanding of Thermal Transport from 1D-and 2D-Confined Nanostructures: Theory and Experiment**
  A. Beardo, J. L. Knobloch, **L. Sendra**, J. Bafaluy, T. D. Frazer, W. Chao, J. N. Hernández-Charpak, H. C. Kapteyn, B. Abad, M. M. Murnane, F. X. Álvarez and J. Camacho, *ACS Nano* **15**, 8, 13019-13030 (2021)

- **Observation of Second Sound in a Rapidly Varying Temperature Field in Ge**
  A. Beardo, M. López-Suárez, L. A. Pérez, **L. Sendra**, M. I. Alonso, C. Melis, J. Bafaluy, J. Camacho, L. Colombo, R. Rurali, F. X. Álvarez and J. S. Reparaz, *Science Advances* **7**, 27, eabg4677 (2021)

- **Derivation of a Hydrodynamic Heat Equation from the Phonon Boltzmann Equation for General Semiconductors**
  L. Sendra, A. Beardo, P. Torres, J. Bafaluy, F. X. Álvarez and J. Camacho, *Physical Review B* **103**, L140301 (2021)

- **Geometrical Quasi-ballistic Effects on Thermal Transport in Nanostructured Devices**
  S. Alajlouni, A. Beardo, **L. Sendra**, A. Ziabari, J. Bafaluy, J. Camacho, Y. Xuan, F. X. Álvarez and A. Shakouri, *Nano Research* **14**, 945-952 (2021)

- **Phonon Hydrodynamics in Frequency Domain Thermoreflectance Experiments**
  A. Beardo, M. Hennessy, **L. Sendra**, J. Camacho, T. G. Myers, J. Bafaluy and F. X. Álvarez, *Physical Review B* **101**, 0753033 (2020)

- **Hydrodynamic Heat Transport in Compact and Holey Silicon Thin Films**
  A. Beardo, M. Calvo-Schwarzwälder, J. Camacho, T. G. Myers, P. Torres, **L. Sendra**, F. X. Álvarez and J. Bafaluy, *Physical Review Applied* **11**, 034003 (2019)

Contents

Acknowledgements iv

Declaration of authorship vi

Abstract vii

List of publications viii

Contents ix

1 Introduction 1

2 Thermal transport 8
2.1 Boltzmann transport equation . . . 9
2.1.1 Linearized BTE . . . 11
2.2 BTE solutions . . . 12
2.2.1 Relaxation Time Approximation . . . 12
2.2.2 Callaway's approximation . . . 13
2.2.3 Iterative solution . . . 15
2.2.4 Guyer-Krumhansl's derivation . . . 16
2.2.5 Kinetic-Collective Model (KCM) . . . 19
2.3 Approximation methods . . . 21

3 The Flux derivatives Formalism 23
3.1 General procedure . . . 24
3.2 Fourier's law derivation . . . 27
3.3 Derivation of the Guyer-Krumhansl's equation . . . 30
3.3.1 Energy conservation . . . 33
3.3.2 Non-equilibrium temperature . . . 33
3.3.3 τ_p on Debye's approximation with identical branches and memory effects . . . 35
3.3.4 Debye's approximation and nonlocality . . . 35
3.4 Boundary conditions . . . 36
3.4.1 Perpendicular heat-flux boundary condition. The temperature jump 38
3.4.2 Tangential heat-flux boundary condition. The slip-boundary condition 41
3.5 Conclusions . . . 41

4 Collective limit 43
4.1 Non-equilibrium distribution function . . . 44

4.2 Transport coefficients . . . 46
4.2.1 Relaxation time, τ . . . 46
4.2.2 Thermal conductivity, κ . . . 47
4.2.3 Non-local length, ℓ . . . 47
4.2.4 Time parameter τ_e . . . 48
4.2.5 α-parameter . . . 48
4.2.6 Time parameter τ_p . . . 48
4.3 Second-sound velocity in the collective limit . . . 49
4.3.1 Drifting approximation . . . 50
4.3.2 Driftless approximation . . . 51
4.3.3 Flux derivatives formalism . . . 52
4.3.4 Discussion . . . 54

5 Kinetic limit and intermediate regimes **56**
5.1 Kinetic limit: the Relaxation Time Approximation solution . . . 57
5.2 Intermediate regimes: the Callaway's solution . . . 60

6 Experimental support of the FDF **67**
6.1 Nonlocal effects in silicon . . . 68
6.1.1 Thin films . . . 70
6.1.2 Linear and circular heat sources . . . 77
6.1.3 Heater gratings . . . 83
6.1.4 Frequency domain thermoreflectance . . . 88
6.2 Memory effects in germanium . . . 90
6.2.1 Second sound: frequency domain thermoreflectance without transducer . . . 91
6.3 Other experiments . . . 94
6.4 Summary of the experimental support of the FDF . . . 94

7 Limitations of the model **97**
7.1 Model limitations . . . 97
7.2 Effective parameters modelization . . . 99
7.2.1 Effective nonlocal length . . . 99
7.2.2 Effective slip boundary condition . . . 99

8 Conclusions **102**

Appendix **106**

A *Ab initio* calculations **107**
A.1 Convergence of low-dimension materials . . . 110
A.2 Relaxation times . . . 111

B Symmetrized scattering matrix **112**

C Energy and momentum projection **114**

D Mathematical relations **116**
D.1 Second-order isotropic tensor 116
D.2 Fourth-order isotropic tensor 117

E Alternative derivation of the GKE in the kinetic limit **119**

F Callaway's parameters **123**

G Sources in the model **125**
G.1 Power density source 125
G.2 Momentum rate density source 126

Bibliography **130**

Acronyms **146**

List of Figures

1.1 Schematic representation of normal, Umklapp, and impurity scatterings . . . 4
1.2 Heat flux profile of hydrodynamic and diffusive regimes 4

2.1 Schematic of three-phonon scattering 11
2.2 RTA thermal conductivity 13
2.3 Callaway's-approximation thermal conductivity 15
2.4 MFPs of the KCM for silicon 20
2.5 Thermal conductivity for KCM for different materials 21

3.1 Triangle with the phonon distribution function, transport equations, and boundary conditions 24

4.1 Second sound velocities for graphene in the collective limit 51

5.1 RTA nonlocal length 59
5.2 RTA heat flux relaxation time, τ_p and the α parameter 59
5.3 Callaway and RTA nonlocal length 64
5.4 Callaway and RTA heat flux relaxation time, τ_p and the α parameter 65

6.1 Heat flux profile in a thin film 71
6.2 Effective thermal conductivities for thin films 72
6.3 Effective thermal conductivities for holey thin films 73
6.4 Effective thermal conductivities for thin films compared with the GKE (single scale) and the RTA (multiscale) predictions 74
6.5 Example of an image of a thermoreflectance imaging technique 78
6.6 Fourier's law failure when trying to reproduce the metal heater and the semiconductor substrate 79
6.7 Predicted and experimental results for linear and circular heaters 81
6.8 Predicted and experimental results of the temperature profile for linear and circular heaters at different temperatures and sizes 82
6.9 Scheme of the experimental setup of the EUV scatterometry in confined 1D and 2D nanostructures 83
6.10 Predicted and experimental results for the 1D- and 2D-confined results for different sizes and periodicity 85
6.11 Two time scales thermal decay of thermal grating and the two-box model . . . 87
6.12 Failure of effective Fourier's law in the FDTR experiment 89
6.13 GKE prediction for the FDTR experiment 90
6.14 Time evolution of a heat pulse with or without nonlocal effects 92
6.15 Maxwell-Cattaneo equation prediction of the second sound 93
6.16 Summary of the experimental parameters used to describe the different situations 95

7.1 Phonon distribution function for a circular heater 98
7.2 Effective thermal conductivity for silicon thin films 100
7.3 Effective thermal conductivity for silicon thin films comparing the GKE and the RTA prediction 101

A.1 Convergence study of the parameters 109
A.2 Comparison of the different relaxation times appearing on the transport equations 111

1 Introduction

Nowadays, most of the devices used in our daily life have components based on semiconductors. These materials are used for many applications, going from transistors to photovoltaic or thermoelectric energy sources [1, 2]. Accordingly, the number of transistors in a microprocessor chip has been predicted to be doubled every two years since the 1960s. This exponential behavior is known as Moore's law [3]. However, in recent years, this growth has been limited because of the inefficient thermal response of the current nanostructured devices of silicon [4]. The actual needs of the electronic devices and the improvement of the fabrication techniques result in a high density of electronic components in the chips. These cannot efficiently evacuate the heat, and the device is overheated [5]. This limitation is reached because the typical sizes of these devices have reached the characteristic size of the heat carriers in a semiconductor: the phonons [6]. Then, the size and geometry of the system play a central role in heat transport at these scales.

Heat propagation in solids is due to the atom vibrations and their interactions. This mechanism is correct in principle. Nevertheless, due to the large number of implied particles, it is impossible to study a realistic situation by understanding them individually. Besides that, the heat transport theory was developed by replacing this individual model with a collective oscillations model, where the energy of the solid is distributed to the normal modes of vibration of the whole crystal. Each normal mode can be understood as a wave. The quanta of this lattice vibrational field are referred to as

a phonon [7]. The theory around these quasi-particles was developed to simplify thermal transport [7, 8].

Historically, the macroscopic theory to model the behavior of phonons in dielectrics is Fourier's law. It was proposed by Joseph Fourier 200 years ago [9], and it predicts that heat is moving diffusively to the lower-temperature positions:

$$\vec{q}(\vec{r},t) = -\kappa\vec{\nabla}T(\vec{r},t), \tag{1.1}$$

where κ is the thermal conductivity, $T(\vec{r},t)$ is the local temperature, and $\vec{q}(\vec{r},t)$ is the heat flux. Combining Fourier's law with energy conservation provides the well-known diffusion equation for heat. The heat flux can be expressed in terms of phonon properties as $\vec{q}(\vec{r},t) \equiv \int \hbar\omega_\lambda \vec{v}_\lambda f_\lambda(\vec{r},t)d\lambda$. The λ sub-index denotes the mode of the phonon with a certain wavevector and branch. ω_λ is the frequency of the λ-mode and $\vec{v}_\lambda$ is the group velocity defined as $\vec{v}_\lambda \equiv \frac{\partial\omega_\lambda}{\partial k}$, with k the wavevector. Finally, $f_\lambda(\vec{r},t)$ is the phonon population of the λ-mode. For the seek of simplicity, from now on, the spatial and temporal dependence of the variables will not be explicitly written ($\vec{q}(\vec{r},t) = \vec{q}$, $T(\vec{r},t) = T$, $f_\lambda(\vec{r},t) = f_\lambda$, ...).

Since Fourier's law predicts a diffusive behavior, it occurs that it does not take into account the interaction of the phonons with the boundaries. In the last decade, the improvement of experimental techniques has allowed observing the thermal response of nanostructured devices [10–21]. At large scales, boundaries have no relevant effect. However, a heat flux reduction appears when system sizes of the order of the characteristic sizes of phonons are reached. This phenomenon is observed, for example, in thin films of silicon, where a transition from Fourier's law to a reduced heat flux is experimentally demonstrated [22–25].

The primary tool of the field to understand this non-Fourier behavior is the Boltzmann transport equation (BTE) [26], which was derived for phonons by Peierls [8]:

$$\frac{\partial f_\lambda}{\partial t} + \vec{v}_\lambda \cdot \vec{\nabla} f_\lambda = C(f_\lambda). \tag{1.2}$$

The left-hand side of Equation (1.2) is called the drift operator $D(f_\lambda)$ and contains the phonon velocity $\vec{v}_\lambda$. The right-hand side is the collision operator $C(f_\lambda)$, which accounts for the collisions of phonons among them and with other elements, such as impurities or crystal defects. This operator is generally a nonlinear function of phonon population, making it very

difficult to handle. Fortunately, many situations address small temperature variations so that it can be linearized [7, 8], and Equation (1.2) becomes a linear equation of f_λ. This linearity allows for building a Hilbert space for the solutions, which will be very useful. From now on, when the BTE is referred to, the linearized version of Equation (1.2) is considered. The BTE is an equation that gives information about the phonon population and relates it with its temporal and spatial derivatives. Solving this equation analytically is not possible except under some approximations (for example, Callaway's approximations [27–29] or the Relaxation Time Approximation (RTA) [30–36], which will be shown in Section 2.2).

Due to its complexity, large efforts have been made to solve it. Several numerical approaches have been tried to do it in the last years, taking advantage of the recent computational improvements. Some have done it by directly solving the equation for simple geometries [35–44] or using Monte Carlo simulations to reproduce it [45–50]. Despite these advances, the computational cost, the complexity of the collision operator, and the difficulty in implementing physical boundary conditions require alternative approaches to solve the problem in complex geometries.

Accordingly, several theories have been developed in recent years to simplify the problem. Some address it by using effective thermal conductivities or boundary resistances in Fourier's law [14, 16, 18]. Other models are based on suppressing the contribution of specific phonon modes to the thermal properties of the system. Usually, the suppressed phonons are those with a mean free path (MFP) smaller than the experimental size of the system [13, 14, 18, 51]. These models are developed for some particular cases and are not predictive for complex geometries.

Nevertheless, under some situations, the non-Fourier behavior is associated with phonon hydrodynamics [28, 29, 36, 42, 43, 52–67]. This phenomenon is usually connected with phonon collisions of the material, as follows. In a molecular flow, all collisions conserve momentum. However, for phonon flow, it may occur that phonon-phonon collisions do not conserve it. Then, the collisions are classified into two kinds: momentum-preserving collisions, named normal collisions; and momentum-destroying ones, named resistive collisions. Figure 1.1 shows that for normal collisions, the resulting wavevector of the generated phonon is the sum of the

colliding phonons. However, the resulting wavevector does not conserve momentum for the Umklapp (intrinsic resistive collisions) or the impurity scattering, which are resistive. In particular, for the Umklapp case, the propagation direction is reversed, thus causing thermal resistance.

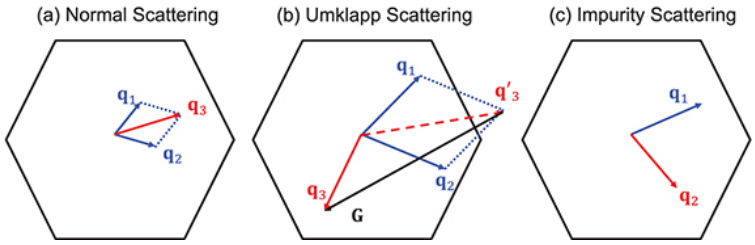

Figure 1.1: Schematic representation of the (a) normal, (b) Umklapp, and (c) impurity scatterings in the reciprocal space. The hexagon represents the first Brillouin zone, and the **q** denotes the wavevector. *Image extracted from [68].*

Hydrodynamic heat transport is expected to occur when normal collisions dominate in front of resistive collisions, i.e., when the crystal momentum is conserved. The name hydrodynamic is due to the analogy with fluids, and this is also the reason why usually the dominance of normal collisions is required: in fluid dynamics, the collisions between particles conserve momentum. When momentum is essentially conserved, the heat flux profile resembles the velocity profile in fluids, recovering Poiseuille-like flow, as seen in Figure 1.2. The collective (or Ziman) regime is where normal collisions dominate. The conditions for this regime are rare to be satisfied. On the one hand, when the temperature is decreased, the resistive collisions are suppressed; on the other hand, it also occurs that there are not enough normal collisions. These narrow conditions have made historically considering hydrodynamic phonon transport not relevant for practical applications [68].

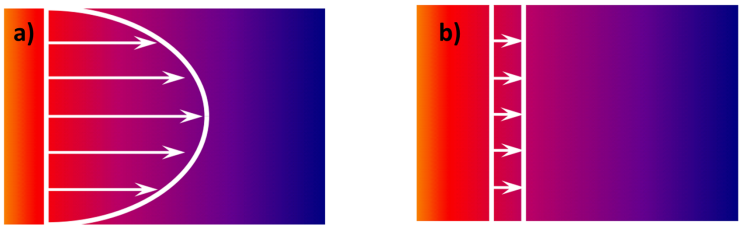

Figure 1.2: Heat flux profile of (a) hydrodynamic and (b) diffusive regimes. The hydrodynamic flux profile recovers the Poiseuille-like shape obtained in fluids with the Navier-Stokes equation. *Image extracted from [54].*

Some models predicting hydrodynamic thermal transport have been developed in the collective regime. One of the most relevant is the generalization of Fourier's law proposed in [43] considering the theory of relaxons [41]. This theory introduces a basis for the BTE's solutions determined by the collision operator's eigenvectors [41, 69]. Therefore, the BTE is expressed with the relaxons' basis instead of the

phonons' basis, which are the eigenstates of the drift operator. This generalization of Fourier's law predicts the emergence of hydrodynamic phenomena, like nonlocal and memory effects. However, these are only predicted in materials like graphite or diamond, where normal collisions dominate. The presence of hydrodynamic effects in materials like silicon or germanium, where resistive collisions are dominant, is absent in this theory.

Guyer and Krumhansl, in 1966, derived a different equation, the so-called Guyer-Krumhansl equation (GKE), which predicts nonlocal and memory effects for materials where normal collisions dominate [52], as in the relaxons development. In this case, the collision operator is separated into the normal and the resistive collision operator. Then, the BTE is expressed in terms of the basis that diagonalizes the normal collision operator. Thus, it naturally imposes conservation laws like energy and momentum. The resulting equation, the GKE, is

$$\vec{q} = -\kappa\vec{\nabla}T - \tau\frac{\partial\vec{q}}{\partial t} + \ell^2\left(\nabla^2\vec{q} + 2\vec{\nabla}\left(\vec{\nabla}\cdot\vec{q}\right)\right). \tag{1.3}$$

where κ is the thermal conductivity, τ is the heat flux relaxation time, and ℓ is the nonlocal length. This equation is a generalization of Fourier's law since it includes memory ($\tau\partial_t\vec{q}$) and nonlocal ($\ell^2(\nabla^2\vec{q} + 2\vec{\nabla}\vec{\nabla}\cdot\vec{q})$) effects.

Let us note the similarity of Equation (1.3) with the Navier-Stokes equation (NSE) for fluids. As in the NSE, the nonlocal effects introduce a viscous-like term that reduces the heat flux near the boundaries. This effect occurs when characteristic sizes of an experiment are reduced to the order of the nonlocal length. Nevertheless, when we consider large sizes, nonlocal effects are negligible, and in a stationary situation, the GKE recovers Fourier's law, as is expected.

As mentioned, these two models [43, 52] do not predict hydrodynamic effects for resistive-dominated (or kinetic) materials. Remarkably, this is at odds with recent experimental results, where non-Fourier behavior observed in kinetic materials can be explained using the GKE, such as in InGaAs [58], silicon [57, 59, 62–65, 67, 70], or germanium [66]. Therefore, in contrast to what is expected, these kinetic materials obey the hydrodynamic equation (Equation (1.3)).

To explain this inconsistency, the kinetic-collective model (KCM), developed by Álvarez and colleagues [71–73], aims to generalize the GKE for kinetic materials. This is achieved

by obtaining microscopic expressions for the parameters of Equation (1.3) in both the kinetic and collective limits and interpolating them to obtain the parameters in general situations. The main drawback of this model is that the parameters are not directly obtained from the BTE. However, they are predictive for a wide range of kinetic materials [58, 59, 62–67, 70]. This predictability allows concluding that the GKE (or hydrodynamic equation) is applicable for materials with no normal collision dominance, in contrast to common belief.

This Ph.D. thesis is motivated by the need to derive the GKE from the BTE for general semiconductors and kinetic materials in particular. This would provide microscopic formulations for the hydrodynamic behavior observed in kinetic materials, in contrast to previous formalisms, where hydrodynamic thermal transport is obtained only for collective materials [43, 52, 74]. Furthermore, it would allow connecting the mesoscopic description with the microscopic description since the BTE is solved and, thus, the distribution function of the phonons. Besides, the expressions for the parameters would be obtained from first principles. In addition, using the kinetic theory from the BTE would also provide consistent boundary conditions for describing the system's thermal behavior.

The tradition of the Statistical Physics group of the Universitat Autònoma de Barcelona inspires the perspective to address this thermal transport problem in this thesis. This group, led by David Jou, developed the Extended irreversible thermodynamics (EIT) theory [75]. This theory aims to simplify transport processes by using mesoscopic descriptions of the system but guaranteeing fundamental properties, such as energy conservation or the second principle of thermodynamics. Keeping this in mind, the derivation of the GKE proposed in this thesis tries to match the mesoscopic and kinetic points of view.

The thesis is organized as follows. Chapter 2 introduces the most relevant theories to address phonon hydrodynamics in the thermal transport field. We also present some theoretical background needed to understand the rest of the thesis chapters. In Chapter 3, we develop the Flux derivatives formalism (FDF), which is the main contribution of the present thesis to the thermal transport field. Through the FDF, we present the derivation of the GKE for general semiconductors with the corresponding expressions for the transport coefficients, which can be calculated using *ab initio* techniques.

In Chapter 4, we apply the FDF to the collective limit and compare its results with previous ones and, in particular, recover the original results by Guyer and Krumhansl [52]. In Chapter 5, we apply the FDF to the kinetic (when resistive collisions dominate) and intermediate regimes using the RTA and Callaway's approximation, respectively. In Chapter 6, we provide experimental comparison of the GKE with the obtained *ab initio* parameters. This includes different materials (such as silicon or germanium), different temperatures (from 15 K to room temperature), different geometries (films, circular or linear heaters, confined nanostructures...), and stationary and non-stationary situations. In Chapter 7, FDF's limitations are analyzed, and a model's improvement is developed to extend the predictability. Finally, Chapter 8 is devoted to conclusions.

Thermal transport 2

This chapter summarizes a general view of the most relevant contributions in thermal transport related to our work. The objective is to provide a general framework to understand our research.

Historically, heat transport was described by Fourier's law. This empiric law relates the heat flux $\vec{q}$ with the local temperature T through spatial variation (Equation (1.1)). This equation is still used in numerous situations to describe the thermal evolution of solids, combined with the energy conservation equation

$$C_v \frac{\partial T}{\partial t} + \vec{\nabla} \cdot \vec{q} = 0, \tag{2.1}$$

being C_v the specific heat of the material.

At the nanoscale or with reduced time scales, this set of equations, using bulk thermal conductivity, has been widely demonstrated to fail in dielectrics: it reveals non-Fourier behavior in kinetic materials, where resistive collisions are dominant, like InGaAs and silicon [13, 15, 18, 22, 25, 58, 63, 65–67, 76] or in collective materials, where normal collisions are dominant [28, 36, 42, 54, 55, 60, 61, 77].

However, on many occasions, these experiments are characterized in terms of Fourier's law by introducing effective parameters, like effective thermal conductivities or effective thermal boundary resistances (TBR), to quantify the deviations from Fourier's law [11, 14, 16, 18, 21, 78]. Much theoretical effort to interpret these experiments consists of suppressing the contribution to the thermal conductivity

of phonons with a mean free path (MFP) larger than some characteristic system size [13, 14, 18, 51, 79, 80]. Other approaches address the study of non-Fourier effects through the linearized phonon BTE [8, 35, 41].

All these theoretical models are based on the phonon description of the thermal transport and the BTE (which will be discussed in Section 2.1). In addition, some efforts have been made to simulate real solids with molecular dynamics, i.e., through atomic motion [81–89]. However, the computational cost of "fully" simulating the material is incompatible with current device sizes and geometries. Therefore, it is helpful to introduce the phonon description [8, 90].

As introduced in Chapter 1, a phonon is a quasi-particle obtained from the solution of the expansion of the Hamiltonian of the atoms of the periodic lattice. This quantization of the energy vibrations in terms of phonons is due to the translational symmetry of the lattice. In this framework, the described solid can be interpreted as a gas of phonons with its corresponding energy $\hbar\omega_\lambda$ and momentum $\hbar\vec{k}$, where $\vec{k}$ is the wavevector of the λ-mode. The sub-index λ denotes the wavevector and the phonon branch. The nonlinear part of the Hamiltonian accounts for the interaction between different modes, which, in terms of phonons, means that phonons collide among them. When the collisions are fully random, Fourier's law is recovered. The number of phonons f_λ of a given λ-mode at a given position and time is described by the BTE.

This chapter, where some of the methods to describe thermal transport with phonons are presented, is organized as follows: Section 2.1 analyzes the BTE. Section 2.2 introduces the most relevant solutions of the BTE related to our work. Finally, in Section 2.3, some of the most relevant approximation methods to close the solution of the BTE are discussed.

2.1 Boltzmann transport equation

In terms of phonons, the picture of the thermal transport is complete when the distribution function of the phonons f_λ, i.e., the number of phonons of the λ-mode, is fully characterized. When the system is in equilibrium, meaning that no external field or temperature gradient is imposed, the distribution function is the Bose-Einstein distribution $f_\lambda = f_\lambda^{eq}$ [7,

91]

$$f_\lambda^{eq} \equiv \frac{1}{e^{\frac{\hbar\omega_\lambda}{k_B T}} - 1}, \tag{2.2}$$

being $\hbar$ and k_B the reduced Planck's constant and Boltzmann's constant, respectively. Equation (2.2) is fully described with a single scalar thermodynamic magnitude, the local temperature T, that characterizes the system when it is in equilibrium.

Out of equilibrium, the phonon distribution evolves through different mechanisms according to the BTE. Peierls introduced this equation in 1929 [8] by adapting to phonons the equations first derived for gases by Boltzmann in 1892 [26]. The two distinct mechanisms are, on the one hand, the drift of the distribution due to phonon motion (drift operator of the BTE). On the other hand, the collisions of the phonons with other phonons or particles (collisions operator). They result in the BTE introduced in Chapter 1, and we rewrite it here for this chapter to be self-contained:

$$\frac{\partial f_\lambda}{\partial t} + \vec{v}_\lambda \cdot \vec{\nabla} f_\lambda = C(f_\lambda). \tag{2.3}$$

One of the biggest difficulties of solving the BTE is that the collisions operator $C(f_\lambda)$ is a non-linear function of f_λ, as mentioned in Chapter 1. For illustration, the simple case (and, in general, more representative) is shown, where the three-phonon interaction is considered:

$$\begin{aligned} &C(f_\lambda) = \\ &\frac{1}{(2\pi)^3} \int\int \left[\Big(f_\lambda f_{\lambda'}(1 + f_{\lambda''}) - (1 + f_\lambda)(1 + f_{\lambda'}) f_{\lambda''} \Big) \Omega_{\lambda,\lambda'}^{\lambda''} \right. \\ &\left. + \frac{1}{2} \Big(f_\lambda (1 + f_{\lambda'})(1 + f_{\lambda''}) - (1 + f_\lambda) f_{\lambda'} f_{\lambda''} \Big) \Omega_\lambda^{\lambda',\lambda''} \right] d\lambda' d\lambda'', \end{aligned} \tag{2.4}$$

where $\Omega_{\lambda,\lambda'}^{\lambda''}$ is the scattering rate between two incident phonons λ and λ' resulting in an outgoing phonon λ'', and $\Omega_\lambda^{\lambda',\lambda''}$ is the scattering rate between one incident phonon λ resulting in two outgoing phonons λ' and λ''. For a schematic representation, see Figure 2.1. Typically, to describe thermal transport, it is sufficient to consider three-phonon interactions, which is the case considered in this thesis. Nevertheless, recent studies pointed out the need to include four-phonon interactions in some materials, like boron arsenide,

under certain non-equilibrium conditions [92, 93]. Apart from phonon-phonon interactions, the collision operator also includes collisions due to defects, impurities, and isotopic dispersion.

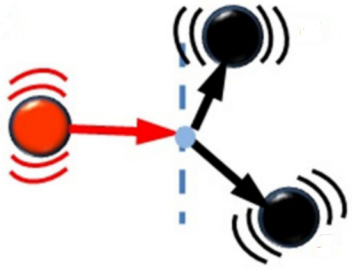

Figure 2.1: Schematic of three-phonon scattering. The red-ingoing phonon (λ) results in the black-outgoing phonons (λ' and λ''). *Image extracted from [94].*

Because of the complexity of the BTE, some simplifying assumptions are employed to address its solution. The first one is its linearization, described below.

2.1.1 Linearized BTE

Let us consider a small perturbation from the equilibrium distribution function,

$$\Delta f_\lambda = f_\lambda - f_\lambda^{eq}, \tag{2.5}$$

proportional to a certain thermodynamic perturbation, like $\vec{\nabla}T$. The perturbation can be expressed in terms of the function ϕ_λ defined as

$$\Delta f_\lambda = \frac{f_\lambda^{eq}(f_\lambda^{eq}+1)}{k_B T}\phi_\lambda, \tag{2.6}$$

where ϕ_λ accounts for the deviation from equilibrium. Introducing Equations (2.5) and (2.6) in the scattering operator (Equation (2.4)) and keeping up to the first order in ϕ_λ, one gets the next equation after some algebra [90]:

$$C(f_\lambda) = \int\int \left(\phi_\lambda - \phi_{\lambda'} - \phi_{\lambda''}\right) P_{\lambda,\lambda',\lambda''} \frac{d\lambda' d\lambda''}{(2\pi)^3}, \tag{2.7}$$

where $P_{\lambda,\lambda',\lambda''}$ is the equilibrium transition rate. This operator, in addition to the linear drift operator D, makes the BTE linear in Δf_λ, which allows applying the methods of linear differential equations. In particular, $C(f_\lambda)$ can be expressed

in a matrix form:

$$C(f_\lambda) = -\sum_{\lambda'} \Omega_{\lambda\lambda'} \Delta f_\lambda, \tag{2.8}$$

with $\Omega_{\lambda\lambda'}$ the so-called collision matrix. Then, the BTE can be written as

$$\mathbf{Df} = \mathbf{Cf}. \tag{2.9}$$

2.2 BTE solutions

As mentioned in Chapter 1, solving this equation analytically is only possible if some approximations are made. In this section, some of the more relevant BTE solutions are presented, going from simple approximations, like the RTA, to more complex derivations, like the one leading to the GKE.

2.2.1 Relaxation Time Approximation

As seen in Equation (2.8), the collision operator is a matrix with non-diagonal terms. To simplify this collisions operator, the most typical approximation is the RTA, which considers that the rate at which the λ-mode decays does not depend on the non-equilibrium situation of the other modes. Then, the collision matrix becomes diagonal and can be expressed as

$$C(f_\lambda) = -\frac{f_\lambda - f_\lambda^{eq}}{\tau_\lambda}, \tag{2.10}$$

where τ_λ is the relaxation time of the λ-mode [95].

For validating this approximation, an expression for the thermal conductivity can be obtained to compare with the experimental one. As a first approximation, the distribution function is assumed to depend on the equilibrium distribution function plus a term that depends on the temperature gradient, $f_\lambda = f_\lambda^{eq} + \vec{\alpha}_\lambda \cdot \vec{\nabla} T$, where $\vec{\alpha}_\lambda$ is an unknown parameter. By considering a stationary situation with a homogeneous gradient of the temperature, one can easily obtain $\vec{\alpha}_\lambda = -\tau_\lambda \frac{\partial f_\lambda^{eq}}{\partial T} \vec{v}_\lambda$ and the thermal conductivity obtained by simply applying the definition of the heat flux, which in terms of phonons reads $\vec{q} \equiv \int \hbar\omega_\lambda \vec{v}_\lambda f_\lambda d\lambda$. For an isotropic material, the thermal conductivity is

$$\kappa = \frac{1}{d} C_v \left\langle v_\lambda^2 \tau_\lambda \right\rangle, \tag{2.11}$$

where we have defined the average $\langle x_\lambda \rangle \equiv \int \hbar\omega_\lambda \frac{\partial f_\lambda^{eq}}{\partial T} x_\lambda d\lambda / C_v$ and d is the material dimension (for example, $d = 3$ for silicon, germanium or diamond, and $d = 2$ for graphene). The specific heat is defined as $C_v \equiv \int \hbar\omega_\lambda \frac{\partial f_\lambda^{eq}}{\partial T} d\lambda$. Figure 2.2 shows the results for the RTA thermal conductivity (Equation (2.11)) for different materials obtained with *ab initio* calculations, i.e., using phonon dispersion relations and scattering times obtained from atomic simulations (see Appendix A for details).

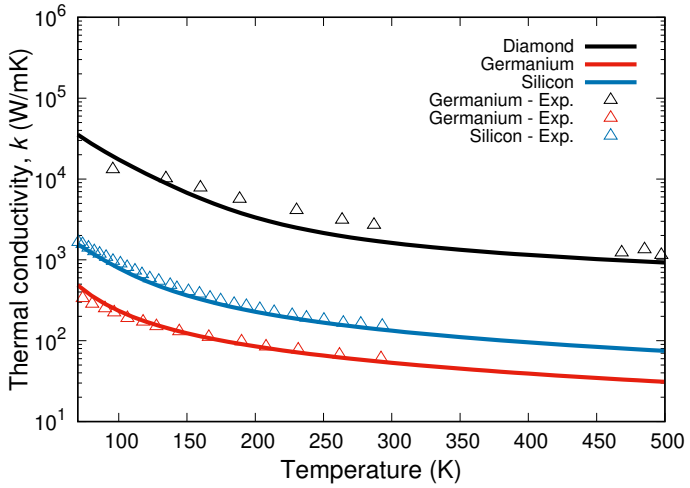

Figure 2.2: Thermal conductivity values under the RTA for different materials for a range of temperatures. Triangles represent the experimental values [96–98]. The *ab initio* calculations are described in Appendix A.

As seen in Equation (2.10), the RTA assumes that collisions relax the distribution to the equilibrium distribution function, which is at odds with some conservation laws. Energy conservation requires $\int \hbar\omega_\lambda C(f_\lambda) d\lambda = 0$, which is not generally guaranteed by Equation (2.10). Then, additional constraints must be added to fulfill this thermodynamic property [32, 35]. In addition, it is well known that normal collisions conserve the crystal momentum, and the collisions operator of the RTA can not guarantee this conservation law. To solve this problem, Callaway [27] proposed a modification of the RTA collisions operator, which is presented in the next section.

2.2.2 Callaway's approximation

As mentioned above, the RTA assumes that the collisions relax the distribution function to the equilibrium distribution function, and does not guarantee the momentum conservation of the normal collisions. Callaway [27] proposed modifying the RTA to incorporate this effect of the normal collisions.

The key point of this new collisions operator is to assume that normal collisions relax the distribution function to the displaced distribution function [7, 99]:

$$f_\lambda^d \equiv \frac{1}{e^{\frac{\hbar\left(\omega_\lambda - \vec{k}\cdot\vec{u}\right)}{k_B T}} - 1}, \tag{2.12}$$

where $\vec{u}$ is the so-called phonon drift velocity. This distribution function, in the absence of resistive collisions and stationary and homogeneous situations, is the distribution function that maximizes the entropy, keeping momentum constant [90, 100]. When the drift velocity is small, $\vec{k}\cdot\vec{u} \ll \hbar\omega_\lambda$, the displaced distribution function can be linearized:

$$f_\lambda^d \approx f_\lambda^{eq} + \frac{T}{\omega_\lambda}\frac{\partial f_\lambda^{eq}}{\partial T}\vec{k}\cdot\vec{u}. \tag{2.13}$$

Then, considering that normal collisions relax the distribution function to the displaced distribution function and that resistive collisions relax the distribution function to the equilibrium one, Callaway [27] proposed the next collisions operator:

$$C(f_\lambda) = -\frac{f_\lambda - f_\lambda^{eq}}{\tau_{R,\lambda}} - \frac{f_\lambda - f_\lambda^d}{\tau_{N,\lambda}}, \tag{2.14}$$

where $\tau_{R,\lambda}$ and $\tau_{N,\lambda}$ are the resistive and normal relaxation times of the λ-mode, respectively.

The drift velocity $\vec{u}$ is unknown at this point. In order to determine it, the momentum conservation for normal collisions is imposed,

$$\int \hbar\vec{k}_\lambda \frac{f_\lambda - f_\lambda^d}{\tau_{N,\lambda}} d\lambda = 0. \tag{2.15}$$

Through this imposition, it can be seen that the drift velocity depends on the distribution function. In the original work, Callaway assumes that the distribution function depends on the temperature gradient, implying that the drift velocity is proportional to it. However, this dependence on the temperature gradient is not the general case.

However, when considering Callaway's approximation,

the resulting thermal conductivity is

$$\kappa = \frac{1}{d} C_v \left(\left\langle v_\lambda^2 \tau_\lambda \right\rangle + \frac{\left\langle \frac{v_\lambda}{v_{p,\lambda}} \frac{\tau_\lambda}{\tau_{N,\lambda}} \right\rangle^2}{\left\langle \frac{1}{v_{p,\lambda}^2} \frac{\tau_\lambda}{\tau_{R,\lambda}\tau_{N,\lambda}} \right\rangle} \right), \tag{2.16}$$

where phase velocity of the λ-mode is defined as $v_{p,\lambda} \equiv \frac{\omega_\lambda}{k}$, and τ_λ is defined as $\tau_\lambda^{-1} \equiv \tau_{R,\lambda}^{-1} + \tau_{N,\lambda}^{-1}$. Notice that the obtained thermal conductivity is the RTA (Equation (2.11)) plus an additional term. If this additional term is small enough, the RTA should be a good approximation, corresponding to when resistive collisions dominate (i.e., $\tau_{R,\lambda} \ll \tau_{N,\lambda}$). For the cases where normal collisions dominate (i.e., $\tau_{R,\lambda} \gg \tau_{N,\lambda}$), the additional term is the relevant one.

Figure 2.3 compares the thermal conductivity under Callaway's approximation and the RTA. As is expected, when considering materials where normal collisions are important, the difference between the RTA conductivity and Callaway's is larger.

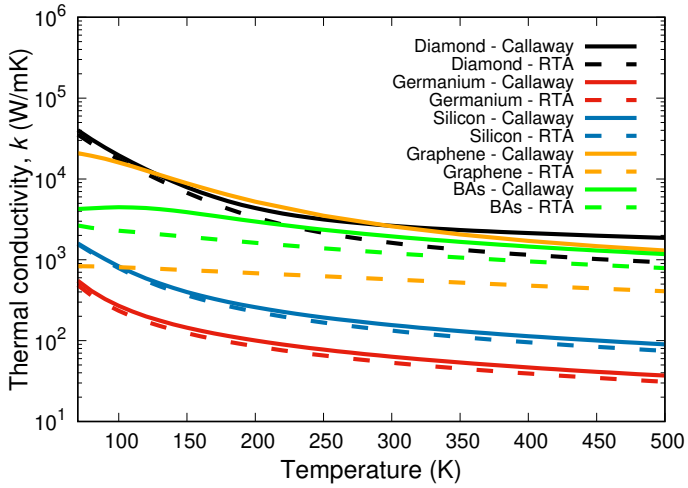

Figure 2.3: Thermal conductivity for Callaway's model (solid lines) and RTA (dashed lines) for different materials (diamond, germanium, silicon, graphene, and BAs) for a range of temperatures from 70 K to 500 K. For materials where resistive collisions dominate (silicon or germanium), the difference between the RTA and the Callaway's approximation is smaller than in materials where normal collisions dominate (diamond, graphene, or BAs). The *ab initio* calculations are described in Appendix A.

Callaway's approximation gives a physical insight into intermediate regimes between kinetic and collective ones. However, a refined method to capture this transition is presented below.

2.2.3 Iterative solution

The iterative solution [37, 38, 101–103] was proposed to obtain the distribution function of the phonons and the thermal conductivity using the full-matrix collisions operator. It allows the incorporation of the matrix's non-diagonal terms

and naturally introduces the redistribution between different phonon modes.

This method is based on numerical iterative processes. Then, the collisions operator (Equation (2.7)) is

$$C(f_\lambda)^{(i+1)} = \int\int \left(\phi_\lambda^{(i)} - \phi_{\lambda'}^{(i)} - \phi_{\lambda''}^{(i)}\right) P_{\lambda,\lambda',\lambda''} \frac{d\lambda' d\lambda''}{(2\pi)^3}, \tag{2.17}$$

where i denotes the iteration. The zeroth iteration ($i = 0$) is assumed to be the RTA solution ($\phi_{\lambda'}^{(i)} = \phi_{\lambda''}^{(i)} = 0$ because it is assumed that all the modes, except for the λ-mode, are in equilibrium).

In [37], they derive Fourier's law with a distribution function of the form $f_\lambda = f_\lambda^{eq} + \vec{\alpha}_\lambda \cdot \vec{\nabla} T$, with $\vec{\alpha}_\lambda$ as a weight function determined iteratively through this equation:

$$C(\vec{\alpha}_\lambda) = \frac{\partial f_\lambda^{eq}}{\partial T} \vec{v}_\lambda. \tag{2.18}$$

The expression for the thermal conductivity, once $\vec{\alpha}_\lambda$ is obtained, is $\kappa = \frac{1}{d} \int \hbar\omega_\lambda v_\lambda \alpha_\lambda d\lambda$ for isotropic materials.

2.2.4 Guyer-Krumhansl's derivation

So far, the solutions of the BTE presented in this section (Section 2.2) are based on obtaining the phonon distribution function. These are performed under a uniform temperature gradient, resulting in Fourier's law. The derivations' physical insight is incorporated into the BTE itself and the corresponding collision operator (for instance, RTA, Callaway or iterative collisions operator). Nevertheless, these derivations may not guarantee some relevant conservation laws, as is the case of the RTA or Callaway's approximation, where energy is not generally conserved, so some additional constraints must be imposed [32, 35].

From another perspective, Guyer and Krumhansl derived, in 1966, a hydrodynamic heat transport equation [52, 74]. The main difference between this approach and the previously presented ones is that Guyer and Krumhansl naturally impose the conservation law's through their mesoscopic variables, for instance, the energy and the momentum for normal collisions, and then do not require additional constraints.

One of the key points of Guyer and Krumhansl's derivation is the separation of the collisions operator between the conserving momentum collisions (normal collisions, N) and

non-conserving momentum collisions (resistive collisions, R), resulting in

$$C(f_\lambda) = N(f_\lambda) + R(f_\lambda). \tag{2.19}$$

In particular, the original work assumes that normal collisions dominate over resistive collisions ($N(f_\lambda) \gg R(f_\lambda)$). Another approximation is considered: a single branch Debye approximation, meaning that $v_\lambda = v =$ constant.

Its solution is based on developing a solution of the BTE for isotropic materials in terms of the eigenvectors of the symmetrized N-operator (see Appendix B). This operator must conserve energy and crystal momentum, meaning that there are four independent distribution functions with a null eigenvector: the zeroth-order element, $|0\rangle$, related to the deviation of energy with respect to the equilibrium energy, and three first-order elements, $|1, i\rangle$, related to the crystal momentum of the system in the three spatial directions, $i = x, y, z$. Then, an arbitrary deviation from the equilibrium distribution function, $\Delta f_\lambda \equiv f_\lambda - f_\lambda^{eq}$, can be written as

$$\Delta f_\lambda = a_0 |0\rangle + \sum_{\alpha=x,y,z} a_{1,\alpha} |1, \alpha\rangle + a_2 |2\rangle , \tag{2.20}$$

where $a_i(\vec{r}, t)$ are the occupation numbers in this new basis and $|2\rangle$ represent all the eigenvectors apart from the zeroth and first orders. Coefficients a_i are related to macroscopic variables: $a_0 \propto \Delta e$, where e is the phonon energy, and $\vec{a}_1 \propto \vec{q}$. In terms of this basis, defined in [52], the BTE can be rewritten as follows

$$\begin{aligned} &\begin{pmatrix} 0 & 0 & 0 \\ 0 & R_{11} & R_{12} \\ 0 & R_{21} & N_{22} + R_{22} \end{pmatrix} \cdot \begin{pmatrix} a_0 \\ \mathbf{a}_1 \\ \mathbf{a}_2 \end{pmatrix} \\ &= \begin{pmatrix} D_{00} & D_{10} & 0 \\ D_{10} & D_{11} & D_{12} \\ 0 & D_{21} & D_{22} \end{pmatrix} \cdot \begin{pmatrix} a_0 \\ \mathbf{a}_1 \\ \mathbf{a}_2 \end{pmatrix}, \end{aligned} \tag{2.21}$$

where $\mathbf{D}$ is the drift operator, and X_{ij} are the components of operator X on the $|k\rangle$-basis. As mentioned above, from the perspective of the mesoscopic variables a_i, it is easy to guarantee the conservation laws of the collisions operator just by introducing null components into the collisions matrix.

The first row of Equation (2.21) is the energy conservation equation, that is, Equation (2.1). The following equation

is obtained by combining the second and the third rows:

$$D_{11}\mathbf{a}_1 + D_{10}a_0 = \left(R_{11} - (R_{12} - D_{12})\left(N_{22} + R_{22} - D_{22}\right)^{-1}(R_{21} - D_{21})\right)\mathbf{a}_1. \tag{2.22}$$

This result is a general transport equation. Nevertheless, Guyer and Krumhansl derived its solution when normal collisions dominate. To obtain the final expression for the GKE, some identifications of the collisions operator, developed in [52], are done:

$$N_{22} \to \frac{1}{\tau_N}, \tag{2.23a}$$

$$R_{11} \to \langle 1|\, \tau_R(q)^{-1}\, |1\rangle\,, \tag{2.23b}$$

$$R_{22} \approx R_{11}, \tag{2.23c}$$

$$\left(\mathbf{R}^{-1}\right)_{11} \to \langle 1|\, \tau_R(q)\, |1\rangle\,, \tag{2.23d}$$

where τ_N and τ_R are the normal and resistive relaxation times, respectively. By combining these equations with Equation (2.22), one can obtain GKE (Equation (1.3)), which we rewrite here completeness:

$$\vec{q} + \tau\frac{\partial\vec{q}}{\partial t} = -\kappa\vec{\nabla}T + \ell^2\left(\nabla^2 + 2\vec{\nabla}(\nabla\vec{\cdot}\,\vec{q})\right) \tag{2.24}$$

This equation resembles the NSE for fluids, which is why it is named the *hydrodynamic equation*.

Let us analyze the different parameters appearing in this equation. The thermal conductivity is

$$\kappa = \frac{1}{3}C_v v^2\left(\Sigma\tau_C + (1-\Sigma)\tau_K\right), \tag{2.25}$$

where it has been defined the collective time $\tau_C \equiv \langle 1|\, \tau_R^{-1}\, |1\rangle^{-1}$, the kinetic time $\tau_K \equiv \langle 1|\, \tau_R\, |1\rangle$, and the Σ is defined as

$$\Sigma \equiv \frac{1}{1 + \frac{\tau_N}{\tau_K}}. \tag{2.26}$$

As expected, this Σ parameter switches between the collective thermal conductivity (when $\Sigma = 1$, i.e., normal collisions dominate) and the kinetic thermal conductivity (when $\Sigma = 0$, i.e., resistive collisions dominate).

This expression properly includes the role of normal collisions, in contrast to RTA, where they are dealt with as resistive ones. Notice that even though normal collisions do not directly contribute to thermal conductivity (for $R \to 0$ we have $\kappa \to \infty$), their influence modifies it [90]. In the kinetic regime ($R \gg N$), this expression considers that phonons relax independently to the equilibrium, as assumed in the RTA (see Section 2.2.1). In the collective regime, where it is fulfilled that $\left\langle \tau_{R,\lambda}^{-1} \right\rangle \ll \omega \ll \left\langle \tau_{N,\lambda}^{-1} \right\rangle$, many normal collisions occur before a resistive collision, thus redistributing the crystal momentum. Hence, the distribution relaxes collectively, characterized by a single collective timescale. Guyer and Krumhansl do not present numerical predictions for this expression of the thermal conductivity (Equation (2.25)). However, it has been validated for a wide range of temperatures, materials, and experiments using first principle calculations in [73].

Guyer and Krumhansl also obtained expressions for the nonlocal length ℓ and the heat flux relaxation time τ in the collective regime since the derivation of the original work [52] was done in this regime. For these two parameters, the following expressions are obtained:

$$\ell^2 = \frac{1}{5} v^2 \tau_N \tau_C, \tag{2.27a}$$

$$\tau = \tau_C. \tag{2.27b}$$

As mentioned above, the GKE was first derived in the collective regime [52] because of its analogy with fluid collisions. This has led to the common belief that normal collisions must dominate for thermal transport to be described by a hydrodynamic equation such as the GKE. However, in recent years, some works derived the GKE in the kinetic limit by assuming identical branches, the Debye approximation, and a mode-independent relaxation time [57, 104–106]. Unfortunately, it results in non-predictive formalisms. KCM was proposed to solve this problem.

2.2.5 Kinetic-Collective Model (KCM)

For stationary situations and uniform temperature gradients, Guyer and Krumhansl obtain a thermal conductivity that interpolates between the kinetic and collective limits (Equation (2.25)). The KCM, developed by Álvarez and col-

leagues [71–73], takes this idea for the thermal conductivity and extrapolates it to the ℓ parameter of the GKE. The resulting parameters for the GKE can describe a wide range of experiments and situations in silicon [58, 59, 62, 63, 65, 67] and consequently support both: the equation and the parameters.

The KCM assumes that the relaxation time of a given λ-mode is a linear combination of the collective relaxation time τ_C of the whole modes and the kinetic relaxation time of the given mode $\tau_{K,\lambda}$, which is the resistive relaxation time, with the same interpolating parameter Σ that is used in the interpolation of the thermal conductivity:

$$\tau_{KCM,\lambda} = \Sigma\tau_C + (1-\Sigma)\tau_{K,\lambda}. \tag{2.28}$$

Then, normal collisions contribute to redistributing the phonon population by increasing the mean free path of the high-frequency phonons and reducing the low-frequency ones, as observed in Figure 2.4.

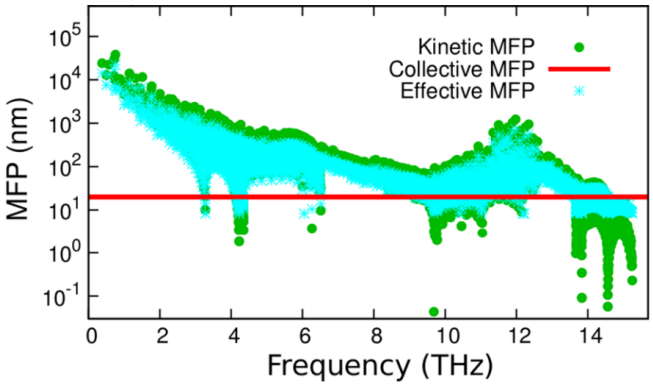

Figure 2.4: MFPs as a function of the frequency of the phonons for silicon at room temperature. In green, the kinetic MFP (just considering the resistive relaxation time) is represented; in red, the collective one; in blue, the linear combination (effective MFP), which is the one proposed by the KCM. Normal collisions redistribute the population to increase the MFP of high-frequency phonons and reduce the MFP of the low-frequency ones. *Image extracted from [73].*

The procedure is the same for the mesoscopic parameters κ and ℓ. In fact, for the thermal conductivity, it is used the expression obtained by Guyer and Krumhansl [52], Equation (2.25), with excellent results for a wide range of temperatures and materials [58, 59, 62, 73], as shown in Figure 2.5.

The main innovation of KCM is the statement that there are nonlocal effects even in the kinetic limit. Once again, the nonlocal length ℓ is calculated through interpolation between the kinetic and the collective limit:

$$\ell^2 = \Sigma\ell_C^2 + (1-\Sigma)\ell_K^2, \tag{2.29}$$

where ℓ_C is the nonlocal length in the collective limit, which

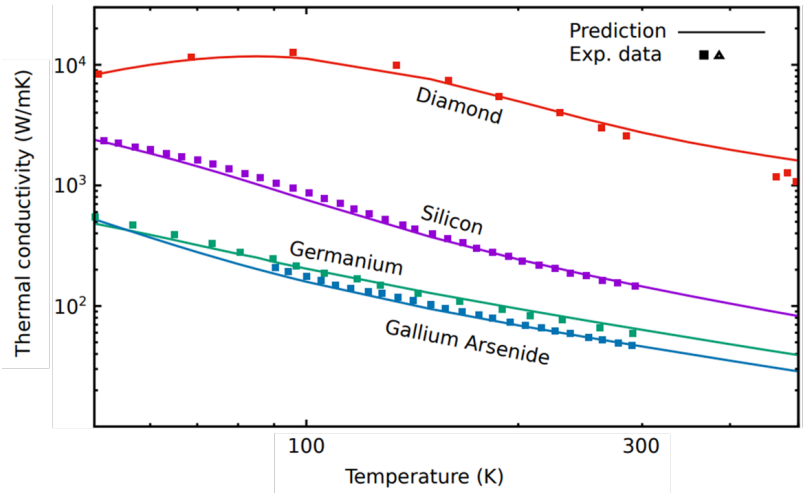

Figure 2.5: Thermal conductivity obtained with the KCM for diamond, silicon, germanium, and gallium arsenide for different temperatures. The obtained thermal conductivities are compared to experimental data. *Image extracted from [73].*

is the one proposed by Guyer and Krumhansl in [52], and ℓ_K is the nonlocal length in the kinetic limit [73]. As mentioned above, the values of the nonlocal length obtained through *ab initio* techniques combined with the thermal conductivity have been demonstrated to reproduce a wide range of experiments with different materials [58, 59, 62, 63, 65, 67].

2.3 Approximation methods

The previously introduced approaches, except for Guyer and Krumhansl's, focused on obtaining thermal conductivity. Thus, its applicability is limited to infinite crystals, where there are no boundary effects. This is the case, for example, of homogeneous perturbations like a constant temperature gradient. Two standard methods were originally proposed, aiming to refine the treatment of the BTE to capture the failure of Fourier's law: the Chapman-Enskogg (CE) method [107] and Grad's method [108].

These methods are based on obtaining the nonequilibrium distribution function and the transport equations under certain assumptions, providing a closed description of the system. As in the case of Guyer and Krumhansl's derivation [52], one of the main advantages of these methods is the capability to guarantee the conservation laws (energy conservation, momentum conservation of the normal collisions...).

The main difference between CE and Grad's methods is the expansion variables of the distribution function. The first one is based on expanding the distribution function in terms of the Knudsen number, which is the ratio between an intrinsic length of the material and a characteristic length of the experiment. This method recovers Fourier's law for

small Knudsen numbers, but it yields unstable equations like Burnett ones for higher-order expansion. On the other side, Grad's moments method is based on expanding the distribution function in terms of the polynomials of the microscopic variables with coefficients which are moments of the distribution. This method provides hyperbolic transport equations yielding discontinuities that are not observed. In the last decades, the regularized moment method [57, 109] has been developed to solve this issue, which yields parabolic equations and prevents these discontinuities.

Unfortunately, this is obtained under very strong assumptions, such as a single linear (Debye) branch and a RTA with the same relaxation time (gray model). In [57], this method is used to derive the GKE assuming an expansion around the displaced distribution function (Equation (2.12)). In summary, all the derivations of the GKE from the BTE assume the collective limit, except for the regularized method, which considers quite unrealistic assumptions but might apply to the kinetic limit. However, this drawback prevents any comparison with experiments. Then, in the literature, there is no microscopic derivation of the GKE for kinetic materials under realistic assumptions. Therefore, there is a gap between theoretical models and experimental evidence, which shows that the GKE properly describes several experiments in kinetic materials like silicon.

The goal of this thesis is to fill this gap. To this end, in the next chapter, we present a new method to solve the BTE, the flux derivatives formalism (FDF). It provides a mixed approach between Grad's method and Chapman-Enskog derivation, similar to the regularized one, but extended to a general collisions operator. This allows deriving the GKE for general collisions operator, dispersion relations, and a number of branches. The method yields specific expressions for the transport coefficients, which can be calculated *ab initio* and be directly compared to experiments.

The Flux derivatives Formalism

3

This chapter presents a formalism, valid for moderate Knudsen numbers, to derive, from an ansatz of the phonon distribution function, a complete set of equations (i.e., the phonon distribution function, the heat-transport equations, and its corresponding boundary conditions) that are consistent with the assumption. This formalism, named the Flux derivatives formalism (FDF) [70], is inspired by the philosophy of EIT, which stresses the importance of the choice of the macroscopic variables describing the non-equilibrium state. In this sense, all the results presented in the chapter can be obtained with the complete collision operator or any approximation to it (for example, the RTA or Callaway's model).

The choice of the ansatz for the distribution function can be interpreted as an expansion of appropriate mesoscopic variables. Typically, as considered in Broido et al. work, the expansion consisted of a perturbation of the temperature gradient [27, 37, 110] or, when collective materials are considered, it consists of the displaced distribution function [43, 52, 57, 69, 74, 104–106, 111–113]. These expansions implicitly assume that these mesoscopic variables (the temperature gradient and the drifting velocity, respectively) are representative of the description of the physical situation. Nevertheless, when characteristic times or sizes of the system are very small, it is reasonable to consider that higher-order expansion is required to describe the physical situation properly.

This higher-order mathematical expansion has a subsequent consequence in the physical interpretation. In analogy to the EIT [75], by introducing a mesoscopic variable into the

distribution function, we assume it is a slow variable. This means that its destruction is slow enough to be considered a fundamental variable to characterize the system and evolves independently of the other considered variables.

In practice, this implies that, depending on the described physical situation, the distribution function has to be expanded with a certain number of mesoscopic variables. As already said, the formalism presented here connects a distribution function with the transport equations and the boundary conditions. So, when choosing the mesoscopic variables to describe the system, the transport equations and the boundary conditions are fully determined. This "triangle" in Figure 3.1 (the distribution function, the transport equations, and the boundary conditions), which is self-consistent, is one of the strongest points of this formalism.

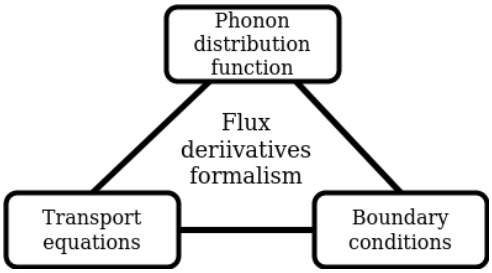

Figure 3.1: Triangle with the phonon distribution function, transport equations, and boundary conditions. FDF provides consistent expressions of these three magnitudes.

Notice that it is emphasized the importance of the non-equilibrium situation to characterize the system properly. This formalism is not restricted to certain materials. At odds with the common belief, for example, this formalism recovers a GKE for kinetic materials like silicon or germanium with predictive parameters [70].

The chapter is organized as follows: Section 3.1 gives a general perspective of the formalism. In Section 3.2, a derivation of Fourier's law with the present formalism is presented, and we strictly recover the thermal conductivity of previous literature [37] as a first check of the formalism. In Section 3.3, a derivation of the GKE with the general collisions operator is shown. In Section 3.4, the corresponding boundary conditions for the GKE are derived from its microscopic expressions. Finally, Section 3.5 is devoted to presenting some conclusions about the formalism.

3.1 General procedure

From a microscopic point of view, thermal transport is well characterized by the linearized BTE. Nevertheless, this equa-

tion is difficult to solve both analytically and computationally for the complex geometries usually found in engineering applications. To optimize the solution, in classical kinetic theory, two well-known methods are used to obtain macroscopic equations from the BTE: the Chapman-Enskog (CE) method [107] and the Grad's moment method [108], presented in Section 2.3. They provide their microscopic counterpart in the form of microscopic expressions for the transport coefficients appearing therein and the non-equilibrium distribution function.

CE method uses the first moments of the distribution as independent variables, which for heat transport is reduced to the temperature T. As a result, the phonon distribution and the macroscopic equations depend on the temperature and its gradients. It is based on an expansion in the Knudsen number and produces Fourier's law to first order and Burnett and super-Burnett equations at higher orders [109]. On the other hand, Grad's method assumes as independent variables the moments of the distribution, which includes the temperature, as in CE, but also the heat flux and, eventually, higher-order fluxes. The distribution function depends on these variables but not on their derivatives. Beyond Fourier, the macroscopic equations produced by both methods display some shortcomings, such as the instability of transient solutions in Burnett and super-Burnett equations, or the discontinuity of some properties in Grad's equations due to their hyperbolic character, added to the difficulty of posing proper boundary conditions for higher derivatives or higher moments, respectively [109].

The formalism presented here, the FDF, uses a mixed approach of CE and Grad methods. The key point is to extend the set of independent mesoscopic variables to the heat flux and its derivatives, both in space and time. The results are similar to those found in the regularized moment method under simplifying assumptions, such as a single dispersionless branch under RTA for a single relaxation time (gray model) [114]. Furthermore, we will consider isotropic materials for the seek of simplicity, but it can be extended to anisotropic materials.

The first step of the formalism is to project the BTE into thermodynamic variables to obtain simpler equations that can be compared to experimental results. Typically, the projections are the energy and the crystalline momentum of the BTE (see Appendix C for a physical argument). With

these two projections, the following equations are obtained:

$$\frac{\partial e}{\partial t} + \vec{\nabla} \cdot \vec{q} = 0, \tag{3.1a}$$

$$\frac{\partial \vec{p}}{\partial t} + \vec{\nabla} \cdot \overline{\overline{\Pi}} = \int \hbar \vec{k}_\lambda C(f_\lambda) d\lambda, \tag{3.1b}$$

where $e \equiv \int \hbar \omega_\lambda f_\lambda d\lambda$ is the energy density, $\vec{q}$ is the heat flux, $\vec{p} \equiv \int \hbar \vec{k}_\lambda f_\lambda d\lambda$ is the crystal-momentum density and $\overline{\overline{\Pi}} \equiv \int \hbar \vec{k} \lambda \vec{v}_\lambda f_\lambda d\lambda$ is the flux of the crystal momentum. These equations describe the conservation of energy and the balance of the quasimomentum.

To close the system and solve it, one needs to relate $\vec{p}$ and $\overline{\overline{\Pi}}$ to the energy density and the heat flux. This relation can be easily obtained by introducing the phonon distribution function to the latter expressions for $\vec{p}$ and $\overline{\overline{\Pi}}$. The issue is to obtain a solution for this distribution.

In this formalism, the distribution function is assumed to depend on a certain number of mesoscopic variables (such as temperature, heat flux, its derivatives. . .). Under the non-equilibrium situation described, these variables are assumed to describe the phonon population properly. Then, the distribution function is

$$f_\lambda = f_\lambda^{eq} + \sum_i a_{\lambda,i} Q_i, \tag{3.2}$$

where Q_i are the known mesoscopic variables and $a_{\lambda,i}$ are unknown coefficients that only depend on the phonon mode λ. When $a_{\lambda,i}$ are determined, the phonon distribution function is also determined, and then, the system is solved from a microscopic (Equation (3.2)) and a mesoscopic (Equations (3.1a) and (3.1b)) perspective. To determine the $a_{\lambda,i}$, we follow a set of steps. First, Equation (3.2) is introduced into Equations (3.1a) and (3.1b). The resulting equations give a relation between the mesoscopic quantities present in the ansatz for the distribution function. These are the transport equations that can be solved to describe the system macroscopically.

Then, Equation (3.2) is introduced into the BTE, resulting

in

$$\begin{aligned} &\frac{\partial f_\lambda^{eq}}{\partial T}\frac{\partial T}{\partial t} + \sum_i a_{\lambda,i}\frac{\partial Q_i}{\partial t} \\ &+\frac{\partial f_\lambda^{eq}}{\partial T}\vec{v}_\lambda \cdot \vec{\nabla}T + \sum_i a_{\lambda,i}\vec{v}_\lambda \cdot \vec{\nabla}Q_i = \sum_i C(a_{\lambda,i})Q_i. \end{aligned} \tag{3.3}$$

After that, the two transport equations (Equations (3.1a) and (3.1b)) are substituted into Equation (3.3) to reduce the degrees of freedom and obtain an equation with independent macroscopic variables.

Nevertheless, some higher-order derivatives appear in Equation (3.3) that can not be equated to the rest of the terms of the BTE ($\partial_t Q_i \neq Q_j$ or $\vec{\nabla}Q_i \neq Q_j$). We consider that these terms can be neglected for small enough Knudsen numbers, resulting in an equation with independent macroscopic variables. This is one of the main assumptions of our formalism.

Finally, for the equation to be satisfied, the coefficients of the (independent) macroscopic variables should be identical, and all the $a_{\lambda,i}$ coefficients are well determined. This implies that the distribution function is determined, and Equations (3.1a) and (3.1b) can also be obtained. Then, the system is closed with the microscopic and mesoscopic descriptions. Thus the BTE is solved.

3.2 Fourier's law derivation

This section provides a derivation of Fourier's law using the previous formalism. In this case, we consider a stationary situation with a uniform temperature gradient. The proposed distribution function is a perturbation in the heat flux

$$f_\lambda = f_\lambda^{eq} + \vec{\beta}_\lambda \cdot \vec{q}, \tag{3.4}$$

where $\vec{\beta}_\lambda$ is an unknown λ-mode dependent coefficient. In this situation, $\vec{\beta}_\lambda$ plays the role of $a_{\lambda,i}$ and $\vec{q}$ of Q_i in Equation (3.3). The underlying assumption in this ansatz is that the heat flux is a slow magnitude in the system, and it is enough to describe the distribution function.

The next step is introducing it into Equations (3.1a) and (3.1b). Moreover, as we consider a stationary situation, the

resulting equations are

$$\vec{\nabla} \cdot \vec{q} = 0, \tag{3.5a}$$

$$\begin{aligned} &\int \hbar \vec{k}_\lambda \frac{\partial f_\lambda^{eq}}{\partial T} \vec{v}_\lambda d\lambda \cdot \vec{\nabla} T + \int \hbar \vec{k}_\lambda \vec{v}_\lambda \vec{\beta}_\lambda d\lambda : \vec{\nabla} \vec{q} \\ &= \int \hbar \vec{k}_\lambda C(\vec{\beta}_\lambda) d\lambda \cdot \vec{q}. \end{aligned} \tag{3.5b}$$

In the previous equation, we use that $C(f_\lambda) = -\sum_{\lambda'} \Omega_{\lambda\lambda'} \Delta f_\lambda$ (Equation (2.8)). An isotropic material is considered to simplify the calculations. With this consideration, the following general relation is obtained (see Appendix D for the derivation)

$$\int A_\lambda \vec{v}_\lambda \vec{v}_\lambda d\lambda = \frac{1}{d} \int A_\lambda v_\lambda^2 d\lambda \; \mathbb{1}, \tag{3.6}$$

where A_λ is a scalar that depends on the λ-mode, $\mathbb{1}$ is the identity matrix, and d is the dimension of the material ($d = 3$ for general materials like silicon, germanium... and $d = 2$ for 2-D materials like graphene). Furthermore, by isotropy, the integral $\int \hbar \vec{k}_\lambda \vec{v}_\lambda \vec{\beta}_\lambda d\lambda$ vanishes, and we finally obtain

$$\frac{1}{d} \int \hbar k_\lambda \frac{\partial f_\lambda^{eq}}{\partial T} v_\lambda d\lambda \; \vec{\nabla} T = \frac{1}{d} \int \hbar k_\lambda C(\beta_\lambda) d\lambda \; \vec{q}, \tag{3.7}$$

where we have used that any vector can be decomposed on $\vec{x}_\lambda = x_\lambda \hat{v}_\lambda$, and $\hat{v}_\lambda$ is the unitary vector of $\vec{v}_\lambda$. Defining thermal conductivity as

$$\kappa \equiv -\frac{\int \hbar k_\lambda \frac{\partial f_\lambda^{eq}}{\partial T} v_\lambda d\lambda}{\int \hbar k_\lambda C(\beta_\lambda) d\lambda}, \tag{3.8}$$

Fourier's law is recovered

$$\vec{q} = -\kappa \vec{\nabla} T. \tag{3.9}$$

To fully characterize Fourier's law, thermal conductivity has to be determined. To do so, we use the BTE itself. Since a stationary situation is considered, Equation (3.4) introduced into the BTE gives

$$\frac{\partial f_\lambda^{eq}}{\partial T} \vec{v}_\lambda \cdot \vec{\nabla} T + \vec{v}_\lambda \vec{\beta}_\lambda : \vec{\nabla} \vec{q} = C(\vec{\beta}_\lambda) \cdot \vec{q}. \tag{3.10}$$

We reduce the degrees of freedom of this equation introducing the transport equation (Equation (3.9)) into Equation (3.10). Then, when considering a uniform temperature gradient, one obtains the following equation for $\vec{\beta}_\lambda$

$$C(\vec{\beta}_\lambda) = -\frac{1}{\kappa}\frac{\partial f_\lambda^{eq}}{\partial T}\vec{v}_\lambda. \tag{3.11}$$

Then, we have two unknown variables: $\vec{\beta}_\lambda$ and κ. By defining $\vec{\alpha}_\lambda \equiv -\kappa\vec{\beta}_\lambda$, Equation (3.11) becomes

$$C(\vec{\alpha}_\lambda) = \frac{\partial f_\lambda^{eq}}{\partial T}\vec{v}_\lambda \tag{3.12}$$

This result is strictly the same one obtained in [37], where it is considered an expansion as $f_\lambda = f_\lambda^{eq} + \vec{\alpha}_\lambda \cdot \vec{\nabla}T$, and they obtain Equation (3.12). $\vec{\alpha}_\lambda$ can be solved for general collisions operators through iterative methods [37, 54] or with other collisions operator like the RTA or Callaway's model (see Chapter 5).

In order to obtain $\vec{\beta}_\lambda$ and κ from $\vec{\alpha}_\lambda$, a consistency relation is imposed. This consistency relation comes from the definition of the heat flux applied to the ansatz for the distribution function $\vec{q} = \int \hbar\omega_\lambda \vec{v}_\lambda \vec{\beta}_\lambda d\lambda \cdot \vec{q}$, which gives

$$\frac{1}{d}\int \hbar\omega_\lambda v_\lambda \beta_\lambda d\lambda = 1. \tag{3.13}$$

Since $\vec{\beta}_\lambda = -\frac{\vec{\alpha}_\lambda}{\kappa}$, Equation (3.13) yields the following expression for thermal conductivity

$$\kappa = -\frac{1}{d}\int \hbar\omega_\lambda v_\lambda \alpha_\lambda d\lambda, \tag{3.14}$$

which is also the expression found by Broido [37]. The knowledge of $\vec{\alpha}_\lambda$ and κ determines $\vec{\beta}_\lambda$. Then, both the microscopic and the mesoscopic descriptions are complete.

To conclude this section, we would like to remark that it is enough to perturb the distribution function with the heat flux (or the gradient of temperature that, in this situation, is equivalent) to derive Fourier's law. When a more complex physical situation is described, it seems reasonable that a more complex distribution function is needed, as we explain in the next section.

3.3 Derivation of the Guyer-Krumhansl's equation

In the present section, we derive the GKE for general semiconductors for moderate Knudsen numbers. As mentioned in Section 3.1, the choice of the distribution function directly implies the resulting transport equation. Moreover, the choice of the distribution function depends on the physical non-equilibrium situation to be described.

Since the derivation of Fourier's law requires an expansion of the distribution function on the heat flux (Equation (3.4)), the next expansion may include the heat flux and its first derivatives. As mentioned in Section 3.1, this assumption implies that the heat flux and its first derivatives slowly evolve and are relevant enough to characterize the system. Then, we assume the following distribution function:

$$f_\lambda = f_\lambda^{eq} + \vec{\beta}_\lambda \cdot \vec{q} + \vec{\gamma}_\lambda \cdot \frac{\partial \vec{q}}{\partial t} + \overline{\overline{G}}_\lambda : \vec{\nabla}\vec{q}, \tag{3.15}$$

where $\vec{\beta}_\lambda$ and $\vec{\gamma}_\lambda$ are vectors, and $\overline{\overline{G}}_\lambda$ is a tensor, all depending on the λ-mode, and they are unknown. In an isotropic material, a rank 2 tensor can be written as $\overline{\overline{G}}_\lambda = \overline{\overline{G}}_{1,\lambda} + \overline{\overline{G}}_{2,\lambda}$ with $\overline{\overline{G}}_{1,\lambda} \equiv g_{1,\lambda}\hat{v}_\lambda\hat{v}_\lambda$ and $\overline{\overline{G}}_{2,\lambda} \equiv g_{2,\lambda}\mathbb{1}$, where $g_{1,\lambda}$ and $g_{2,\lambda}$ are unknown scalars that depend on the λ-mode.

Then, the distribution function is introduced into Equations (3.1a) and (3.1b) to obtain the transport equation, and the resulting equations are

$$\int \hbar\omega_\lambda \frac{\partial f_\lambda^{eq}}{\partial T} d\lambda \frac{\partial T}{\partial t} + \\ + \left(\frac{1}{d}\int \hbar\omega_\lambda g_{1,\lambda} d\lambda + \int \hbar\omega_\lambda g_{2,\lambda} d\lambda\right) \frac{\partial \vec{\nabla}\cdot\vec{q}}{\partial t} + \vec{\nabla}\cdot\vec{q} = 0 \tag{3.16}$$

$$\frac{1}{d}\int \hbar k_\lambda \beta_\lambda d\lambda \frac{\partial \vec{q}}{\partial t} + \frac{1}{d}\int \hbar k_\lambda \gamma_\lambda d\lambda \frac{\partial^2 \vec{q}}{\partial t^2} + \\ + \frac{1}{d}\int \hbar k_\lambda \frac{\partial f_\lambda^{eq}}{\partial T} v_\lambda d\lambda \vec{\nabla} T + \frac{1}{d(d+2)}\int \hbar k_\lambda v_\lambda g_{1,\lambda} d\lambda \nabla^2 \vec{q} + \\ + \left(\frac{2}{d(d+2)}\int \hbar k_\lambda v_\lambda g_{1,\lambda} d\lambda + \frac{1}{d}\int \hbar k_\lambda v_\lambda g_{2,\lambda}\right)\vec{\nabla}(\vec{\nabla}\cdot\vec{q}) = \\ = \frac{1}{d}\int \hbar k_\lambda C(\beta_\lambda) d\lambda \vec{q} + \frac{1}{d}\int \hbar k_\lambda C(\gamma_\lambda) d\lambda \frac{\partial \vec{q}}{\partial t}. \tag{3.17}$$

In these expressions, for isotropic materials, we have used the following relation (see Appendix D for the derivation):

$$\int A_\lambda \frac{v_{\lambda,i} v_{\lambda,j} v_{\lambda,k} v_{\lambda,l}}{v_\lambda^4} d\lambda \\ = \frac{1}{d(d+2)}(\delta_{ij}\delta_{kl} + \delta_{ik}\delta_{kl} + \delta_{il}\delta_{jk}) \int A_\lambda d\lambda. \tag{3.18}$$

Equations (3.16) and (3.17), then, are rewritten as

$$C_v \frac{\partial T}{\partial t} - \tau_e \frac{\partial \vec{\nabla}\cdot\vec{q}}{\partial t} + \vec{\nabla}\cdot\vec{q} = 0, \tag{3.19a}$$

$$\vec{q} + \tau \frac{\partial \vec{q}}{\partial t} + \tau_p^2 \frac{\partial^2 \vec{q}}{\partial t^2} = -\kappa \vec{\nabla} T + \ell^2 \left(\nabla^2 \vec{q} + \alpha' \vec{\nabla}(\vec{\nabla}\cdot\vec{q})\right). \tag{3.19b}$$

These equations are the energy conservation and the GKE, respectively. Then, the GKE is derived, for the first time, for a general collisions operator, which ranges from the collective to the kinetic regimes [70].

In these expressions, we have defined that

$$\tau_e \equiv -\left(\frac{1}{d}\int \hbar \omega_\lambda g_{1,\lambda} d\lambda + \int \hbar \omega_\lambda g_{2,\lambda} d\lambda\right), \tag{3.20a}$$

$$\tau \equiv \frac{\int \hbar k_\lambda C(\gamma_\lambda) d\lambda - \int \hbar k_\lambda \beta_\lambda d\lambda}{\int \hbar k_\lambda C(\beta_\lambda) d\lambda}, \tag{3.20b}$$

$$\tau_p^2 \equiv -\frac{\int \hbar k_\lambda \gamma_\lambda d\lambda}{\int \hbar k_\lambda C(\beta_\lambda) d\lambda}, \tag{3.20c}$$

$$\kappa \equiv -\frac{\int \hbar k_\lambda \frac{\partial f_\lambda^{eq}}{\partial T} v_\lambda d\lambda}{\int \hbar k_\lambda C(\beta_\lambda) d\lambda}, \tag{3.20d}$$

$$\ell^2 \equiv \frac{1}{d+2}\frac{\int \hbar k_\lambda v_\lambda g_{1,\lambda} d\lambda}{\int \hbar k_\lambda C(\beta_\lambda) d\lambda}, \tag{3.20e}$$

$$\alpha' \equiv 2 + (d+2)\frac{\int \hbar k_\lambda v_\lambda g_{2,\lambda} d\lambda}{\int \hbar k_\lambda v_\lambda g_{1,\lambda} d\lambda}. \tag{3.20f}$$

So far, the expressions for the mesoscopic parameters have been obtained, but to fully characterize them, it is necessary to complete the microscopic description, i.e., obtaining $\vec{\beta}_\lambda$, $\vec{\gamma}_\lambda$, and $\overline{\overline{G}}_\lambda$. With this aim, Equation (3.15) is introduced into the BTE, and Equations (3.19a) and (3.19b) are used to reduce the number of independent macroscopic quantities. The obtained equation is

$$\begin{aligned}
&\frac{\partial f_\lambda^{eq}}{\partial T}\left(\frac{\tau_e}{C_v}\frac{\partial \vec{\nabla}\cdot\vec{q}}{\partial t} - \frac{1}{C_v}\vec{\nabla}\cdot\vec{q}\right) + \\
&+\vec{\beta}_\lambda \cdot \frac{\partial \vec{q}}{\partial t} + \vec{\gamma}_\lambda \cdot \frac{\partial^2 \vec{q}}{\partial t^2} + \overline{\overline{G}}_\lambda : \frac{\partial \vec{\nabla}\vec{q}}{\partial t} + \\
&+\frac{\partial f_\lambda^{eq}}{\partial T}\vec{v}_\lambda \cdot \left(-\frac{1}{\kappa}\vec{q} - \frac{\tau}{\kappa}\frac{\partial \vec{q}}{\partial t} - \frac{\tau_p^2}{\kappa}\frac{\partial^2 \vec{q}}{\partial t^2}\right) + \\
&+\frac{\partial f_\lambda^{eq}}{\partial T}\vec{v}_\lambda \cdot \frac{\ell^2}{\kappa}(\nabla^2\vec{q} + \alpha'\vec{\nabla}(\vec{\nabla}\cdot\vec{q})) + \\
&+\vec{v}_\lambda\vec{\beta}_\lambda : \vec{\nabla}\vec{q} + \vec{v}_\lambda\vec{\gamma}_\lambda : \frac{\partial \vec{\nabla}\vec{q}}{\partial t} = \\
&= C(\vec{\beta}_\lambda)\cdot\vec{q} + C(\vec{\gamma}_\lambda)\cdot\frac{\partial \vec{q}}{\partial t} + C(\overline{\overline{G}}_\lambda) : \vec{\nabla}\vec{q}.
\end{aligned} \tag{3.21}$$

In this equation, some mesoscopic variables are not present in the distribution function (Equation (3.15)), but the higher-order derivatives can be neglected for moderate spatial and temporal variations ($\partial_t \vec{\nabla}\cdot\vec{q}$, $\partial_t \vec{\nabla}\vec{q}$, $\partial^2_{t^2}\vec{q}$, $\nabla^2\vec{q}$ and $\vec{\nabla}(\vec{\nabla}\cdot\vec{q})$). Then, all mesoscopic quantities in Equation (3.21) are independent variables, and the equation can only be satisfied if their coefficients are equal:

$$C(\vec{\beta}_\lambda) = -\frac{1}{\kappa}\frac{\partial f_\lambda^{eq}}{\partial T}\vec{v}_\lambda, \tag{3.22a}$$

$$C(\vec{\gamma}_\lambda) = \vec{\beta}_\lambda - \frac{\tau}{\kappa}\frac{\partial f_\lambda^{eq}}{\partial T}\vec{v}_\lambda, \tag{3.22b}$$

$$C(g_{1,\lambda}) = \beta_\lambda v_\lambda, \tag{3.22c}$$

$$C(g_{2,\lambda}) = -\frac{1}{C_v}\frac{\partial f_\lambda^{eq}}{\partial T}. \tag{3.22d}$$

These equations can be solved for a given collision operator, and then the microscopic solution is completed. Notice that Equation (3.22a) is the same result as obtained in Fourier's derivation (Equation (3.11)).

To obtain the heat flux relaxation time τ, in analogy to the consistency relation used for the thermal conductivity (Equation (3.13)), we have used a second consistency relation (obtained again from the microscopic expression for the heat flux $\vec{q} \equiv \int \hbar\omega_\lambda \vec{v}_\lambda f_\lambda d\lambda$):

$$\int \hbar\omega_\lambda v_\lambda \gamma_\lambda d\lambda = 0. \tag{3.23}$$

Finally, let us note that, in contrast to the present formalism, Guyer and Krumhansl [52] do not supply an explicit expression for the distribution function.

At this point, we want to explore some relevant aspects of the obtained equations in this GKE derivation.

3.3.1 Energy conservation

It is important to remark that the proposed distribution function conserves energy for general collision operators:

$$\begin{aligned}\int \hbar\omega_\lambda C(f_\lambda)d\lambda = \int \hbar\omega_\lambda C(\overline{\overline{G}}_\lambda)d\lambda : \vec{\nabla}\vec{q} = \\ \left(\frac{1}{d}\int \hbar\omega_\lambda v_\lambda \beta_\lambda d\lambda - \frac{1}{C_v}\int \hbar\omega_\lambda \frac{\partial f_\lambda^{eq}}{\partial T} d\lambda\right)\vec{\nabla}\cdot\vec{q} = 0,\end{aligned} \tag{3.24}$$

where the first equality comes from isotropy, and the last equality follows from the consistency relation Equation (3.13). This energy conservation contrasts with the RTA and Callaway's approaches, where, as mentioned above, energy conservation states additional conditions to the formalism [32, 35].

3.3.2 Non-equilibrium temperature

Typically, the energy conservation equation is of the form of $C_v\partial_t T + \vec{\nabla}\cdot\vec{q} = 0$ instead of Equation (3.19a). Nevertheless, the local equilibrium temperature is usually defined as T' satisfying that $e = e_{eq}(T')$, with $e_{eq} \equiv \int \hbar\omega_\lambda f_\lambda^{eq} d\lambda$ [43, 46,

52, 112]. Using the distribution function of Equation (3.15), we obtain the following expression for the energy,

$$e = e_{eq}(T) - \tau_e \vec{\nabla} \cdot \vec{q} = e_{eq}(T'). \tag{3.25}$$

If we assume that $T' \ll T_0$, with T_0 the reference temperature of the whole system, the energy can be linearized $e(T') = e_{eq}(T_0) + C_v(T' - T_0)$. Then, Equation (3.25) yields $\partial_t T = \partial_t T' + \frac{\tau_e}{C_v}\partial_t \vec{\nabla} \cdot \vec{q}$ and $\vec{\nabla} T = \vec{\nabla} T' + \frac{\tau_e}{C_v}\vec{\nabla}(\vec{\nabla} \cdot \vec{q})$ Notice that, in a stationary situation, $T = T'$ (see Equation (3.25)). If we substitute previous relations into Equations (3.19a) and (3.19b), we obtain that

$$C_v \frac{\partial T'}{\partial t} + \vec{\nabla} \cdot \vec{q} = 0, \tag{3.26a}$$

$$\vec{q} + \tau \frac{\partial \vec{q}}{\partial t} = -\kappa \vec{\nabla} T' + \ell^2 \left(\nabla^2 \vec{q} + \alpha \vec{\nabla}(\vec{\nabla} \cdot \vec{q}) \right), \tag{3.26b}$$

where it has been defined that

$$\alpha \equiv \alpha' - \frac{\kappa \tau_e}{C_v \ell^2}, \tag{3.27}$$

and we have used that $\tau_p^2 \frac{\partial^2 \vec{q}}{\partial t^2}$ can be neglected, as discussed in the next section. Now, Equation (3.26a) has the expected form for energy conservation. Actually, this set of equations (Equations (3.26a) and (3.26b)), along with the boundary conditions that will be derived in Section 3.4, is what we solve to reproduce experiments. Then, we assume that the temperature measured in experiments is the local equilibrium temperature T'. We will provide experimental evidence supporting these expressions in Chapter 6.

The distribution function is written in terms of the heat flux $\vec{q}$ (and its first derivatives) and the local temperature T. Nevertheless, the transport equations, Equations (3.26a) and (3.26b), are written in terms of T' instead of T. We also express the phonon distribution function in terms of T', obtaining the following expression:

$$f_\lambda = f_\lambda^{eq}(T') + \vec{\beta}_\lambda \cdot \vec{q} + \vec{\gamma}_\lambda \cdot \frac{\partial \vec{q}}{\partial t} + \left(\overline{\overline{G}}_\lambda - \frac{1}{C_v} \frac{\partial f_\lambda^{eq}}{\partial T} \int \hbar \omega_\lambda \overline{\overline{G}}_\lambda d\lambda \right) : \vec{\nabla} \vec{q}, \tag{3.28}$$

where it has been used that $\int \hbar \omega_\lambda \overline{\overline{G}}_\lambda d\lambda = -\tau_e \mathbb{1}$. By writing

the distribution function in this form, it is trivial to see that the definition of the energy results in $e = e_{eq}(T')$, which resembles a consistency relation, as in the heat flux case, because the energy projection of the distribution function is an identity.

3.3.3 τ_p on Debye's approximation with identical branches and memory effects

A comment on τ_p^2 time is necessary at this point. This parameter is related to the difference between the crystal momentum $\vec{p}$ and the heat flux $\vec{q}$. It appears because, even though consistency relations impose $\int \hbar\omega_\lambda \vec{v}_\lambda \vec{\gamma}_\lambda d\lambda = 0$ (Equation (3.23)), it is not necessary that $\int \hbar\vec{k}_\lambda \vec{\gamma}_\lambda d\lambda = 0$. These two integrals only will be identical when Debye's approximation with identical branches is considered. Under this situation, $\tau_p^2 = 0$ (see Equations (3.20c)), and the typical GKE [52] is recovered. These are precisely the assumptions made in the Guyer and Krumhansl papers [52, 74]. Then, τ_p^2 is related to how far the material is from Debye's approximation with identical branches. In general, as it is numerically shown in Figure 5.2, τ_p is found to be an order of magnitude smaller than τ for materials like silicon, germanium, and diamond, meaning that $\tau_p^2 \frac{\partial^2 \vec{q}}{\partial t^2}$ can be neglected as compared to $\tau \frac{\partial \vec{q}}{\partial t}$ except in extreme non-equilibrium situations. By considering that this is the case, from now on we will neglect this term and obtain the exact GKE for the heat flux.

3.3.4 Debye's approximation and nonlocality

When Debye's approximation is considered (it is not necessary that all the branches are identical), α does not depend on the material. Its value is

$$\alpha = \frac{d-2}{d}. \tag{3.29}$$

This result can be easily obtained from the general collision operator value obtained in Section 3.3.2 (Equation (3.27)). When considering the Debye approximation, the group velocity is $v_\lambda = \frac{\omega_\lambda}{k}$, and by using this relation, Equation (3.29) is obtained.

This expression for α has some implications. Firstly, in a three-dimensions material ($d = 3$), $\alpha = 1/3$, obtaining that

$$\vec{q} + \tau \frac{\partial \vec{q}}{\partial t} = -\kappa \vec{\nabla} T + \ell^2 \left(\nabla^2 \vec{q} + \frac{1}{3} \vec{\nabla} (\vec{\nabla} \cdot \vec{q}) \right). \tag{3.30}$$

This result for α is obtained in [57] and is at odds with the original work of Guyer and Krumhansl [52], but it agrees with [104, 112]. Hardy and Albers explained that this discrepancy is due to an approximation made in [52].

The second remarkable result is that when a two-dimensions material is considered ($d = 2$), like graphene, $\alpha = 0$, obtaining that

$$\vec{q} + \tau \frac{\partial \vec{q}}{\partial t} = -\kappa \vec{\nabla} T + \ell^2 \nabla^2 \vec{q}. \tag{3.31}$$

Finally, when considering a one-dimension material, since $\nabla^2 \vec{q} = \vec{\nabla} (\vec{\nabla} \cdot \vec{q})$ and $\alpha = -1$, the nonlocal effects are canceled, and the resulting equation is

$$\vec{q} + \tau \frac{\partial \vec{q}}{\partial t} = -\kappa \vec{\nabla} T. \tag{3.32}$$

3.4 Boundary conditions

This section provides a general procedure to derive boundary conditions for any transport equation, particularly for the GKE. One of the main problems in solving the BTE is to impose the boundary conditions for each phonon [31, 46, 115, 116]. Here, simple boundary conditions are derived in terms of the mesoscopic variables appearing on the ansatz of the phonon distribution function.

As pointed out in [57], the two main implications of the boundary conditions in the hydrodynamic equation are a heat-flux retardant in the tangential component (Section 3.4.1) and a temperature jump when an interface between two materials is considered (Section 3.4.2). These two implications are consequences of the choice of the phonon distribution function. We will use the distribution function of Equation (3.15) to be consistent with the GKE derivation.

The present derivation is based on the derivation in [57]. Nevertheless, here is the first time that the temperature jump for a general collisions operator and without Debye's approximation is presented since, in [57, 63], the derivation is under a gray model and using Debye's approximation with identical phonon branches. The main idea is based on the principle of classic kinetic theory [108, 117]: the boundary condition for a given macroscopic variable is related to the

balance of its flux at the boundary. We will designate ϕ_λ as the microscopic variable, which is integrated to obtain the conserved macroscopic magnitude. Then, the resulting equation is

$$\int_\Omega \vec{v}_\lambda \phi_\lambda f_\lambda d\lambda = \int_{\Omega^-} \vec{v}_\lambda \phi_\lambda f_\lambda^- d\lambda + \int_{\Omega^+} \vec{v}_\lambda \phi_\lambda f_\lambda^+ d\lambda \quad (3.33)$$

with Ω denoting the whole phonon space and Ω^- (Ω^+) denoting the phonon space where $\hat{v}_\lambda \cdot \hat{n} < 0$ ($\hat{v}_\lambda \cdot \hat{n} > 0$), which are the ingoing (outgoing) to the surface phonons, with $\hat{n}$ the unitary and normal-to-the-boundary vector. f_λ^- (f_λ^+) is the distribution function of the ingoing (outgoing) phonons.

Reasonably, the ingoing distribution function is the "bulk" distribution function $f_\lambda^- = f_\lambda$ (Equation (3.15)). Another important assumption is that the outgoing distribution function f_λ^+ is a linear combination of a specularly reflected ingoing distribution function and a diffusively reflected distribution:

$$f_\lambda^+ = (1-s) f_\lambda^{eq}(T_w) + s f_\lambda^-(\hat{v}_\lambda \cdot \hat{n} \rightarrow -\hat{v}_\lambda \cdot \hat{n}). \quad (3.34)$$

In the previous relation, there are two new parameters. The first one is T_w, which is the temperature of the "wall". This temperature is an instrumental parameter used to derive the boundary conditions, but it has no physical meaning and will not appear in the resulting expression. It is assumed that the phonons are emitted at this temperature when diffusive scattering occurs.

The other new parameter is the specularity s. The specularity refers to which amount of phonons have been specularly reflected. When $s \rightarrow 0$, all the phonons have been diffusively reflected; on the other hand, when $s \rightarrow 1$, all the phonons have been specularly reflected. If we consider a mode-independent s parameter, as it is the case of Equation (3.34), the value is obtained by a comparison between the wavelength of the phonons and the average height of the roughness defects η [22, 62, 90]

$$s = \frac{\int \hbar\omega_\lambda \frac{\partial f_\lambda^{eq}}{\partial T} e^{-\pi(2\eta \vec{k}_\lambda \cdot \hat{n})^2} d\lambda}{C_v}. \quad (3.35)$$

Typically, this parameter tends to vanish $s \rightarrow 0$ since the wavelengths of the phonons are much smaller than

the characteristic sizes of the roughness (for silicon, for example, is of the order of tenths of Angstroms for these experiments: [22–24, 76]). To get an insight, for silicon at room temperature, when a characteristic roughness of $\eta \approx 0.2nm$ is considered, the specularity coefficient is of the order of $s \approx 0.3$, meaning that most of the phonons are diffusively reflected. Nevertheless, this section considers a general case where s can be any value between 0 and 1.

3.4.1 Perpendicular heat-flux boundary condition. The temperature jump

In this section, the perpendicular to the surface heat flux at the boundary is derived. First, the most intuitive part is that insulation is imposed at the free surface [62],

$$\vec{q} \cdot \hat{n} = 0. \tag{3.36}$$

Nevertheless, the material is not isolated when there is no free surface. In this case, the continuity of the normal component of the heat flux is imposed,

$$\vec{q} \cdot \hat{n} = \vec{q}_M \cdot \hat{n}, \tag{3.37}$$

where the sub-index M denotes the other material of the interface. In general, this material is a metal in our simulations [63–67] (see Chapter 6 for further details).

Furthermore, we will use Equation (3.33) to fully characterize Equation (3.37). Since the energy is a conserved magnitude, it is used $\phi_\lambda = \hbar\omega_\lambda$ in Equation (3.33) and it is considered the normal-to-the-surface component of the flux

$$\int_\Omega \hbar\omega_\lambda v_{\lambda,n} f_\lambda d\lambda = \int_{\Omega^-} \hbar\omega_\lambda v_{\lambda,n} f_\lambda^- d\lambda + \int_{\Omega^+} \hbar\omega_\lambda v_{\lambda,n} f_\lambda^+ d\lambda, \tag{3.38}$$

where the sub-index n denotes the normal component. This equation is applied to the semiconductor, characterized by the distribution function of Equation (3.15). By putting it into Equation (3.38), using the consistency relations (Equations (3.13) and (3.23)), and isolating $\int_{\Omega^+} \hbar\omega_\lambda \vec{v}_{\lambda,n} f_\lambda^{eq}(T_w) d\lambda$, it is

obtained that

$$\begin{aligned}\int_{\Omega^+}\hbar\omega_\lambda\vec{v}_{\lambda,n}f_\lambda^{eq}(T_w)d\lambda = \\ \frac{1}{2}\frac{1+s}{1-s}q_n \\ +\int_{\Omega^+}\hbar\omega_\lambda v_{\lambda,n}f_\lambda^{eq}d\lambda+\int_{\Omega^+}\hbar\omega_\lambda v_{\lambda,n}G_{1,\lambda,rr}d\lambda\frac{\partial q_r}{\partial r} \\ +\int_{\Omega^+}\hbar\omega_\lambda v_{\lambda,n}G_{1,\lambda,nn}d\lambda\frac{\partial q_n}{\partial n}+\int_{\Omega^+}\hbar\omega_\lambda v_{\lambda,n}g_{2,\lambda}d\lambda\vec{\nabla}\cdot\vec{q},\end{aligned} \tag{3.39}$$

where the sub-index r denotes the tangential component. Since the equilibrium distribution function can be expressed as $f_\lambda^{eq}(T) = f_\lambda^{eq}(T_0) + \frac{\partial f_\lambda^{eq}}{\partial T}(T - T_0)$, the previous equation can be expressed as

$$\begin{aligned}T_w - T = \\ \frac{1}{2\int_{\Omega^+}\hbar\omega_\lambda v_{\lambda,n}\frac{\partial f_\lambda^{eq}}{\partial T}d\lambda}\frac{1+s}{1-s}q_n \\ +\frac{\int_{\Omega^+}\hbar\omega_\lambda v_{\lambda,n}G_{1,\lambda,rr}d\lambda}{\int_{\Omega^+}\hbar\omega_\lambda v_{\lambda,n}\frac{\partial f_\lambda^{eq}}{\partial T}d\lambda}\frac{\partial q_r}{\partial r}+\frac{\int_{\Omega^+}\hbar\omega_\lambda v_{\lambda,n}G_{1,\lambda,nn}d\lambda}{\int_{\Omega^+}\hbar\omega_\lambda v_{\lambda,n}\frac{\partial f_\lambda^{eq}}{\partial T}d\lambda}\frac{\partial q_n}{\partial n} \\ +\frac{\int_{\Omega^+}\hbar\omega_\lambda v_{\lambda,n}g_{2,\lambda}d\lambda}{\int_{\Omega^+}\hbar\omega_\lambda v_{\lambda,n}\frac{\partial f_\lambda^{eq}}{\partial T}d\lambda}\vec{\nabla}\cdot\vec{q}.\end{aligned} \tag{3.40}$$

The same procedure is done in the "metal" interface, but a different distribution function is considered in this case. Since metal is well-characterized by Fourier's law (which is dominated by electrons) [62, 64–66], it is enough to use Equation (3.4) to describe it, i.e., consider that the distribution function of the metal only depends on the heat flux, as explained in Section 3.2. Then, by using Equation (3.38) in the metal, we obtain the final expression for this boundary condition:

$$T_w - T_M = -\frac{1}{2\int_{\Omega^+}\hbar\omega_\lambda^M v_{\lambda,n}^M\frac{\partial f_\lambda^{eq,M}}{\partial T}d\lambda}\frac{1+s}{1-s}q_n, \tag{3.41}$$

assuming that the specularity s is the same at both sides of the interface. Then, by isolating the instrumental temperature

T_w and equaling both equations, it is obtained

$$T - T_M = -\frac{1}{2}C(\Gamma^{-1}+\Gamma_M^{-1})\vec{q}\cdot\hat{n}+\Gamma^{-1}\left(\overline{\overline{\chi}} : \vec{\nabla}\vec{q} - \zeta\vec{\nabla}\cdot\vec{q}\right), \quad (3.42)$$

where the next coefficients are defined

$$C \equiv \frac{1+s}{1-s}, \quad (3.43a)$$

$$\Gamma \equiv \int_{\Omega^+} \hbar\omega_\lambda v_{\lambda,n}\frac{\partial f_\lambda^{eq}}{\partial T}d\lambda, \quad (3.43b)$$

$$\overline{\overline{\chi}} \equiv -\int_{\Omega^+} \hbar\omega_\lambda v_{\lambda,n}\overline{\overline{G}}_{1,\lambda}d\lambda, \quad (3.43c)$$

$$\zeta \equiv \int_{\Omega^+} \hbar\omega_\lambda v_{\lambda,n} g_{2,\lambda}d\lambda. \quad (3.43d)$$

This result, known as temperature jump, is the same as the one obtained in [57] in steady-state or what we obtained in [63], but in both cases, it is used in a gray model. Notice that the term $(\Gamma^{-1}+\Gamma_M^{-1})/2$ is the typical result of the Diffuse Mismatch Model (DMM) or the Kapitza resistance [118, 119]. Nevertheless, this term assumes a perfect contact (i.e., on all surfaces, both materials are in contact). Therefore, it can be considered as a lower bound. The boundary resistance for a real interface is larger, even being of the same order. In [63], we obtained that $\Gamma_{exp}^{-1} = 2.71\Gamma^{-1}$, where Γ_{exp}^{-1} is the experimental value.

The additional terms of Equation (3.42) ($\Gamma^{-1}\overline{\overline{\chi}} : \vec{\nabla}\vec{q}$ and $\Gamma^{-1}\zeta\vec{\nabla}\cdot\vec{q}$) are related to the system's nonlocality. Actually, $\overline{\overline{\chi}}$ and ζ are lengths. Equations (3.43c) and (3.43d) are presented under the RTA to get a physical insight

$$\overline{\overline{\chi}} = d\frac{\left\langle v_{\lambda,n}\vec{v}_\lambda\vec{v}_\lambda\tau_\lambda^2\right\rangle_+}{\left\langle v_\lambda^2\tau_\lambda\right\rangle}, \quad (3.44a)$$

$$\zeta = \left\langle v_{\lambda,n}\tau_\lambda\right\rangle_+, \quad (3.44b)$$

where it has been defined that $\langle x_\lambda\rangle_+ \equiv \int_{\Omega^+}\hbar\omega_\lambda\frac{\partial f_\lambda^{eq}}{\partial T}x_\lambda d\lambda/C_v$. We found that these two terms generally do not have any relevant contribution [63–66]. We only expect a significant effect when extreme non-equilibrium situations are considered.

3.4.2 Tangential heat-flux boundary condition. The slip-boundary condition

As mentioned in Section 3.3, the GKE is analogous to the NSE, specifically, the $\ell^2(\nabla^2 + \alpha\vec{\nabla}\cdot\vec{q})$ terms in Equation (3.26b) and the viscous terms of the NSE. Thus, concepts such as friction and vorticity become relevant [59]. Then, in analogy with the flow of rarefied gases with large Knudsen numbers, a slip boundary condition is expected [120].

The slip boundary condition is naturally derived when applying Equation (3.33), considering the heat flux as a conserved magnitude,

$$\int_{\Omega} \hbar\omega_\lambda \vec{v}_\lambda \vec{v}_\lambda f_\lambda d\lambda = \int_{\Omega^-} \hbar\omega_\lambda \vec{v}_\lambda \vec{v}_\lambda f_\lambda^- d\lambda + \int_{\Omega^+} \hbar\omega_\lambda \vec{v}_\lambda \vec{v}_\lambda f_\lambda^+ d\lambda, \tag{3.45}$$

with the distribution function of Equation (3.15), as presented in [57, 62] for a single Debye branch ($v_\lambda = v$ = constant) and a single phonon relaxation time ($\tau_\lambda = \tau$ = constant). In this case, with a procedure completely analogous to the previous section, it is obtained that

$$q_r = C\ell \left(\nabla_n q_r + \nabla_r q_n\right), \tag{3.46}$$

which is the slip boundary condition obtained in [57, 62], but also considering the normal-to-the-surface components since we are not considering a free surface. For a free surface, we recover exactly the results in [57, 62].

3.5 Conclusions

As a summary of the chapter, we have obtained on microscopic grounds that, beyond Fourier, the next approximation of heat transport in general non-metallic substances is the hydrodynamic equation (GKE), which recovers Fourier at large scales. In contrast to general belief, it includes kinetic materials like silicon and fills the gap between extensive nanoscale experiments in kinetic substances and microscopic theory. This framework can be applied to materials both in the limit dominated by normal scattering and in the intermediate regime when normal and resistive collisions are relevant and where this formalism may shed light on the interpretation of experiments.

Another important point of the formalism is the proper derivation of the boundary conditions using kinetic theory.

With them, the distribution function and the transport equations, we have a complete picture of the thermal transport going from a microscopic to a macroscopic perspective.

Furthermore, the FDF recovers Fourier's law when considering a uniform $\vec{\nabla}T$ and a stationary situation, with the same results as found through previous methods [37]. Thus, we have validated the formalism for a known situation.

Finally, the main feature of FDF is its mathematical simplicity. With *ab initio* expressions for all the parameters, it results in a predictive model for a wide range of non-equilibrium situations. The equations used to solve the system (Equations (3.26a) and (3.26b) combined with the boundary conditions) can be implemented with finite element methods, and computational costs of this implementation are much smaller than the computational cost of directly solving the BTE.

Collective limit 4

The GKE was derived for general collisions operator, dispersion relations, and branches in the previous chapter. Nevertheless, it was originally derived by Guyer and Krumhansl in the collective regime, i.e., when $N \gg R$, and assuming a single branch and Debye approximation [52, 74]. In this regime, normal collisions strongly correlate the evolution of the populations of different phonon modes. This implies, for example, that RTA does not apply since phonon modes do not evolve independently: a detailed study of this limit requires including the off-diagonal terms in the linear collision operator C [52, 69].

In this chapter, we apply FDF to the collective limit [121], which allows us to recover Guyer and Krumhansl results under their assumptions and generalize them to several branches and general dispersion relations. The recovery of these results through this entirely different method supports the FDF.

In addition, we obtain a refined expression for the phonon distribution function in this regime. Typically, when normal collisions dominate, it is considered that the distribution function is the displaced one [7, 43, 52, 57, 69, 74, 106, 111–113], which, as mentioned, describes a collective motion of phonons that seem to move at the same drift velocity $\vec{u}$. Our phonon distribution function differs from the displaced one because of the non-null coefficients accounting for the memory and nonlocal effects (i.e., $\vec{\gamma}_\lambda$ and $\overline{\overline{G}}_\lambda$ of Equation (3.15) in the collective limit are not zero). Even though these coefficients may be small, they are necessary for a consistent

and complete description of the collective limit, as will be seen in Section 4.1. This generalization of the phonon distribution function in the collective limit will also allow us to solve a long-standing issue about the velocity of second sound in this limit.

The chapter is organized as follows: in Section 4.1, we derive the phonon distribution function in the collective limit. In Section 4.2, we use the distribution function to obtain the transport coefficients in this regime. Finally, in Section 4.3, we analyze the second-sound velocity in collective materials.

4.1 Non-equilibrium distribution function

The objective of this section is to derive the phonon distribution function in the collective limit. According to FDF, if the phonon distribution function is simply the displaced one, it would not generate nonlocal effects. This is because they are related to the first derivatives of the heat flux appearing on the distribution function. In that case, the results would be analogous to the ones obtained in Section 3.2, where Fourier's law is recovered.

FDF postulates that the distribution function depends on the heat flux and its derivatives as given by Equation (3.15), with the weight functions being the solutions of Equations (3.22a)-(3.22d). To determine these weights in the collective limit, we will use that, in the limit where resistive collisions are absent, in stationary and homogeneous situations, the solution of the BTE is the displaced (or drifting) Bose-Einstein distribution [90, 99] (Equation (2.13)), as mentioned above.

On the other hand, under stationary and homogeneous conditions, the ansatz of Equation (3.15) simplifies to $f_\lambda = f_\lambda^{eq} + \vec{\beta}_\lambda \cdot \vec{q}$. This has the same form as Equation (2.13). This yields the heat flux $\vec{q} \propto \vec{u}$, which allows identifying $\vec{\beta}_\lambda$ in the collective limit as

$$\vec{\beta}_\lambda^{col} = \frac{d}{C_v \left\langle \frac{v_\lambda}{v_{p,\lambda}} \right\rangle} \frac{\vec{k}}{\omega_\lambda} \partial_T f_\lambda^{eq}. \tag{4.1}$$

Notice that this equation is applied to systems of different dimensions d and, in particular, to 2D materials ($d = 2$) like graphene, where normal collisions are dominant [54].

The other weight functions can be evaluated by taking

into account that in the limit $N \gg R$, one can approximate the collision operator acting on function x_λ as $C(x_\lambda) \simeq N(x_\lambda) \simeq -\frac{x_\lambda}{\tau_{N,\lambda}}$, with $\tau_{N,\lambda}$ the relaxation time for the normal scattering of the λ-mode and $x_\lambda = \vec{\gamma}_\lambda$, $g_{1,\lambda}$, and $g_{2,\lambda}$. Let us note, however, that this does not apply to $\vec{\beta}_\lambda^{col}$ since N conserves momentum, and then $N(\vec{\beta}_\lambda^{col}) = N(f_\lambda^d) = 0$. By using Equations (3.22b)-(3.22d), one has

$$\vec{\gamma}_\lambda = \tau_{N,\lambda}\left(\frac{\tau}{\kappa}\frac{\partial f_\lambda^{eq}}{\partial T}\vec{v}_\lambda - \vec{\beta}_\lambda^{col}\right) + D\vec{\beta}_\lambda^{col} \tag{4.2a}$$

$$\overline{\overline{G}}_{1,\lambda} = -\tau_{N,\lambda}\vec{\beta}_\lambda^{col}\vec{v}_\lambda \tag{4.2b}$$

$$g_{2,\lambda} = \frac{\tau_{N,\lambda}}{C_v}\frac{\partial f_\lambda^{eq}}{\partial T}. \tag{4.2c}$$

The last term in Equation (4.2a) is introduced because the integration of $\vec{\gamma}_\lambda$ in this limit is determined aside from a function proportional to $\vec{\beta}_\lambda^{col}$ because $N(\vec{\beta}_\lambda^{col}) = 0$. Transport coefficients τ and κ are determined below (Section 4.2), and coefficient D is subsequently obtained by the constraint of Equation (3.23). All weights are thus specified.

We now compare these results to Guyer and Krumhansl's [52] (developed in Section 2.2.4) to remark on the differences between the two formalisms. In their derivation, the authors expressed the distribution function in terms of the eigenvectors of the symmetrized normal scattering operator. Since only two of these eigenvectors are known (the ones related to the energy and crystal momentum), they could only find explicit expressions for the first terms of the expansion. This gives the displaced distribution Equation (2.13) or, equivalently, $f_\lambda^{eq} + \vec{\beta}_\lambda \cdot \vec{q}$, but not the higher order terms. Our formalism, instead, provides higher order corrections in terms of the flux derivatives, Equation (3.15), with explicit expressions for the weights. One might think that these corrections, which are of order $\tau_{N,\lambda}$, are small and could be neglected. Instead, let us stress that they are necessary for a consistent and complete description of the collective limit, as previously mentioned, like thermal viscosity or the proper definition of second sound velocity.

4.2 Transport coefficients

Our purpose now is to evaluate the transport coefficients by introducing the weights calculated above in the general expressions of the formalism, Equations (3.20a)-(3.20f), and compare them to previous work.

As we commented previously, since crystal momentum is conserved in normal collisions, i.e., $\int \hbar\vec{k}_\lambda N(f_\lambda)d\lambda = 0$, below, we use that $\int \hbar\vec{k}_\lambda C(x_\lambda)d\lambda = \int \hbar\vec{k}_\lambda R(x_\lambda)d\lambda$, for any weight function component x_λ.

4.2.1 Relaxation time, τ

The general expression for τ, Equation (3.20b), gives in the collective regime

$$\tau = \frac{\int \hbar k_\lambda R(\gamma_\lambda^{col})d\lambda - \int \hbar k_\lambda \beta_\lambda^{col} d\lambda}{\int \hbar k_\lambda R(\beta_\lambda^{col})d\lambda}. \tag{4.3}$$

Since in this regime $R \longrightarrow 0$, one has $\int \hbar k_\lambda R(\gamma_\lambda)d\lambda \ll \int \hbar k_\lambda \beta_\lambda d\lambda$, and the heat flux relaxation time is

$$\tau = -\frac{\int \hbar k_\lambda \beta_\lambda^{col} d\lambda}{\int \hbar k_\lambda R(\beta_\lambda^{col})d\lambda} \equiv -R_{11}^{*-1}, \tag{4.4}$$

which is an average resistive scattering rate. The notation R_{11}^* follows the original one by Guyer and Krumhansl [52] since it can be seen that the quotient in Equation (4.4) can be written as $R_{11}^* \equiv <1_x|\mathbf{R}^*|1_x>$, i.e., the component of the symmetrized Resistive collision operator $\mathbf{R}^*$ projected to the normalized eigenvector $|1_x>$ of the symmetrized Normal scattering operator $\mathbf{N}^*$ (see Appendix B for the definitions of symmetrized operators and eigenvectors of $\mathbf{N}^*$). This is also the result found by Guyer and Krumhansl. When one approximates $R \simeq -\frac{1}{\tau_{R,\lambda}}$, then $\tau = <1_x|\frac{1}{\tau_{R,\lambda}}|1_x>^{-1}$, which is the most common expression used for the relaxation time in the collective limit [52, 54, 74].

4.2.2 Thermal conductivity, κ

The general expression for the thermal conductivity (Equation (3.20d)) yields

$$\kappa = -\frac{\int \hbar k_\lambda v_\lambda \partial_T f_\lambda^{eq} d\lambda}{\int \hbar k_\lambda R(\beta_\lambda^{col}) d\lambda}, \tag{4.5}$$

and using expression Equation (4.4) for τ and Equation (4.1) for β_λ^{col} it can be rewritten as

$$\kappa = \frac{1}{d} C_v \left\langle \frac{v_\lambda}{v_{p,\lambda}} \right\rangle^2 \left\langle v_{p,\lambda}^{-2} \right\rangle^{-1} \tau. \tag{4.6}$$

This is the general expression for the thermal conductivity in the collective limit for arbitrary dimensions.

Furthermore, suppose one considers the Debye approximation and a single phonon branch with velocity v in 3D, as assumed in the original work of Guyer and Krumhansl. Then, one has $\kappa = \frac{1}{3} C_v v^2 \tau$, which is the result obtained in [52].

4.2.3 Non-local length, ℓ

Introducing Equation (4.2b) into Equation (3.20e) yields

$$\ell^2 = -\frac{1}{d+2} \frac{\int \hbar k_\lambda v_\lambda^2 \beta_\lambda^{col} \tau_{N,\lambda} d\lambda}{\int \hbar k_\lambda R(\beta_\lambda^{col}) d\lambda}. \tag{4.7}$$

By using Equation (4.4), it can be written in terms of eigenvectors $|1_x>$ as

$$\ell^2 = <1_x| v_y^2 \tau_{N,\lambda} |1_x> \tau. \tag{4.8}$$

Interestingly, this result agrees with [29], obtained using Callaway's model. The latter expression provides microscopic insight into the physical meaning of ℓ and the difference between the NSE and the GKE. In fluids, particles conserve momentum, while resistive scattering does not, and as we discuss below, this is responsible for a characteristic length ℓ in phonons.

According to the GKE, the thermal viscous diffusivity is given by $\nu = \ell^2/\tau$. Equation (4.8) sets that ν is simply given by an average on $v_y^2 \tau_N$, which reflects the physical origin of the diffusion of heat flux and momentum in this limit, namely normal scattering. In contrast to fluids, where momentum

is conserved, resistive collisions destroy momentum so that it diffuses only a finite time of order τ. This results in a transport equation for phonons characterized by the length diffused by momentum before being destroyed, which is approximately $\nu\tau = \ell^2$.

In terms of averages, in d dimensions the nonlocal length writes as

$$\ell^2 = \frac{1}{d+2}\left\langle \frac{v_\lambda^2}{v_{p,\lambda}^2}\tau_N \right\rangle \left\langle v_{p,\lambda}^{-2} \right\rangle^{-1} \tau. \tag{4.9}$$

A single Debye branch in 3D yields $\ell^2 = \frac{1}{5}v^2 \langle \tau_{N,\lambda} \rangle \tau$, as obtained by Guyer and Krumhansl [52, 74].

4.2.4 Time parameter τ_e

Substituting Equations (4.2b) and (4.2c) in Equation (3.20a) gives

$$\tau_e = \frac{\left\langle \frac{v_\lambda}{v_{p,\lambda}}\tau_{N,\lambda} \right\rangle - \left\langle \frac{v_\lambda}{v_{p,\lambda}} \right\rangle \langle \tau_{N,\lambda} \rangle}{\left\langle \frac{v_\lambda}{v_{p,\lambda}} \right\rangle}. \tag{4.10}$$

One finds that in the Debye approximation, $\tau_e = 0$ and generally it is of order $\langle \tau_{N,\lambda} \rangle$. Consequently, condition $(T - T')/T = \omega\tau_e \Delta T/T \ll 1$ is safely satisfied for $\omega \langle \tau_{N,\lambda} \rangle < 1$, which is already a condition for the collective regime. Namely, the timescale of experiments must be larger than normal scattering times [69, 74, 112].

4.2.5 α-parameter

In d dimensions, one has

$$\alpha = 2 - \frac{d+2}{d}\frac{\left\langle \frac{v_\lambda}{v_{p,\lambda}}\tau_{N,\lambda} \right\rangle}{\left\langle \frac{v_\lambda^2}{v_{p,\lambda}^2}\tau_{N,\lambda} \right\rangle}\left\langle \frac{v_\lambda}{v_{p,\lambda}} \right\rangle - \frac{\kappa\tau_e}{C_v\ell^2}. \tag{4.11}$$

In Debye approximation, one gets $\alpha = \frac{d-2}{d}$, as mentioned in Section 3.3.2, which is a different result from the Guyer and Krumhansl work, where they obtain $\alpha = 2$ [52].

4.2.6 Time parameter τ_p

According to Equation (3.20c), τ_p directly vanishes for identical Debye branches because of constraint Equation (3.23),

in agreement with Guyer and Krumhansl. For general dispersion relations, it can be written as $\tau_p^2 = \tilde{\tau}_N \tau$ by defining

$$\tilde{\tau}_N = \frac{\int \hbar \gamma_\lambda^{col} k_\lambda d\lambda}{\int \hbar k_\lambda \beta_\lambda^{col} d\lambda}. \tag{4.12}$$

The latter is a difference of two averages of $\tau_{N,\lambda}$, so $\tilde{\tau}_N$ is of order $\langle \tau_{N,\lambda} \rangle$ (indeed smaller). Then, the quotient of the second and first-time derivative terms in Equation (3.26b) is $\omega \tau_p^2 / \tau \approx \omega \langle \tau_N \rangle$. This is much smaller than 1 in the collective limit, so the second time derivative can be neglected, and one recovers the GKE.

4.3 Second-sound velocity in the collective limit

Second sound is the propagation of heat in the form of waves, as first sound is the wave propagation of momentum or density disturbances. These waves have been experimentally observed in some solids at cryogenic temperatures [122–124] and more recently in graphite below 200 K [61, 125]. In these cases, normal collisions dominate, which is the expected regime for second sound to be detected [69, 74]. Recently, however, we have observed second sound in germanium at room temperature [66], where resistive collisions are very important. Despite this, in this section, we focus on second sound in the collective limit.

Quite surprisingly, in this limit, two expressions for the velocity of second sound have been used in the literature [28, 54, 55, 69] coming each from different approximations of the BTE, the so-called drifting and driftless approximations. Remarkably, they lead to different results, and the differences are especially important in low-dimensional materials. We are thus faced with two different predictions for the same experimental situation, i.e., the speed of second sound in the collective limit. It is thus both theoretically and experimentally relevant to solve this conflict.

In this section, we will show that a proper analysis of the BTE predicts just a single velocity for second sound in the collective limit, thus solving the conundrum [121]. In the following, it is presented the derivations leading to the drifting and driftless expressions for the second sound speed, and then shows how the FDF solves the paradox.

Drifting and driftless approximations use the energy

conservation equation and assume that the phonon distribution function tends to the displaced distribution in the limit of negligible resistive scattering. The conflict comes from two possibilities of projecting the BTE to obtain macroscopic equations: either on the crystal momentum (drifting approximation) or the heat flux (driftless approximation) [55, 69].

4.3.1 Drifting approximation

In this limit, crystal momentum is conserved, so the BTE leads to the following balance for energy and momentum

$$\frac{\partial e}{\partial t} + \vec{\nabla} \cdot \vec{q} = 0 \tag{4.13a}$$

$$\frac{\partial \vec{p}}{\partial t} + \vec{\nabla} \cdot \overline{\overline{\Pi}} = 0. \tag{4.13b}$$

Introducing the displaced distribution (Equation (2.12)) in the e, $\vec{q}$, $\vec{p}$, and $\overline{\overline{\Pi}}$ expressions yields

$$C_v \frac{\partial T}{\partial t} + \frac{T}{d} C_v \left\langle \frac{v_\lambda}{v_{p,\lambda}} \right\rangle \vec{\nabla} \cdot \vec{u} = 0 \tag{4.14a}$$

$$\frac{T}{d} C_v \left\langle \frac{1}{v_{p,\lambda}^2} \right\rangle \frac{\partial \vec{u}}{\partial t} + \frac{1}{d} C_v \left\langle \frac{v_\lambda}{v_{p,\lambda}} \right\rangle \vec{\nabla} T = 0. \tag{4.14b}$$

The combination of these equations supplies a wave equation for temperature (and for the drift velocity) with propagation speed

$$v_{drift}^2 = \frac{1}{d} \frac{\left\langle \frac{v_\lambda}{v_{p,\lambda}} \right\rangle^2}{\left\langle \frac{1}{v_{p,\lambda}^2} \right\rangle} \tag{4.15}$$

The Debye approximation in 3 dimensions yields

$$v_{drift}^2 = \frac{1}{3} \left\langle \frac{1}{v_{p,\lambda}^2} \right\rangle^{-1}. \tag{4.16}$$

For identical branches, it gives $v_{drift}^2 = v^2/3$, with v the first sound velocity [52, 69].

4.3.2 Driftless approximation

If instead of projecting the BTE on the quasimomentum, one projects it on the heat flux, one gets a balance for the heat flux

$$\frac{\partial \vec{q}}{\partial t} + \vec{\nabla} \cdot \bar{\bar{Q}} = \int \hbar \omega_\lambda \vec{v}_\lambda N(f_\lambda) d\lambda, \tag{4.17}$$

with $\bar{\bar{Q}} = \int \hbar \omega_\lambda \vec{v}_\lambda \vec{v}_\lambda f_\lambda d\lambda$ the flux of the heat flux. For the displaced distribution, the right-hand side of Equation (4.17) vanishes since $N(f_\lambda^d)$ is identically null. Combining the previous equation with the energy conservation yields a wave equation for temperature, but now with a different velocity

$$v_{dless}^2 = \frac{1}{d} \left\langle v_\lambda^2 \right\rangle. \tag{4.18}$$

In [69], this expression for the second sound velocity is derived without assuming that the distribution function is the drifting one, thus the name of driftless velocity. In Debye's approximation, it yields in 3 dimensions,

$$v_{dless}^2 = \frac{1}{3} \left\langle v_{\lambda,p}^2 \right\rangle, \tag{4.19}$$

which is different from Equation (4.16) except for identical branches [69].

Figure 4.1 highlights the differences between drifting and driftless velocities for graphene obtained from Equations (4.15) and (4.18), which differ in a factor of around 2 as found for carbon nanotubes [55].

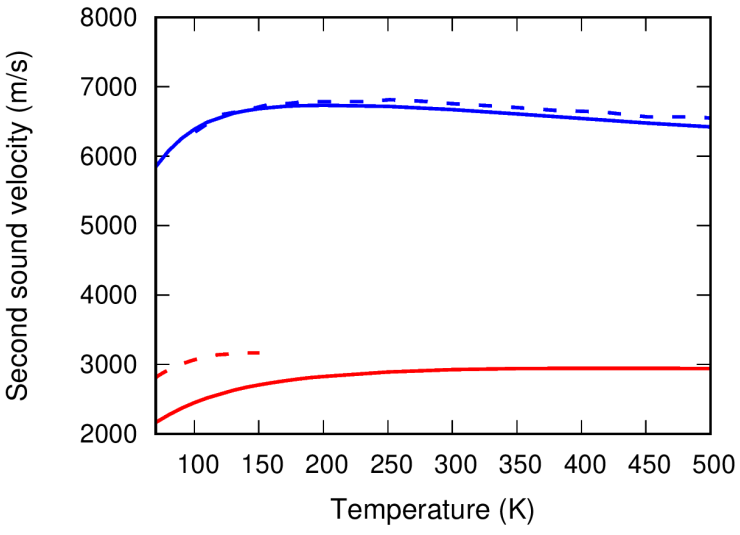

Figure 4.1: Second sound velocities for graphene for drifting (red solid line) and driftless (blue solid line) expressions at different temperatures. The drifting results are compared with the results in [54] (red dashed line) and the driftless results with the results in [28] (blue dashed line). *Image extracted from [121].*

4.3.3 Flux derivatives formalism

In our framework, the heat flux obeys the GKE. In the ideal collective limit, where resistive scattering can be neglected ($\tau \to \infty$) and $\tau_N \to 0$, it reduces to

$$\tau \frac{\partial \vec{q}}{\partial t} + \kappa \vec{\nabla} T' = 0. \tag{4.20}$$

Combined with energy conservation, it yields a thermal wave equation with a second sound velocity given by

$$v_{SS}^2 = \frac{\kappa}{C_v \tau}. \tag{4.21}$$

Using the expression for κ in the previous section (Equation (4.6)), one finds

$$v_{SS} = v_{drift}. \tag{4.22}$$

Then, the FDF supplies the drifting second sound velocity in the collective limit.

This is the same result as with the direct numerical solution of the BTE: for graphene ribbons obtains a velocity for second sound in the collective limit which coincides with the drifting velocity [126].

Then, we show how our formalism [121] allows understanding: i) why the driftless approximation supplies a wrong prediction; and ii) that a proper analysis of the heat flux projection also predicts for the second-sound speed the *drifting* (not driftless) velocity.

In the driftless derivation, the right-hand side of Equation (4.17) identically vanishes so that the heat flux is conserved. This result is a bit surprising because a normal collision conserves quasimomentum $\hbar\vec{k}$ but not the heat flux $\hbar\omega_\lambda \vec{v}_\lambda$. For instance, in a three-phonon normal collision, one generally has $\omega_1\vec{v}_1 + \omega\vec{v}_2 \neq \omega_3\vec{v}_3$. Two conditions are necessary for equality to hold generally: linear dispersion relations (Debye approximation) and identical branches. Aside from this particular case, the energy flux generally changes direction after a normal collision. This feature has been noticed previously and led the authors of [55] to prefer the drifting velocity to the driftless solution in their analysis.

Let us note, however, that the no conservation of $\hbar\omega_\lambda\vec{v}_\lambda$ in collisions is not necessarily in contradiction with that the integral $\int \hbar\omega_\lambda \vec{v}_\lambda N(f_\lambda) d\lambda$ vanishes, i.e., the sum of heat flux variations for all collisions in a given position could still be zero so that the total heat flux $\vec{q}$ would still be a conserved

macroscopic quantity. This apparently improbable situation is actually what happens for homogeneous and stationary cases, as shown by Peierls [127], since then the solution of the BTE is the displaced distribution and $N(f_\lambda^d) = 0$; in this case, a uniform heat flux is maintained without a temperature gradient [90].

The key issue in our study [121] is whether the heat flux $\vec{q}$ is conserved in unsteady and inhomogeneous situations, such as in wave propagation. Our formalism sheds light on this point. According to the FDF, the distribution function is given by Equation (3.15), so the heat source term in Equation (4.17) yields

$$\int \hbar\omega_\lambda \vec{v}_\lambda N(\vec{\beta}_\lambda) d\lambda \cdot \vec{q} + \int \hbar\omega_\lambda \vec{v}_\lambda N(\vec{\gamma}_\lambda) d\lambda \cdot \frac{\partial \vec{q}}{\partial t}. \quad (4.23)$$

The term in $\overline{\overline{G}}_\lambda$ vanishes by symmetry in isotropic systems. In the collective limit, the first term vanishes because $N(\vec{\beta}_\lambda^{col}) \propto N(f_\lambda^d) = 0$, as in the driftless derivation. However, the last term survives, and, as a result, the heat flux *is not* generally conserved in unsteady situations, at variance with the driftless derivation. This explains why this approach provides wrong predictions for the velocity of second sound.

There is yet to be seen whether the inclusion of the source term in the heat flux equation solves the conflict, i.e., whether the heat flux projection predicts for second sound the drifting velocity obtained through the momentum projection. The source term can be easily evaluated with the help of the general equation for $C(\vec{\gamma}_\lambda)$, Equation (3.22b), which yields

$$\int \hbar\omega_\lambda \vec{v}_\lambda C(\vec{\gamma}_\lambda) d\lambda = \mathbb{I} - \frac{\tau}{\kappa} \int \hbar\omega_\lambda \vec{v}_\lambda \vec{v}_\lambda \frac{\partial f_\lambda^{eq}}{\partial T}, \quad (4.24)$$

where constraint for $\vec{\beta}_\lambda$, Equation (3.13), has been used. Introducing the non-equilibrium phonon distribution, Equation (3.15), in the expression for the flux of the heat flux, $\overline{\overline{Q}}$, can be approximated in this (collective and infinite medium) limit to the local equilibrium one up to terms of order $\omega_\lambda \tau_{N,\lambda}$. The Flux derivatives formalism thus gives the balance equation of the heat flux

$$\frac{\partial \vec{q}}{\partial t} + \frac{1}{d} C_v \left\langle v_\lambda^2 \right\rangle \vec{\nabla} T = \left(1 - \frac{\tau}{d\kappa} C_v \left\langle v_\lambda^2 \right\rangle\right) \frac{\partial \vec{q}}{\partial t}. \quad (4.25)$$

Remarkably, terms cancel out, and one is left with Equation (4.20). We thus recover a wave equation with the *drifting* speed for second sound, in agreement with the drifting derivation as consistency is required.

4.3.4 Discussion

The derivation above shows that the origin of the error in the driftless derivation was to assume that the displaced distribution was a good approximation for the distribution function in the collective limit. It is the inclusion of the term in $\partial\vec{q}/\partial t$ in the distribution function that allows solving the inconsistency. This underlines the pertinence of using this macroscopic quantity as an independent variable in the nonequilibrium phonon distribution, as assumed in the FDF. Indeed, both the driftless and drifting derivations above assume the displaced phonon distribution. Despite this is not correct in unsteady or inhomogeneous situations in none of these cases. Nevertheless, the drifting derivation provides good results because momentum conservation in normal collision gets rid of the term in heat flux time derivative, in contrast to what happens when projecting on the energy flux.

Interestingly, we have obtained a closed expression for the source term in the heat flux balance equation, Equation (4.25). It shows that when resistive scattering can be neglected, the heat flux is a conserved quantity in stationary situations, not only for the homogeneous case, as studied by Peierls, but also for inhomogeneous ones, as in stationary Poiseuille flow, where $\vec{q}$ is only destroyed at boundaries. In unsteady situations, it is helpful to write the source term as $(1-v_{dless}^2/v_{drift}^2)\partial\vec{q}/\partial t$. Since both velocities are generally different, the source term does not vanish, and $\vec{q}$ is not conserved. Nevertheless, it becomes null for linear dispersion and identical branches, in agreement with the conservation of $\hbar\omega\vec{v}$ in each collision discussed above. Typically, $v_{dless} > v_{drift}$ (see for instance Equations (4.16) and (4.19), or [55]) so that the prefactor of $\partial\vec{q}/\partial t$ is negative. Notice however that the source term has not a definite sign. In a thermal wave, for instance, $\partial\vec{q}/\partial t$ changes the sign and the source term with it. Accordingly, at any point in space, the heat flux is created and destroyed periodically by normal collisions. Thus, the effect of normal collisions is not to destroy heat flux but to introduce a delay in the heat flux.

Let us finally comment that Hardy introduced the driftless second sound velocity by assuming a general odd perturbation describing situations not restricted to the collective limit [69]. Then the phonon distribution is not necessarily the displaced one, thus the name driftless second sound. Hardy considered a RTA model (therefore out from the collective limit) with a constant relaxation time in his heuristic derivation. Our model also yields the driftless second sound speed under these approximations since, in RTA, $\kappa = \frac{1}{d} C_v \left\langle v_\lambda^2 \right\rangle \tau$. However, our model is not restricted to these approximations, and it generally sets $v_{SS}^2 = \frac{\kappa}{C_v \tau}$.

Finally, we present some conclusions. First, we have applied FDF to the collective limit [121]. When considering the approximations done by Guyer and Krumhansl in the original work [52], we recover the same results but extend them to general dispersion relations. Thus, we have theoretical support of the FDF in the collective limit. Furthermore, we have demonstrated the need to include the first derivatives of the heat flux in the phonon distribution function. This allows the conciliation of the drifting and driftless velocities, and concludes that the displaced distribution function is insufficient to completely describe systems in the collective limit.

Kinetic limit and intermediate regimes

5

The primary motivation of this thesis was to provide a theoretical foundation for the GKE in kinetic materials like silicon. In Chapter 3, we have provided a derivation of the GKE for the general collisions operator. In this chapter, we will apply these results to the RTA [70] and Callaway's approximation.

As mentioned in Section 2.2.1, RTA is a paradigmatic example of kinetic materials, and also, with this approximation, we obtain the GKE with relevant nonlocal effects. This is at odds with a recent macroscopic model obtained from the BTE [43], where they obtain negligible viscous effects for kinetic materials. Furthermore, the simplicity of the RTA will allow us to obtain explicit equations for the transport parameters and, then, to obtain a physical interpretation of its expressions. Thus, we will also provide numerical values for all these parameters using *ab initio* techniques. This will check the validity of the FDF and its GKE derivation in materials where resistive collisions dominate.

We will also apply the FDF to Callaway's approximation. The objective is to obtain expressions for the transition between kinetic and collective materials and recover the expressions of the RTA and the collective cases in the limits to validate it.

The chapter is organized as follows: in Section 5.1, we will derive the GKE for kinetic materials, and in Section 5.2, we will do it under Callaway's approximation. In both cases, we will provide explicit expressions for the phonon distribution function, the transport parameters, and their

values through *ab initio* techniques.

5.1 Kinetic limit: the Relaxation Time Approximation solution

In Section 3.3, we have derived the GKE with a general linearized collisions operator for moderate Knudsen numbers. This means that, in contrast to common belief, the hydrodynamic equation is recovered, whatever the collision operator it is. Thus, also, in the kinetic limit, where resistive collisions dominate, the GKE is predicted, and it is not necessary that normal collisions dominate.

In the present section, a paradigmatic example of the kinetic limit, the RTA [35], is used to obtain the GKE with explicit expressions for the distribution function and the transport parameters [70]. This limit has proved to compare well with experimental thermal conductivities in bulk silicon and germanium in a wide temperature range [95], which is of great interest in technological applications. In Appendix E, we present an alternative derivation of this kinetic limit with the same results as in the present RTA derivation.

To do so, results in Section 3.3 for the general collisions operator are used in the RTA, which is the collisions operator in Equation (2.10). Then, the complete distribution function is obtained by using Equations (3.22a)-(3.22d):

$$\begin{aligned} f_\lambda = f_\lambda^{eq} + \frac{\tau_\lambda}{\kappa}\frac{\partial f_\lambda^{eq}}{\partial T}\vec{v}_\lambda \cdot \vec{q} + \frac{\tau_\lambda(\tau-\tau_\lambda)}{\kappa}\frac{\partial f_\lambda^{eq}}{\partial T}\vec{v}_\lambda \cdot \frac{\partial \vec{q}}{\partial t} \\ - \frac{\tau_\lambda^2}{\kappa}\frac{\partial f_\lambda^{eq}}{\partial T}\vec{v}_\lambda\vec{v}_\lambda : \vec{\nabla}\vec{q} + \frac{\tau_\lambda}{C_v}\frac{\partial f_\lambda^{eq}}{\partial T}\vec{\nabla}\cdot\vec{q}. \end{aligned} \tag{5.1}$$

To our knowledge, this expression is the first simple expression for the phonon distribution under unsteady inhomogeneous conditions in terms of first-principle quantities [70]. Interestingly, when considering a mode-independent relaxation time ($\tau_\lambda = \tau_0 =$ constant) and identical Debye branches ($v_\lambda = v =$ constant), Equation (5.1) yields the distribution function obtained in [57] through a regularized Grad's method.

The transport parameters are also directly obtained when an explicit expression for the collision operator is assumed. In this case, using Equations (3.20a)-(3.20f) and

Equation (3.27), we obtain:

$$\tau = \frac{\left\langle v_\lambda^2 \tau_\lambda^2 \right\rangle}{\left\langle v_\lambda^2 \tau_\lambda \right\rangle}, \tag{5.2a}$$

$$\tau_p^2 = \frac{\left\langle v_\lambda^2 \tau_\lambda^2 \right\rangle \left\langle \frac{v_\lambda}{v_{p,\lambda}} \tau_\lambda \right\rangle}{\left\langle v_\lambda^2 \tau_\lambda \right\rangle \left\langle \frac{v_\lambda}{v_{p,\lambda}} \right\rangle} - \frac{\left\langle \frac{v_\lambda}{v_{p,\lambda}} \tau_\lambda^2 \right\rangle}{\left\langle \frac{v_\lambda}{v_{p,\lambda}} \right\rangle}, \tag{5.2b}$$

$$\kappa = \frac{1}{d} C_v \left\langle v_\lambda^2 \tau_\lambda \right\rangle, \tag{5.2c}$$

$$\ell^2 = \frac{1}{d+2} \frac{\left\langle \frac{v_\lambda}{v_{p,\lambda}} v_\lambda^2 \tau_\lambda^2 \right\rangle}{\left\langle \frac{v_\lambda}{v_{p,\lambda}} \right\rangle}, \tag{5.2d}$$

$$\begin{aligned} \alpha = 2 &- \frac{d+2}{d} \frac{\left\langle v_\lambda^2 \tau_\lambda \right\rangle \left\langle \frac{v_\lambda}{v_{p,\lambda}} \tau_\lambda \right\rangle}{\left\langle \frac{v_\lambda}{v_{p,\lambda}} v_\lambda^2 \tau_\lambda^2 \right\rangle} \\ &- \frac{d+2}{d} \frac{\left\langle \frac{v_\lambda}{v_{p,\lambda}} \right\rangle \left(\left\langle v_\lambda^2 \tau_\lambda^2 \right\rangle - \left\langle v_\lambda^2 \tau_\lambda \right\rangle \left\langle \tau_\lambda \right\rangle \right)}{\left\langle \frac{v_\lambda}{v_{p,\lambda}} v_\lambda^2 \tau_\lambda^2 \right\rangle}, \end{aligned} \tag{5.2e}$$

From these equations, there are some points to remark on. First, the expected thermal conductivity under the RTA is recovered. Second, the nonlocal length ℓ is an average of the phonon MFPs. This implies that even in the kinetic regime, the nonlocal length can play an important role in the description of the system. In the Debye approximation with a mode-independent relaxation time, it yields $\ell^2 = \Lambda^2/(d+2)$, with Λ the mode-independent MFP, as found by Guo and Wang [57]. The values for different materials of the nonlocal length using Equation (5.2d) are plotted in Figure 5.1. The results are very similar to the KCM prediction.

Another remarkable result comes from the heat-flux relaxation time. Usually, τ is considered as $\tau_\kappa \equiv d\kappa/(C_v \left\langle v_\lambda^2 \right\rangle)$, which is the time appearing on the thermal conductivity. This expression, under the RTA, gives $\tau_\kappa = \left\langle v_\lambda^2 \tau_\lambda \right\rangle / \left\langle v_\lambda^2 \right\rangle$. The present result (Equation (5.2a)) is substantially different. A numerical comparison between τ and τ_κ will be seen in Appendix A, where it is observed that $\tau \gg \tau_\kappa$, which implies that memory effects appear at larger time scales than typically expected. Furthermore, it also can be observed that $\tau^2 \gg \tau_p^2$,

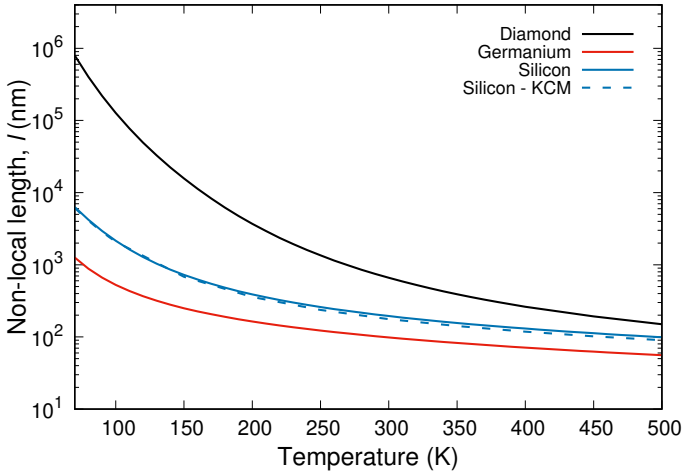

Figure 5.1: Nonlocal length under the RTA for different materials (diamond, germanium, and silicon) for a range of temperatures from 70 K to 500 K. Silicon is compared with the KCM prediction. The *ab initio* calculations are described in Appendix A.

which means that, in general, the contribution of $\tau_p^2 \frac{\partial^2 \vec{q}}{\partial t^2}$ is negligible. A comparison of τ and τ_p and the α parameter, using *ab initio* calculations, is in Figure 5.2.

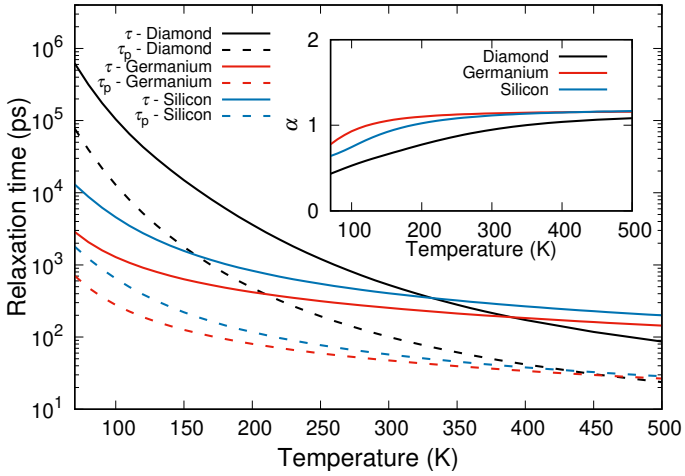

Figure 5.2: Heat flux relaxation time τ, τ_p, and the α parameter under the RTA for different materials (diamond, germanium, and silicon) for a range of temperatures from 70 K to 500 K. The value of τ_p is an order of magnitude lower than τ. The *ab initio* calculations are described in Appendix A.

In conclusion, we have demonstrated that the GKE can be derived in the kinetic limit, in contrast to the common belief: the transport parameters related to the nonlocal and memory effects are non-negligible. For example, as shown in Figure 5.1, the nonlocal length is of the order of hundreds of nanometers at room temperature. Then, when experimental sizes reduce to the order of microns, we can observe these effects. Extensive experimental validation in kinetic materials of these parameters will be shown in Chapter 6.

Nevertheless, the results obtained in the present section are not valid for materials where normal collisions play an important role. Contrarily, in Chapter 4, we have provided the derivation in the collective limit. Thus, we have both limits. To obtain a transition between them, we will apply Callaway's collisions operator in the next section. This will

allow us to obtain physical insight into intermediate regimes and observe the contribution of normal collisions to the parameters of the GKE and the distribution function.

5.2 Intermediate regimes: the Callaway's solution

The GKE was first derived in the collective limit [52] (Chapter 4), and we have derived it in the kinetic limit [70] (in the previous section). Nevertheless, there is no derivation for intermediate regimes, apart from the general collisions operator, which can not provide explicit expressions for the parameters or the distribution function. In this section, we will use Callaway's collisions operator to capture the effects of the normal collisions for those materials where there is no clear dominance of normal nor resistive collisions. Then, we provide a physical insight into the interplay between these scatterings, and thus, we obtain an interpolation between kinetic and collective regimes.

To do so, we will use FDF following some of the steps presented in the original work of Callaway [27]. The collisions operator proposed, already presented in Equation (2.14) and rewritten here to be more clear, is

$$C(f_\lambda) = -\frac{f_\lambda - f_\lambda^{eq}}{\tau_{R,\lambda}} - \frac{f_\lambda - f_\lambda^{d}}{\tau_{N,\lambda}}. \tag{5.3}$$

For instance, the drift velocity $\vec{u}$ appearing on the displaced distribution function f_λ^d is obtained by imposing that the normal collisions conserve the momentum (Equation (2.15)), as in Section 2.2.2. Then, the drift velocity is

$$\vec{u} = \frac{d}{C_v T \left\langle \frac{1}{v_{p,\lambda}^2} \right\rangle} \int \hbar \vec{k}_\lambda \frac{f_\lambda}{\tau_{N,\lambda}} d\lambda. \tag{5.4}$$

From this equation, there is an important conclusion. Equation (5.4) shows that the drift velocity depends on the distribution function through its integration. This means that the drift velocity has different values depending on the ansatz for the distribution function f_λ. Actually, in the original work by Callaway [27], it is assumed that the distribution function is proportional to the temperature gradient $\vec{\nabla} T$, and then also the drift velocity is proportional to it. However, this is

not the general case.

Another important conclusion can be extracted from the collisions operator, which can be written as follows by substituting the expression for the displaced distribution function (Equation (2.13)) into Equation (5.3)

$$C(f_\lambda) = -\frac{f_\lambda - f_\lambda^{eq}}{\tau_\lambda} + \frac{T}{v_\lambda v_{p,\lambda} \tau_{N,\lambda}} \frac{\partial f_\lambda^{eq}}{\partial T} \vec{v}_\lambda \cdot \vec{u}. \tag{5.5}$$

Then, Callaway's collisions operator can be decomposed into an RTA-like collisions operator plus a second term that depends on the drift velocity. This means that when the RTA-like collisions operator part dominates, the results presented in Section 5.1 should be recovered.

Notice that so far, there is no assumption on the distribution function f_λ. Nevertheless, in this section, the ansatz for the distribution function considered is Equation (3.15), which depends on the heat flux and its first derivatives, and then, the corresponding drift velocity is (using Equation (5.4))

$$\vec{u} = \frac{1}{T}\left(A\vec{q} + B\frac{\partial \vec{q}}{\partial t}\right), \tag{5.6}$$

where it has been defined that

$$A \equiv \frac{1}{C_v \left\langle v_{p,\lambda}^2 \tau_{N,\lambda} \right\rangle} \int \hbar k \frac{\beta_\lambda}{\tau_{N,\lambda}} d\lambda, \tag{5.7a}$$

$$B \equiv \frac{1}{C_v \left\langle v_{p,\lambda}^2 \tau_{N,\lambda} \right\rangle} \int \hbar k \frac{\gamma_\lambda}{\tau_{N,\lambda}} d\lambda, \tag{5.7b}$$

being β_λ and γ_λ the weights appearing on the phonon distribution function (Equation (3.15)). Then, the displaced distribution function is

$$f_\lambda^d = f_\lambda^{eq} + \frac{A}{\omega_\lambda} \frac{\partial f_\lambda^{eq}}{\partial T} \vec{k} \cdot \vec{q} + \frac{B}{\omega_\lambda} \frac{\partial f_\lambda^{eq}}{\partial T} \vec{k} \cdot \frac{\partial \vec{q}}{\partial t}. \tag{5.8}$$

As already mentioned, the displaced distribution function depends on the ansatz for the distribution function. In the present case, the drift velocity depends on the heat flux and its temporal derivative. When considering a stationary situation with a uniform temperature gradient, Equation (5.6) recovers the typical result presented in [27], where the drift velocity is proportional to the temperature gradient.

Following the procedure in Section 3.3, all the transport

coefficients can be obtained. First, we recover the typical expression for Callaway's thermal conductivity (Equation (2.16)). As pointed out in Section 2.2.2, in kinetic materials, it is expected that the thermal conductivity of the RTA part is a good approximation. However, in collective materials, the perturbation due to Callaway's approximation is more relevant or even dominant. A similar analysis can be done for the other transport parameters, like the heat-flux relaxation time τ and the nonlocal length ℓ:

$$\tau = \frac{\left\langle \frac{\tau_\lambda}{\tau_{R,\lambda}\tau_{N,\lambda}} \right\rangle \left\langle \tau_\lambda^2 \right\rangle + 2 \left\langle \frac{\tau_\lambda}{\tau_{N,\lambda}} \right\rangle \left\langle \frac{\tau_\lambda^2}{\tau_{N,\lambda}} \right\rangle + \frac{\left\langle \frac{\tau_\lambda}{\tau_{N,\lambda}} \right\rangle^2 \left\langle \frac{\tau_\lambda^2}{\tau_{N,\lambda}^2} \right\rangle}{\left\langle \frac{\tau_\lambda}{\tau_{R,\lambda}\tau_{N,\lambda}} \right\rangle}}{\left\langle \frac{\tau_\lambda}{\tau_{R,\lambda}\tau_{N,\lambda}} \right\rangle \left\langle \tau_\lambda \right\rangle + \left\langle \frac{\tau_\lambda}{\tau_{N,\lambda}} \right\rangle^2}, \tag{5.9a}$$

$$\ell^2 = \frac{1}{d+2} v^2 \left(\left\langle \tau_\lambda^2 \right\rangle + \left\langle \frac{\tau_\lambda}{\tau_{N,\lambda}} \right\rangle \left\langle \frac{\tau_\lambda^2}{\tau_{N,\lambda}} \right\rangle \right), \tag{5.9b}$$

where, for the seek of simplicity, the presented expressions are under Debye's approximation and a single branch ($v_\lambda = v$ = constant), as also will be for the following expressions for τ_p and α. The general expressions for a general dispersion relation are presented in Appendix F. For both cases, the nonlocal length ℓ and the heat flux relaxation time τ have terms that differ from the RTA expressions. When materials with an important contribution of normal collisions are considered, these terms should become relevant. However, this only happens for very collective materials, like graphene. For other normal-dominated materials, like Diamond or BAs, these terms' contribution is negligible, as will be shown in Figures 5.3 and 5.4.

The expressions for the other parameters appearing on the GKE are

$$\tau_p = 0, \tag{5.10a}$$

$$\alpha = \frac{d-2}{d}. \tag{5.10b}$$

These two last expressions recover the expected results derived for a general collisions operator under Debye's approximation and a single branch (see Sections 3.3.3 and 3.3.4).

From a microscopic point of view, the distribution function in Callaway's approximation is described by the weights

$\vec{\beta}_\lambda$, $\vec{\gamma}_\lambda$ and $\overline{\overline{G}}_\lambda$ (see Equation (3.15))

$$\vec{\beta}_\lambda = \left(1 + A' \frac{1}{v_\lambda v_{p,\lambda}} \frac{1}{\tau_{N,\lambda}}\right) \frac{\tau_\lambda}{\kappa} \frac{\partial f_\lambda^{eq}}{\partial T} \vec{v}_\lambda, \tag{5.11a}$$

$$\begin{aligned}\vec{\gamma}_\lambda =& \frac{\tau_\lambda(\tau - \tau_\lambda)}{\kappa} \frac{\partial f_\lambda^{eq}}{\partial T} \vec{v}_\lambda \\ &+ \frac{1}{v_\lambda v_{p,\lambda}} \frac{1}{\tau_{N,\lambda}} \left(A' - \frac{B'}{\tau - \tau_\lambda}\right) \frac{\tau_\lambda(\tau - \tau_\lambda)}{\kappa} \frac{\partial f_\lambda^{eq}}{\partial T} \vec{v}_\lambda,\end{aligned} \tag{5.11b}$$

$$\overline{\overline{G}}_\lambda = -\left(1 + A' \frac{1}{v_\lambda v_{p,\lambda}} \frac{1}{\tau_{N,\lambda}}\right) \frac{\tau_\lambda^2}{\kappa} \frac{\partial f_\lambda^{eq}}{\partial T} \vec{v}_\lambda \vec{v}_\lambda + \frac{\tau_\lambda}{C_v} \frac{\partial f_\lambda^{eq}}{\partial T} \mathbb{1}, \tag{5.11c}$$

where it has been defined that

$$A' \equiv \frac{\left\langle \frac{v_\lambda}{v_p} \frac{\tau_\lambda}{\tau_N} \right\rangle}{\left\langle \frac{1}{v_p^2} \frac{\tau_\lambda}{\tau_R \tau_N} \right\rangle}, \tag{5.12a}$$

$$B' \equiv \frac{\left\langle \frac{v_\lambda}{v_p} \frac{\tau_\lambda^2}{\tau_N} \right\rangle + A' \left\langle \frac{1}{v_p^2} \frac{\tau_\lambda^2}{\tau_N^2} \right\rangle}{\left\langle \frac{1}{v_p^2} \frac{\tau_\lambda}{\tau_R \tau_N} \right\rangle}. \tag{5.12b}$$

Notice that all these weights are the RTA values obtained in Section 5.1 with a correction, which will be dominant when $\tau_{N,\lambda} \ll \tau_{R,\lambda}$. The results for the thermal conductivity are shown in Figure 2.3, where a difference between Callaway's approximation and RTA is observed for collective materials. For the case of the nonlocal length, the effect of Callaway's approximation is negligible except for graphene, as can be observed in Figure 5.3.

For the rest of the second-order or hydrodynamic parameters (heat flux relaxation time τ and α parameter), both models (RTA and Callaway) provide similar behavior, as can be seen in Figure 5.4.

A possible explanation for this negligible effect can be the following: the difference between RTA and Callaway's approximation is that the normal collisions relax to a function that conserves momentum (displaced distribution function), that, in general, is strongly related to the heat flux. The hydrodynamic parameters (nonlocal length, heat flux relaxation time, and α-parameter) are related to higher orders of the

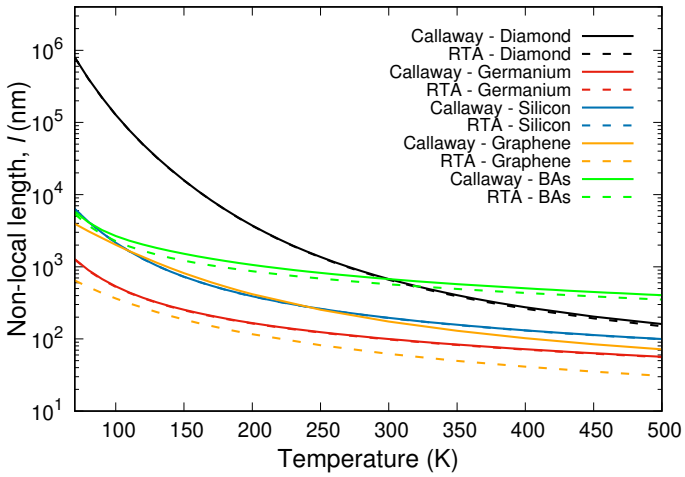

Figure 5.3: Nonlocal length in Callaway's model compared to the RTA for different materials (diamond, germanium, silicon, graphene, and BAs) ranging temperatures from 70 K to 500 K. Except for graphene, which is a collective material, the RTA does not differ from Callaway's approximation. The *ab initio* calculations are described in Appendix A.

distribution function ($\vec{\nabla}\vec{q}$ or $\partial_t \vec{q}$), and, for these cases, the relaxation time is equivalent to the RTA. This can be seen in Equation (5.5), where the first term is completely equivalent to the RTA, thus affecting flux derivatives terms in the distribution function. The second part of this equation only affects the distribution-function terms that can be projected to the crystal momentum, and thus it does not affect the terms of the heat-flux derivatives.

These are the results of Callaway's approximation, which gives a transition between the kinetic and collective regimes. As it is expected, the corresponding collective ($\tau_{N,\lambda} \ll \tau_{R,\lambda}$) and kinetic ($\tau_{N,\lambda} \gg \tau_{R,\lambda}$) limits recover the results of the RTA presented in Section 5.1 and the collective ones presented in Chapter 4, respectively.

Now, a comment on τ_p is in order. This parameter is shown in Figure 5.4. The results using Callaway or RTA are very similar for kinetic materials and τ_p is an order of magnitude smaller than the heat-flux relaxation time ($\tau_p \ll \tau$). Nevertheless, when we use Callaway's collisions operator for collective materials like BAs or graphene, τ_p^2 is negative ($\tau_p^2 < 0$) and of the order of the heat flux relaxation time (or even larger for the case of graphene), $|\tau_p^2| \sim \tau^2$. This is an unphysical result. As mentioned in Section 4.2.6, in the collective limit, this parameter is of the order of $\langle \tau_{N,\lambda} \rangle$, which has to be very small. This is not consistent with the results presented in this section.

A possible explanation for this inconsistency is the use of Callaway's collisions operator. As mentioned above, Callaway's and RTA results are very similar for the second-order parameters. This is also the case with τ_p^2. Since BAs and graphene are collective materials, one may assume that the

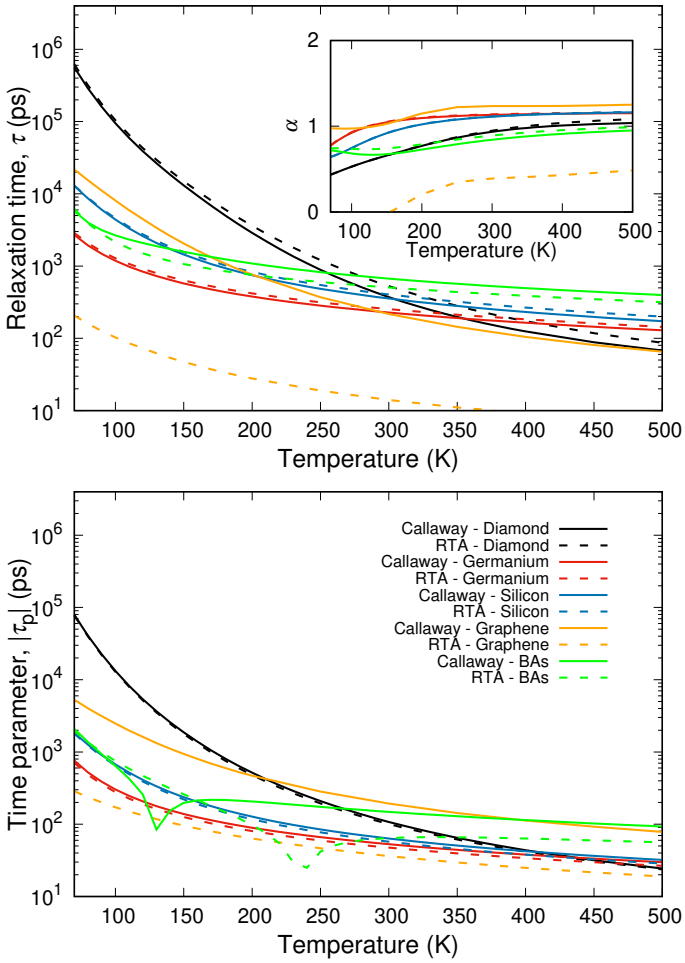

Figure 5.4: Heat flux relaxation time τ, τ_p, and the α parameter under Callaway's approximation compared to the RTA for different materials (diamond, germanium, silicon, graphene, and BAs) for a range of temperatures from 70 K to 500 K. As in the nonlocal length case (see Figure 5.3), except for graphene and BAs, which are collective materials, the RTA does not differ from Callaway's approximation. The *ab initio* calculations are described in Appendix A.

typical collisions operator for kinetic materials, the RTA, can lead to some problems and, thus, Callaway's approximation can lead to it. Furthermore, in the original work [27], Callaway presented the model as a phenomenological model. This may imply some incoherent results, as mentioned by Guyer and Krumhansl in [74], where it is said that Callaway's model is only valid in the limits (where $\tau_{R,\lambda} \ll \tau_{N,\lambda}$ or $\tau_{R,\lambda} \gg \tau_{N,\lambda}$), and the intermediate regimes (that is the case of graphene and BAs since RTA and Callaway's contributions are relevant) can lead to erroneous conclusions.

Finally, we can extract some conclusions. We have derived the GKE for kinetic materials using the RTA [70] and for intermediate regimes using Callaway's approximation. The results under RTA, with a nonlocal length of ~ 200 nm for silicon at room temperature, show that nonlocal effects are present in kinetic materials. This is at odds with other formalisms predicting negligible silicon viscous effects [43]. To check the validity of the results of the FDF, in the next chapter, we will compare the predictions of the GKE using

the *ab initio* with a wide range of experiments in silicon and germanium.

Moreover, we have provided an explicit expression for the phonon distribution function, which is the first time to our knowledge that a simple expression under unsteady inhomogeneous conditions in terms of first-principles quantities was obtained.

Experimental support of the FDF

6

In Chapter 3, the FDF is presented as a formalism that yields the GKE by assuming that the phonon distribution function depends on certain mesoscopic variables: the heat flux, and its first derivatives [70]. The present chapter aims to demonstrate the applicability of this equation with *ab initio* parameters through multiple experimental evidence. This evidence is presented in a wide range of situations, going from stationary to time-dependent situations, with different sizes or geometries, materials, and temperatures [14, 22, 23, 58, 64–67, 76, 128–130].

The experiments in this chapter and their modelization have been performed in collaboration with numerous research groups. In particular, the linear and circular heat source experiments (Section 6.1.2) were performed by Professor Shakouri's group at the Brick Nanotechnology Centre (University of Purdue). The heater grating experiments (Section 6.1.3) were performed by Professor Murnane's group at the University of Colorado at Boulder. The observation of second sound and the FDTR in germanium experiments (Sections 6.1.4 and 6.2.1) were performed by Reparaz's group at Institut de Ciència de Materials de Barcelona (ICMAB). The analytical solutions of the GKE of the FDTR experiment (Section 6.1.4) were performed by Professor Myers' group at Centre de Recerca Matemàtica (CRM). Finally, the modelization of all these experiments through the finite element method (FEM) was performed by Dr. Beardo from our group, which was the main contribution of his Ph.D. thesis [131].

My primary contribution in this chapter, which aims to

explain the numerous experiments where FDF predictions have been used, is to supply the *ab initio* values of the FDF and to participate in the modelization performed by Dr. Beardo.

The GKE, combined with the energy conservation and the corresponding boundary conditions, is implemented with COMSOL Multiphysics, a program that uses the FEM. This is done using the Galerkin method implementation [132] and its resulting weak form (see [62, 131] for further details). The easy implementation with the FEM is one of the main powers of the GKE since it extremely reduces the computational cost when simulating complex geometries, compared with the full BTE. Furthermore, the solution of the system provides temperature, heat flux, and its derivatives, which allows obtaining the phonon distribution function, using Equation (3.15), and thus solving the BTE from a microscopic point of view. Then, we will also analyze the presented experiments from that perspective.

The sections of this chapter present different experimental situations, all supporting the FDF. Section 6.1 presents experiments where the set-up's characteristic size or geometry is modified to observe the nonlocal effects (both in stationary and non-stationary situations). In Section 6.2, the effects of memory in non-stationary experiments are presented. In Section 6.3, an experiment of time-domain thermoreflectance (TDTR) is shown. Finally, Section 6.4 presents conclusions about comparing the FDF with experiments.

6.1 Nonlocal effects in silicon

As already mentioned, Fourier's law traditionally modeled heat transport in semiconductors, which does not predict any size effect. When large sizes are considered, above hundreds of microns [22, 23, 76], Fourier's law description is valid since the characteristic length of the heat carriers, the phonons, is smaller than this length. Fourier's law fails to predict the results when the length is reduced to sizes of the order of the MFPs of the phonons [11, 18, 58]. In general, to explain these phenomena, it is used an effective Fourier's law with a reduced thermal conductivity [13, 14, 16, 133] or a TBR that depends on the size [11, 18, 21]. In terms of effective thermal conductivity, the underlying assumption is to consider that phonons with a MFP larger than the system size do not contribute to heat transport. This assumption results in an

effective thermal conductivity where the effects start at the order of 10 microns for silicon at room temperature [22, 23, 76, 114] because the size of the larger MFPs of the phonons is reached. Then, this implies a multiscale effect since there is not a single size scale that characterizes the system.

However, as mentioned in previous chapters, the GKE predicts hydrodynamic effects. Usually, the most important effect of this model is the one predicted by the nonlocal length ℓ (see Equation (3.19b)), which implies single-scale effects compared with the previously mentioned multiscale effective thermal conductivity.

This nonlocal length, which is of the order of hundreds of nanometers (for silicon at room temperature is $\ell \approx 195$ nm [70]), is related to the correlation of the phonons in the region determined by this length. The fact that this length is the only size that characterizes the thermal description of the system, instead of the multiscale behavior, relies on the following physical assumption introduced in Chapter 3 [70].

The thermal description of the system depends on the physical situation. When the spatial flux variation is important enough, the distribution function must depend explicitly on it, i.e., the gradient of the heat flux $\vec{\nabla}\vec{q}$, resulting in Equation (3.15) ($\frac{\partial \vec{q}}{\partial t}$ is also included in the mentioned equation since the temporal derivative of the heat flux is also considered to be relevant, but in this section, we are focused on size effects). The higher-order perturbations of the distribution function (for instance, terms of the order of $\vec{\nabla}\vec{\nabla}\vec{q}$) are considered not to be excited because of the physical situation, or if they are excited, they are assumed to decay with time much shorter than the other excitations. This results in a distribution function that easily recovers the GKE, with a single spatial scale. These nonlocal effects are modeled with a Laplacian of the heat flux ($\nabla^2\vec{q}$), which can be considered a generalization of Fourier's law. This term reduces the heat flux near the boundaries and, consequently, effectively reduces the thermal conductivity.

The nonlocal effects are experimentally confirmed in different situations. In the present section, we observe the effects of reducing the characteristic sizes of the set-up, which are fully captured by the GKE. Section 6.1.1 reproduces the experimental thermal conductivity of silicon thin films for different sizes and temperatures. Furthermore, we present a microscopic description of the system according to FDF.

In Section 6.1.2, we perform a similar analysis as in the case of the thin film but consider linear and circular heaters. In Sections 6.1.3 and 6.1.4, the nonlocal effects of time-dependent experiments are studied. The first considers an initial pulse in a nanostructured transducer on top of a semiconductor. The second considers a FDTR experiment. In all these cases, except for the thin films, there are interfaces between the heaters (or an oxide layer in the FDTR experiment) and the semiconductor. Our boundary conditions will efficiently reproduce the contact with *ab initio* parameters. This contrasts with other formalisms, which use boundary resistance as a fitting parameter [11, 14, 16, 18, 21, 78].

6.1.1 Thin films

Thin films are one of the most paradigmatic and simpler situations where the size effects are observed in thermal transport. From a physical point of view, this setup is relevant because it can discern between a multiscale or single scale (like the GKE) behavior of heat. When a temperature gradient is imposed, the heat flow is different depending on the size of the film (when the characteristic sizes are reduced to the order of microns or nanometers [22–24, 128, 134, 135]). This effect can be seen in the measured effective thermal conductivity.

The GKE interpretation of this phenomenon is that the heat flux is reduced near the boundaries of the thin film. The boundary conditions obtained in the FDF (see Section 3.4 for details) predict a slip boundary condition for a free surface (Equation (3.46)) which imposes that the flux in the tangential-to-the-surface direction depends on its spatial variation in the normal direction. This condition implies that the heat flux resembles the Poiseuille velocity profile in fluids because of the viscosity, but the heat flux is not null at the boundary. This analogy is more accurate for normal-collision-dominating materials because phonon momentum is only destroyed at the boundaries since intrinsic collisions conserve it. Nevertheless, for materials where resistive collisions play an important role, this analogy can be understood as the momentum conservation within the region near the boundary because of the absence of resistive collisions.

Macroscopically, this effect is a consequence of the non-local length. The heat flux at the surface can not immediately relax in the heat flux inside the semiconductor, and it requires

a distance of the order of ℓ to transit between the one imposed in the boundary and the one inside the semiconductor.

In Figure 6.1, an example of the effects of this boundary in a thin film is depicted. As can be seen, Fourier's law predicts a plane flux profile, whereas the GKE reduces the heat flux near the surface in a region of the order of the nonlocal length ℓ. When a large thin film is considered ($w \gg \ell$, where w is the width of the thin film), the effects of the heat flux reduction in this region are negligible since this region is small compared with the width of the film, and the bulk thermal conductivity is recovered. Nevertheless, when we reduce the width of the thin film to the order of the nonlocal length, $w \sim \ell$, the heat flux reduction is comparable to the total heat flux, meaning that the effective thermal conductivity of the thin film is reduced.

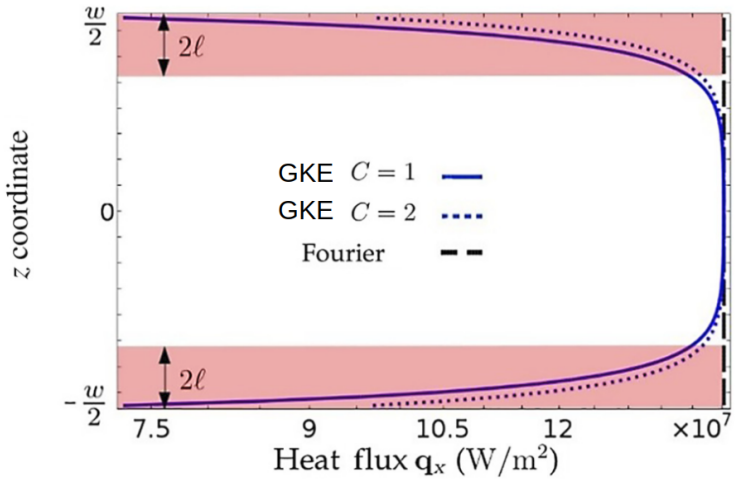

Figure 6.1: Heat flux profile of a thin film for a given width (in this case, a $w = 3\mu m$ silicon thin film at $T = 300K$). The black dashed line represents Fourier's law prediction, the solid blue line represents the GKE prediction with a completely diffusive boundary ($C = 1$), and the blue dotted line represents the GKE prediction with a non-completely diffusive boundary ($C = 2$). As it can be seen, the reduction of the heat flux near the boundaries occurs in a region of the order of the nonlocal length ℓ (indicated in red in the figure) in contrast to Fourier's law, where no reduction occurs. *Image extracted from [62].*

The GKE, the boundary effects, and their implications can be validated by comparing them to experimental results. We compare our prediction with experimental measurements [22, 23, 76] of the effective thermal conductivity for silicon thin films of different sizes and temperatures [62]. The results are presented in Figure 6.2: the GKE prediction is in good agreement with experimental measurements. At this point, it is important to remark that all the parameters appearing on the GKE are *ab initio* parameters, meaning that the model is completely predictive. This result also allows discerning between a single scale or a multiscale behavior since it can be explained with a single-scale equation, the GKE (a deeper explanation of this result is presented in Section 6.1.1.1).

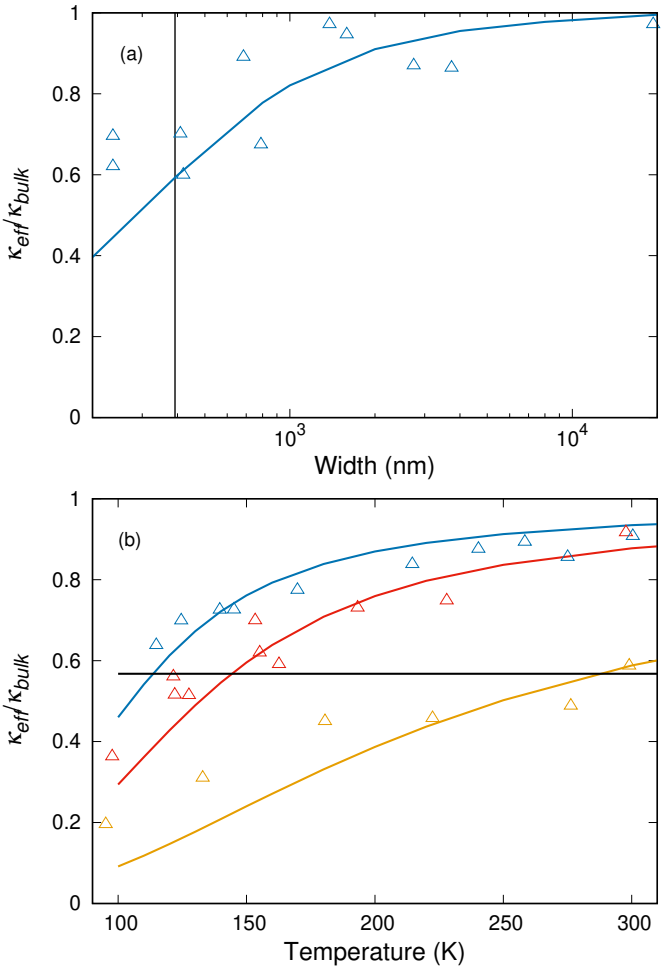

Figure 6.2: Normalized effective thermal conductivities for silicon thin films: (a) at 300 K and different sizes. The vertical line is at 2ℓ size, the limit of the applicability region; (b) at different temperatures for widths of 420 nm (blue), 1600 nm (red), and 3000 nm (blue). The horizontal line represents the normalized effective thermal conductivity for a film of $w = 2\ell$, where it is expected to fail the model. In both figures, (a) and (b), the solid line represents the GKE prediction, and triangles represent the experimental values. As can be seen, the prediction is good except for low temperatures or small sizes, where a discrepancy occurs. *Image reproduced from [62].*

Nevertheless, as can be seen in Figure 6.2, at certain (low) temperatures or (small) sizes, the prediction of the GKE differs from the experimental results. Thus, we propose an applicability region for the model, which is phenomenologically obtained by comparing the experimental values with the prediction [62]: the predictability of the GKE is guaranteed for a region going from an infinite film to a film of a width twice the nonlocal length ($w \approx 2\ell$). A reasonable explanation for this limit recalls that the region where the heat flux reduction occurs, which is of the order of 2ℓ (see Figure 6.1), overlaps with the other boundary. We attribute the model's failure at these scales to the microscopic derivation since it is valid only for moderate Knudsen numbers. This microscopic interpretation will be analyzed in Section 6.1.1.2. Higher-order moments or effective parameters in the physical description of the problem must be included to improve the predictability, as will be seen in Chapter 7.

Moreover, this description with a single characteristic length ℓ (the GKE description) allows describing another

kind of thin film: the holey thin film. We describe the thermal behavior of a thin film with holes of different diameters or periodicity [13] using exactly the same modelization parameters [62]. Notice the model's capability, combined with the Finite Elements implementation, to reproduce complex geometries with a single set of equations. Even in this more complex case, the comparison with the experimental results is in good agreement for a wide range of temperatures, as seen in Figure 6.3, where we compare two films with different periodicity, sizes, and diameters of the holes.

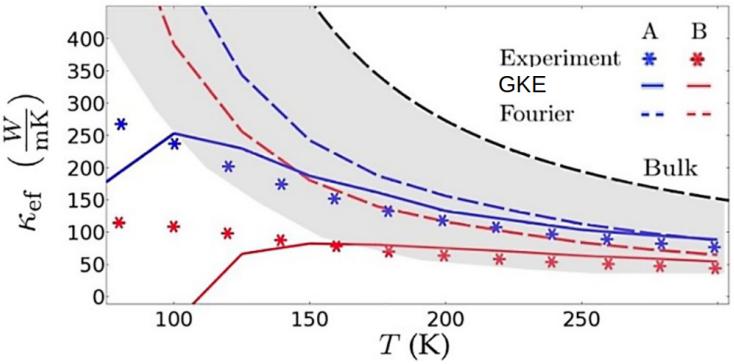

Figure 6.3: Effective thermal conductivities of silicon holey thin films. The A (B) film, in blue (red), represents a film of a width of $w = 4.84\mu m$ ($w = 4.49\mu m$), a periodicity of $20\mu m$ ($4\mu m$), and a hole diameter of $11.4\mu m$ ($2.8\mu m$). Asterisks: experimental values [13]; solid lines: GKE prediction; dashed lines: Fourier's law prediction. The gray zone is the predictability region, where the GKE reproduces the experimental results. *Image extracted from [62].*

6.1.1.1 Single scale vs. multiscale results

As previously mentioned, some theoretical efforts have been made to predict the effective thermal conductivity for the nanoscale using a multiscale model. This means that thermal transport has multiple characteristic lengths, usually related to the MFPs of phonons. A paradigmatic example of this situation is the RTA applied to the thin films. An exact solution is obtained when considering an infinite thin film using the RTA in the BTE [31]. As expected, phonons of MFP larger than or similar to the width of the films have a suppressed contribution to the effective thermal conductivity. Then, the suppression of the thermal conductivity spans several orders of magnitude because of the MFPs of the phonons.

In contrast, the GKE predicts a single scale effect, since the only characteristic length is the nonlocal length ℓ. For example, for thin films, the next equation is obtained [136],

$$\frac{\kappa_{eff}}{\kappa} = 1 - 2\text{Kn}\frac{\tanh\left(\frac{1}{2\text{Kn}}\right)}{1 + C\tanh\left(\frac{1}{2\text{Kn}}\right)}, \tag{6.1}$$

where the Knudsen number has been defined as $\mathrm{Kn} = \frac{\ell}{w}$, and C is the parameter appearing on the slip boundary condition, that it is $C = 1$ for diffusive boundaries. Equation (6.1) shows that the reduction in the effective thermal conductivity predicted by the GKE is only associated with the ℓ.

This difference in the effective thermal conductivity prediction allows us to experimentally discern between the multiscale and the single-scale thermal transport behavior in thin films. For the RTA prediction, the reduction of the effective thermal conductivity can be seen as the width of the film reduced to several microns since there are MFPs of these sizes (for the silicon example at room temperature, see Figure 2.4). However, the GKE predicts size effects when the width reaches the order of the nonlocal length, which in silicon at room temperature is ~ 200 nm [70].

Figure 6.4 shows the experimental results for silicon thin films of different sizes and temperatures [22] and they are compared to the GKE and RTA solutions. As already mentioned, we expect that the GKE fails to predict Knudsens numbers above $\mathrm{Kn} > \frac{1}{2}$. Then, in this figure, we have used transparent experimental points depending on the Knudsen to remark the points we expect to be predictive. In the predictability region, the GKE captures more accurately size effects in front of the RTA model. This suggests that thermal transport in thin films has a single scale.

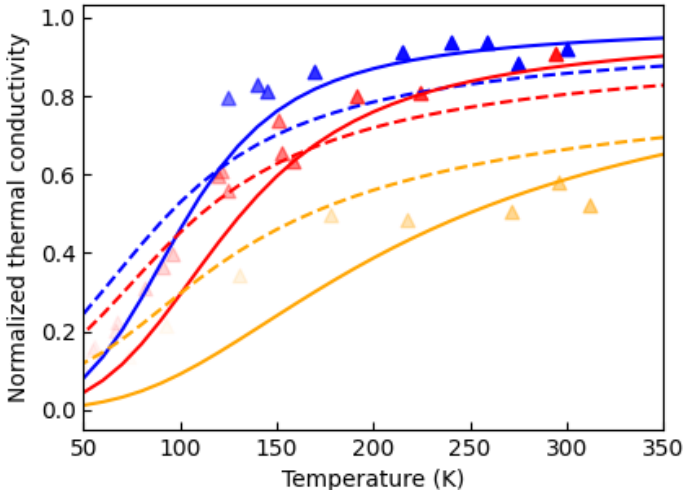

Figure 6.4: Effective thermal conductivities for thin films compared with the GKE (single scale) and the RTA (multiscale) predictions. Triangles represent the experimental results (with its transparency depending on the Knudsen number), the solid lines represent the GKE prediction, and the dashed line represents the RTA prediction. In blue, the results for a thin film of 3000 nm, in red of 1600 nm, and in orange of 420 nm.

6.1.1.2 Microscopic interpretation

To conclude the section, we will analyze the experiment from a microscopic point of view. One of the strengths of the FDF

is that it provides both the mesoscopic description (transport equations) and the microscopic description (phonon distribution function). Because of its simplicity, the thin film's case allows for obtaining analytical solutions from the GKE for the heat flux profile and effective thermal conductivity [136]. The expression for the effective thermal conductivity was already shown in Equation 6.1. However, we are now interested in the heat flux because it is the magnitude appearing on the phonon distribution function (Equation 3.15), which is the magnitude we will study in this section. The expression for the heat flux is [136]

$$q_x = \kappa \frac{\Delta T}{L}\left(1 - \frac{\cosh\left(\frac{y}{\ell}\right)}{A(\mathrm{Kn})}\right), \tag{6.2}$$

where we have assumed that the direction perpendicular to the thin film surfaces is the y-direction, and the direction of the $\vec{\nabla}T$ is the x-direction. Thus, the only component of heat flux is also in the x-direction. We have also used that the gradient of temperature is constant along all the film, $\frac{\partial T}{\partial x} = -\frac{\Delta T}{L}$, with L the length of the film and ΔT the temperature difference between the extremes. Finally, we have used that $\mathrm{Kn} = \frac{\ell}{w}$, and we have defined that

$$A(\mathrm{Kn}) \equiv \left(1 + C\tanh\left(\frac{1}{2\mathrm{Kn}}\right)\right)\cosh\left(\frac{1}{2\mathrm{Kn}}\right), \tag{6.3}$$

where C is the parameter appearing on the slip boundary condition (Equation 3.46).

Considering a time-independent situation, the phonon distribution function for the GKE case is (Equation 3.15)

$$f_\lambda = f_\lambda^{eq} + \beta_{\lambda,x} q_x + g_{1,\lambda} \frac{v_{\lambda,x} v_{\lambda,y}}{v_\lambda^2} \frac{\partial q_x}{\partial y}. \tag{6.4}$$

In this expression for the distribution function, we know β_λ, $g_{1,\lambda}$, obtained through the FDF (see Chapter 3) and the heat flux profile (and thus its derivative), which is obtained from Equation (6.2). Then, we can obtain the exact value for the phonon distribution function.

Nevertheless, we can interpret the phonon distribution function in a more intuitive form: as an effective Fourier's law. As we have shown in Section 3.2, we should consider that the phonon distribution function is $f_\lambda = f_\lambda^{eq} - \kappa \vec{\beta}_\lambda \cdot \vec{\nabla}T$ to obtain Fourier's law. To recover Equation (6.4), we will

consider the same distribution function to obtain Fourier's law but with a modification:

$$f_\lambda = f_\lambda^{eq} + s_\lambda \kappa \beta_{\lambda,x} \frac{\Delta T}{L}, \tag{6.5}$$

where s_λ is a new unknown function that aims to capture the non-Fourier effects predicted by the GKE, resulting in an effective Fourier's law with exactly the same behavior as the GKE. To do so, we equal Equations (6.4) and (6.5), and we obtain

$$s_\lambda = 1 - \frac{\cosh\left(\frac{y/w}{\mathrm{Kn}}\right)}{A(\mathrm{Kn})} + \frac{\Lambda_{\lambda,y}}{\ell} \frac{\sinh\left(\frac{y/w}{\mathrm{Kn}}\right)}{A(\mathrm{Kn})}, \tag{6.6}$$

where, for the seek of simplicity, we have used the RTA values for β_λ and $g_{1,\lambda}$ (see Section 5.1). We have also defined the MFP in the y-direction as $\Lambda_{\lambda,y} \equiv v_{\lambda,y}\tau_\lambda$.

Notice that s_λ resembles the suppression function used to describe some experiments, where the contribution of some modes to the thermal conductivity is suppressed [13, 14, 18, 51, 79, 80]. However, the behavior of s_λ is substantially different:

- It depends on the position of the thin film y. This excludes formalisms where the suppression function does not depend on the position.
- It is not necessary that $0 \leq s_\lambda \leq 1$. One can obtain very large or negative values when considering modes with a large $\Lambda_{\lambda,y}$. Notice that negative values for s_λ are not nonphysical since the phonon distribution function may still be positive because of the equilibrium term f_λ^{eq}.
- When obtaining the effective thermal conductivity by integrating Equation (6.5) over all the phonon modes, it does not depend on the phonon mode, even s_λ does. This is because the dependence in the mode vanishes by symmetry in an isotropic material. This result, which may seem surprising, is intuitive since the s_λ is derived to recover the GKE behavior, which has no mode-dependence.

The conclusion is that, when we try to interpret thermal transport in thin films with an effective Fourier's law, we require a complex dependence in the distribution function with position-dependent weights to interpret the experimental results. Besides, FDF, which naturally includes the first

derivatives, provides a simple interpretation of the phonon distribution function.

At this point, we would like to remark that the microscopic interpretation carried on in this section is not limited to the case of thin film. When we consider other experiments, the FEM implementation of the GKE allows obtaining the values of the macroscopic magnitudes (temperature, heat flux, and its first derivatives) for all the positions and times of the experiment. Thus, we can also obtain the distribution function for arbitrary complex situations.

6.1.2 Linear and circular heat sources

In collaboration with Brick Nanotechnology Centre (University of Purdue)

In the previous section, we studied the effects of reducing the size of a silicon sample with the GKE, specifically for a thin film. In that case, the only material to be simulated is the semiconductor and its geometry, but no interactions between materials are necessary. Nevertheless, there are some situations where it is necessary to introduce different materials and, consequently, interfaces between them. This is the case of metallic heat sources with semiconductor substrates, which is the situation presented in this section: we will show the thermal process of releasing heat from a metallic structure to a silicon substrate. The particularity of this experiment is that two different geometries (linear and circular heaters) with different sizes and temperatures are compared [64, 67]. Thus, it allows to check the model by changing the temperature, the size, or the geometry, giving a powerful tool to validate the prediction of the FDF. Once again, it explicitly gives non-Fourier signatures of thermal behavior.

The experiments are performed through the thermoreflectance imaging (TRI) technique. This novel technique is based on the change of the incident light's reflection coefficient due to the material's local temperature, resulting in a high-resolution, non-contact optical imaging technique [58, 137]. In Figure 6.5 we show an example of the output of the TRI for two samples of the experiment. There, the high resolution of the technique is appreciated.

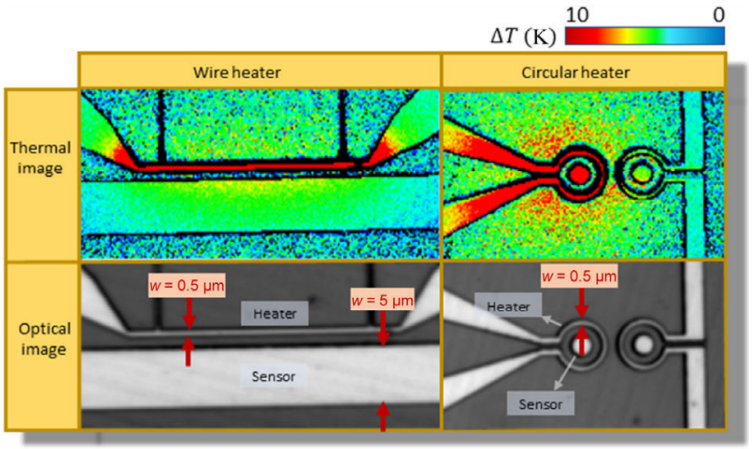

Figure 6.5: Example of the output information of TRI technique. At the bottom, the optical images of the setup (a circular and linear heater of Au with a sensor of a 500 nm width on top of a silicon substrate) with its corresponding thermal images. At the top, images are extracted with the TRI technique [64, 67]. Notice the high-resolution of the TRI. *Image extracted from [64].*

6.1.2.1 Fourier's law's failure

In this experiment, the non-Fourier signature is manifested explicitly, as observed in the experiment of [58] with the same geometry, but considering InGaAs besides silicon. With TRI, temperature profiles are easily obtained and, thus, compared with the corresponding model prediction. To demonstrate the failure of Fourier's law in this setup, we plot a comparison of Fourier's results and the experimental ones (Figure 6.6).

As mentioned in Chapter 2, an effective (reduced) thermal conductivity is usually used to explain some results in the thermal transport field. In that sense, in Figures 6.6.a-b, we present an example of the temperature profile of a circular and a linear Au heater on top of silicon using different values of the thermal conductivity: using the bulk value, using an effective thermal conductivity trying to fit the semiconductor or using a thermal conductivity fitting the metal [64]. In Figures 6.6.a-b, we can observe that Fourier's law can not predict the full temperature profile even using fitting parameters. When the semiconductor is fitted, the metal can not be predicted, and the other way around. Furthermore, the behavior of the fitted thermal conductivity when the size of the heater is reduced depends on the geometry. For a linear heater (see Figure 6.5 for the geometry), when the size of the heater is decreased, the thermal conductivity to fit the heater is increased, and the thermal conductivity to fit the sensor is decreased. On the contrary, for a circular heater, when the size of the heater is decreased, both the thermal conductivity to fit the heater and the sensor decrease (see Figure 6.6.c). This is a paradigmatic situation to show that the non-Fourier behavior not only depends on the size but also on the system's geometry.

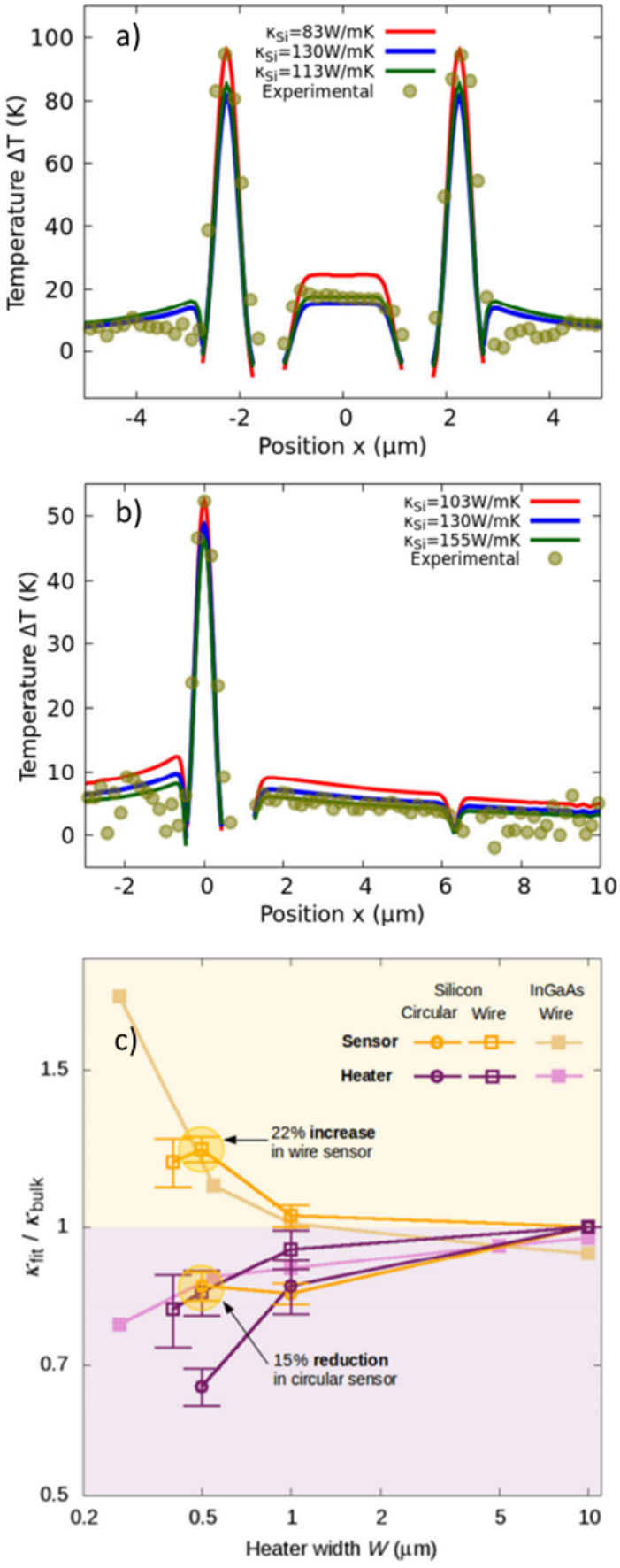

Figure 6.6: Temperature profile of an Au heater of a width of 0.5 μm and a silicon substrate. The green dots represent the experimental values, the blue line represents the prediction with the bulk thermal conductivity, the red line represents Fourier's prediction with a thermal conductivity fitted to reproduce the heater, and the green line represents the prediction trying to fit the substrate. The a) figure represents the circular geometry, and the b) figure represents the straight geometry (see Figure 6.5 to clarify the geometries). In both cases, Fourier's law can not predict the full temperature profile. c) Normalized fitted thermal conductivity for heaters of different sizes (for silicon [64] and InGaAs [58]). The fitted thermal conductivity depends not only on the size but also on the system's geometry. *Image extracted from [64].*

6.1.2.2 GKE prediction

This failure of Fourier's law can be explained the absence of hydrodynamic effects, which are predicted by the GKE with *ab initio* parameters. Furthermore, the complexity of the geometry (circular and linear heaters) makes the analytical solution of the BTE difficult to obtain. With the GKE, and using FEM, we can obtain the solution for this situation (see [64] for further details of the thermal behavior of this experiment).

Naturally introduced by the GKE, this geometry and size dependence allows predicting a wide range of situations. The problem with effective Fourier's law reported in Section 6.1.2.1 is solved through the nonlocal effects. The prediction of the GKE reproduces the temperature profile obtained with the TRI technique [64]. Thus, it predicts the heater and the sensor with a single set of parameters, solving the Fourier's law problem presented in Figure 6.6.c. All these predictions are shown in Figure 6.7. In this figure, Fourier's law and the GKE predictions converge when large sizes are considered for both the linear and the circular heater; and they coincide with the experimental values. This is because nonlocal effects are negligible for large sizes, and then the GKE recovers Fourier's law. Nevertheless, Fourier's law underpredicts the temperature profile when size is decreased, while GKE recovers the experimental values.

It is worth to remark the next point: with the GKE, we reproduce the temperature map of the whole experimental sample. In the case of the thin film [62] (Section 6.1.1), the only experimental output is the effective thermal conductivity, which implies that it can be fitted with numerous methods since there is a single experimental output. Furthermore, the heat flux profile predicted for thin films by the GKE has no experimental evidence. In the present section, the output values of the experiment are the entire map of temperatures, which has much more robustness in the model validation.

This set of experiments has a particularity with respect to the thin film experiments (Section 6.1.1): an interface exists between two materials: the heater and the substrate. In Section 3.4, we derived a boundary condition for the normal-to-the-boundary heat flux using the FDF. The derivation [63] recovers the DMM when there are no nonlocal effects (nevertheless, when the nonlocal effects are relevant, other terms besides the predicted by the DMM appear). This term, implemented into the boundary conditions, is calculated

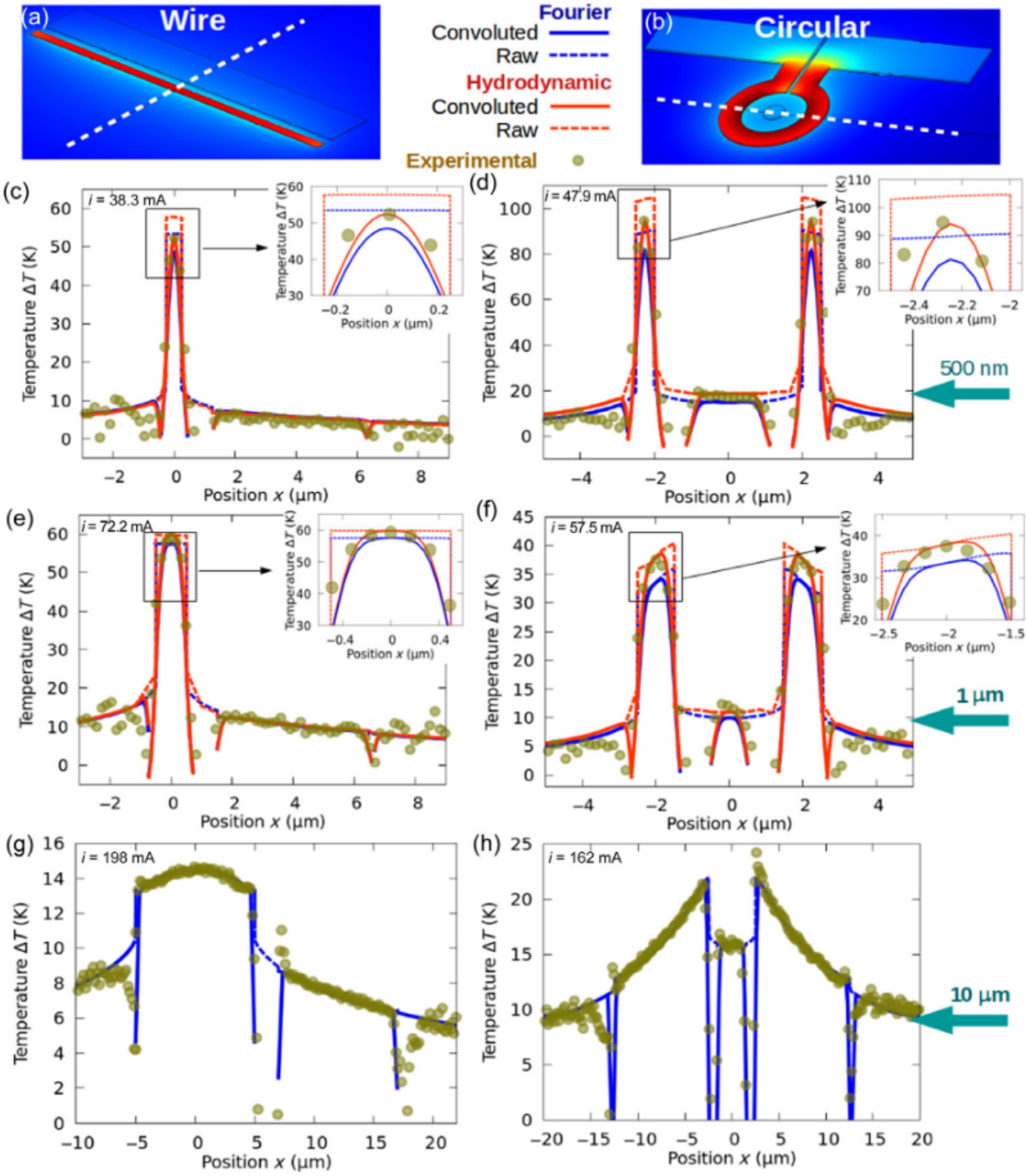

Figure 6.7: Predicted and experimental results for linear and circular heaters for Fourier's law and GKE. a) and b) are the thermal images for the wire and circular geometries, respectively. The left column, c), e), and g), represents the temperature profile of a linear heater for different sizes. The right column, d), f), and h), represent a circular heater. There is the Fourier's law prediction in blue, and the GKE one in red. The raw (dashed) line represents the real predicted temperature profile. Nevertheless, thermal images must be compared with the convoluted (solid) line, where a convolution because of the optical blurring is done (see [64] for more information). As can be seen, the prediction of the GKE can reproduce the experimental values for both geometries and all the sizes. *Image extracted from [64].*

from *ab initio* and is size or geometry-independent. Nevertheless, since the DMM predicts a perfect contact, it does not consider the interface's experimental defects.

We use a value for the boundary resistance proportional to the DMM result to capture these defects. We fit the value at large scales to obtain the proportionality constant, where Fourier's law is predictive. Thus we do not incorporate size effects in the boundary resistance. The results obtained are close to the DMM. When we reduce the size of the heater, we do not change this value. Then, we guarantee that the boundary resistance is not a fitted value. This contrasts with other approaches where size-dependent fitting parameters are used to predict the interface [138].

So far, we have obtained the results presented at room temperature [64]. Nevertheless, FDF also predicts the transport parameters depending on temperature, as seen in Chapter 3. Using the same samples as in the room temperature case, we present the results in a range of temperatures going from 100 K to room temperature [67]. Again, the predicted results of the GKE, using completely *ab initio* parameters, reproduce the experimental measurements done by TRI.

Then, combining all the results in circular and linear heaters allows concluding that the GKE predicts the geometry and size effects for complex geometries and a wide range of sizes without fitting parameters. Even more, it can be predictable for a wide range of temperatures. An image of this conclusion is depicted in Figure 6.8, where a transition in size, geometry, and temperature is represented.

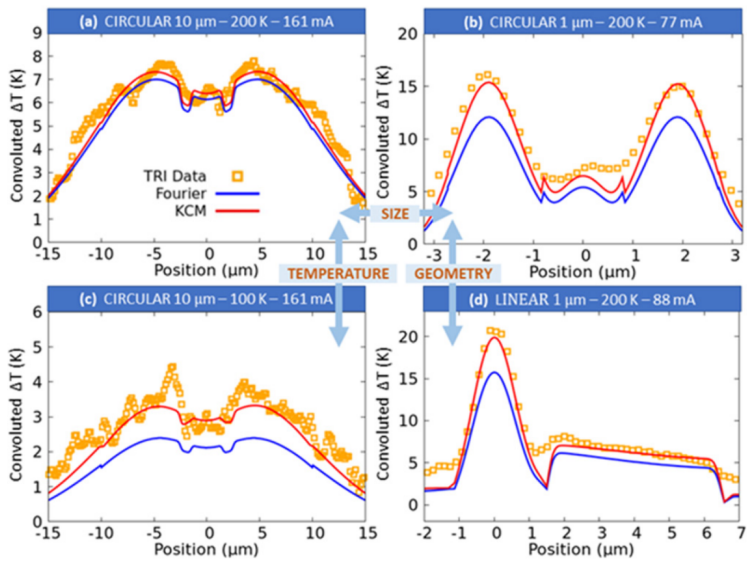

Figure 6.8: Representation of the prediction power of the FDF parameters for the GKE. The GKE (red line) reproduces the experimental values of TRI (orange squares), where Fourier's law fails (blue line). This can be seen for: the same geometry and different sizes, a) and b) figures; for the same size and different temperatures, a) and c); and for the same size and different geometries, b) and d) figures. At the top of each image is shown the geometry (circular or linear), the size, the temperature, and the electrical current intensity in the heater. *Image extracted from [67].*

Nevertheless, in this experiment, when we consider the

smaller circular heater at 100 K, we fail to predict the temperature profile at points of the semiconductor close to the heater. We attribute this limitation to the microscopic description of the experiment. The phonon distribution function for some modes at these points is negative, which has no physical sense. This is because of the large gradients of the heat flux and its effects on f_λ (Equation (3.15)). This limitation is associated with the derivation through the FDF, which is bounded to moderate Knudsen numbers.

In Chapter 7, we will microscopically analyze this behavior to argue the limitation of the model for this extreme situation.

6.1.3 Heater gratings

In collaboration with Kapteyn-Murnane group (University of Colorado)

This section presents another situation where nonlocal effects and the GKE can explain the experimental results. Nevertheless, in this case, the GKE is applied to describe a time-dependent situation in contrast to previous sections of this chapter.

The experimental setup consists of periodic 1D- and 2D-confined heat sources on top of the silicon substrate. The experiment studies the heat dissipation from the heaters to the semiconductor using extreme ultraviolet (EUV) scatterometry [11, 18, 21]. As explained in Figure 6.9, an infrared laser is used to pump the metallic structures, and an ultrashort EUV probe pulse is used to measure the change in the diffraction efficiency.

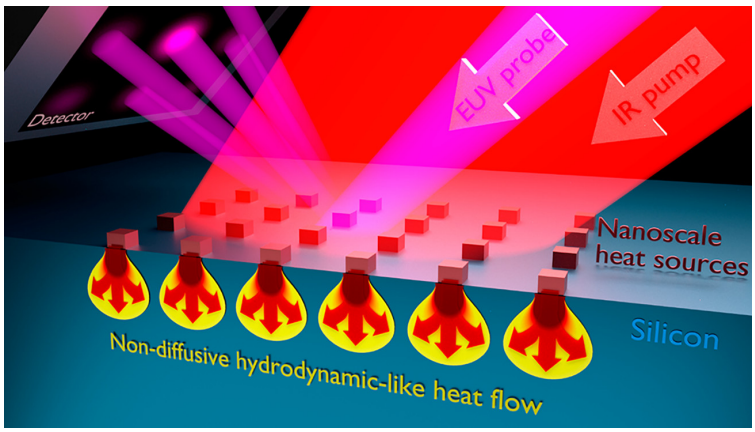

Figure 6.9: Scheme of the experimental setup of the EUV scatterometry in confined 1D and 2D nanostructures. An infrared laser pulse heats the metallic structures, and an EUV probe measures the diffraction efficiency of the system. Heat is dissipated into the silicon substrate. In the silicon region near the heaters, it is expected hydrodynamic behavior. *Image extracted from [65].*

The periodic structures are arranged in periodic nanolines (or nanodots) with different periodicity (P) between

lines (dots) and different line (dot) sizes (L). Using finite elements, we can implement the GKE in a time-dependent situation to simulate this experiment, with the parameters extracted from the FDF. The interface condition for simulating the TBR and the slip-boundary condition are used in this situation. Moreover, we couple the thermal system with an elastic set of equations to simulate the whole system. In this studied case, the elastic part plays an important role since the heat pulse dilates the system. This is one of the main advantages of implementing the GKE using finite elements: it can be easily coupled with other physical models.

Depending on the periodicity and the size of the nanoline or the nanodot, it is useful to distinguish between the effectively isolated and the close-packed situations. The first one refers to the situation where the hydrodynamic effects that take in the semiconductor due to one heater are not affected by the hydrodynamic effects of the other heater. Since the characteristic size of the hydrodynamic effects is the nonlocal length ℓ, this situation is when the distance between the heater is larger than twice the nonlocal length ($P - L > 2\ell$). This condition for the isolation of the heaters is strongly related to the predictability region presented in Section 6.1.1, where the distance between the two boundaries of the thin film, W, is required to be twice the nonlocal length ($W > 2\ell$). In Figures 6.10.a-b, we present the results in this situation for nanolines and nanodots, respectively. This figure distinguishes between the inertial and quasi-static results. The quasi-static solutions capture the deformation of the system because of the thermal expansion; hence, they can be associated with the local temperature [21]. The inertial solution takes into account the contribution of the oscillating elastic waves. This last solution is the one used to compare with the experimental results of the diffraction efficiency.

In the effectively isolated situation, both for nanolines and nanodots, the predicted result with the GKE is excellent, as seen in Figure 6.10. We obtain this with *ab initio* parameters, without any geometry-dependent fit parameter [65]. This contrasts with, for example, suppression-function models, which are very difficult to implement for the nanodots' geometry [16].

For the close-packed case ($P - L < 2\ell$), the nonlocal effects of two consecutive heaters are expected to interact since the phonons from one heater can reach the other heater's phonon before scattering (remember that the nonlocal length

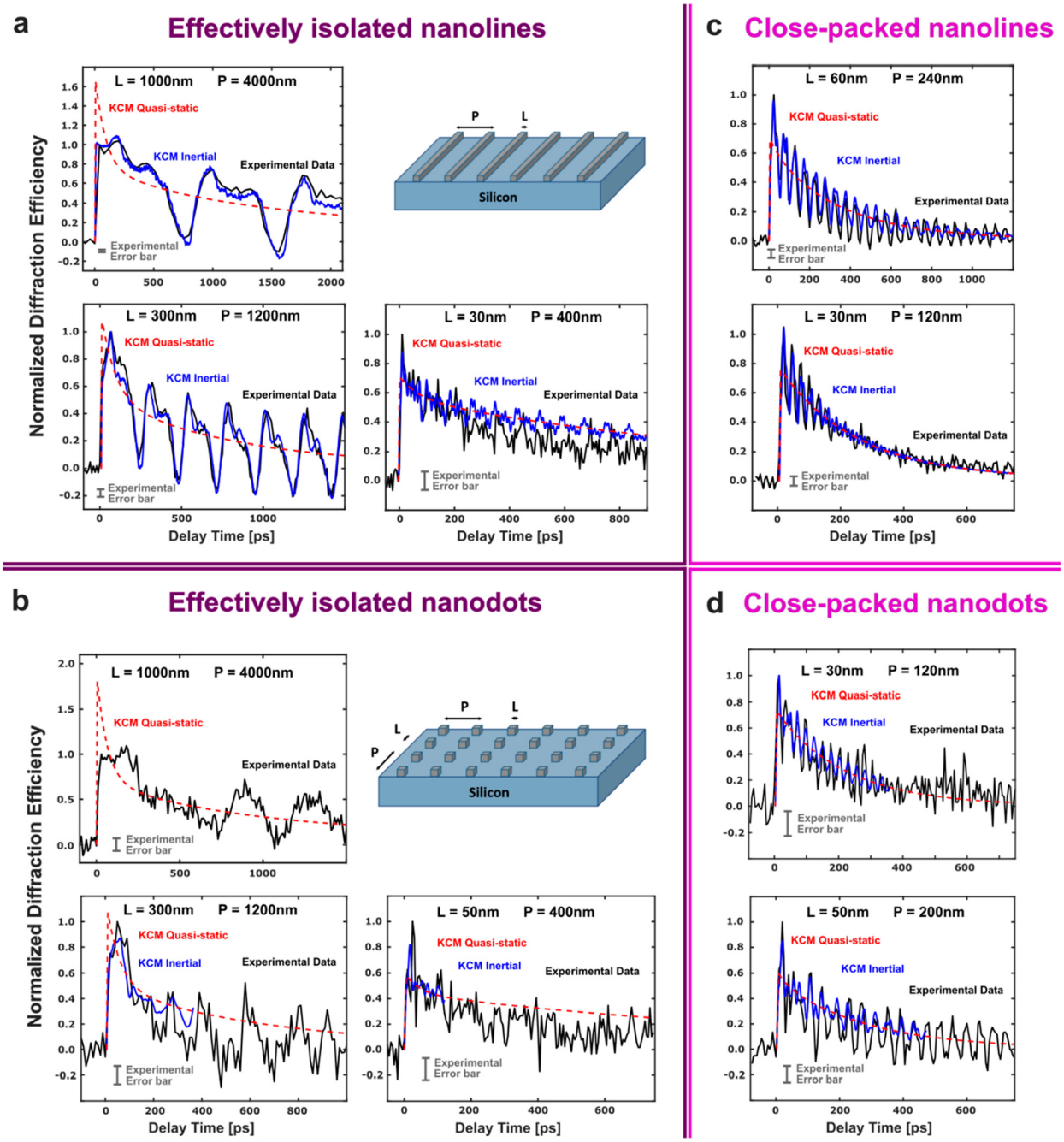

Figure 6.10: Comparison between the EUV scatterometry data and the GKE prediction for the 1D and 2D-nanostructures. Black lines represent the experimental data, the blue line is the GKE prediction, and the red dashed line is the GKE prediction taking into account only the system's thermal (not elastic) deformation. a) and b) figures represent the effectively isolated situations ($P - L > 2\ell$ for lines and dots, respectively, for different P and L combinations. c) and d) figures represent the close-packed case ($P - L < 2\ell$), where an effective nonlocal length is used ($\ell = \frac{P-L}{2}$). In all the situations, the GKE prediction is in excellent agreement with the experimental data. *Image extracted from [65].*

is related to the characteristic size of the phonons). In this situation, since the GKE is derived for finite Knudsen numbers, the model is reasonable to fail, accordingly to the predictability region [62]. We propose an effective model to overcome this limitation, keeping the simplicity of the GKE. In this case, we assume that the effective nonlocal length is $\ell = \frac{P-L}{2}$, i.e., a geometry-dependent parameter that is half of the distance between heaters [65]. As seen in Figures 6.10.c-d, the agreement with the experimental results for the close-packed situation using this nonlocal length is excellent.

Nevertheless, we would like to point out that when effective parameters are used, the model has reached the limit of applicability. These situations will be discussed in Chapter 7, where some solutions for these limits will be presented.

6.1.3.1 Two-time scales: the two-box model

In this section, we analyze this experiment's thermal decay and compare it with the prediction of the GKE and Fourier's law. Figure 6.11.a shows the thermal decay for an isolated 250 nm line width case. Fourier's law can only predict a single timescale, and it results that, even in the best fit, it cannot reproduce the thermal decay at all times: it overestimates the thermal decay at short times and underestimates it at large times. However, the experimental results display two different time scales: a fast one at short times and a slow one at longer times. Moreover, this behavior is observed in other nanostructure sizes (see Figure 6.10), clearly concluding that Fourier's law cannot capture the full nanostructure relaxation and, consequently, misses the underlying physics.

Contrarily, the GKE does predict these two-time scales. The processes involved in this prediction are interface decay and hydrodynamic decay. The first one is the process where the heater releases the energy rapidly into the dam region, which is defined as the region of the semiconductor of size L below the heater. It plays the role of a reservoir due to the thermal viscosity from hydrodynamic effects. Then, with a much larger timescale, the heat is released from the dam region to the rest of the semiconductor. These two processes are schematically represented in Figure 6.11.b, which we named the two-box model [65]. This model is a consequence of the GKE, and, at short times, it predicts the temperature

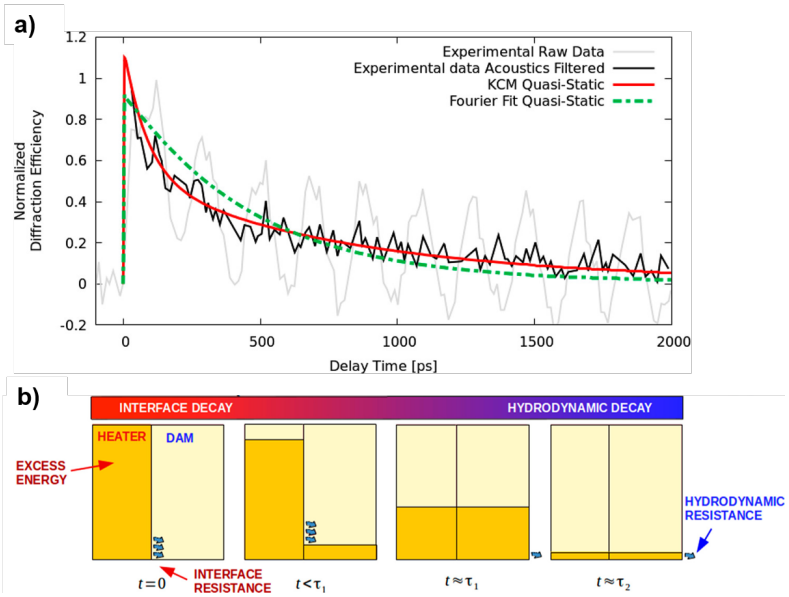

Figure 6.11: a) Experimental and theoretical quasi-static change in diffraction efficiency in terms of time. The results are for an isolated heater of $L = 250$ nm and $P = 1000$ nm. The gray line represents the experimental data, the black line represents the experimental data taking into account only the thermal processes, the red line represents the GKE prediction, and the dashed green line represents the best fit of Fourier's law. There are two experimental timescales, which can be reproduced by the GKE. b) Cartoon of the two-box model in analogy with fluids. The two boxes represent the heater and the dam region, with the liquid as the temperature. *Image extracted from [65].*

of the heater

$$T_1 - T_2^{\infty} = a_1 e^{-\frac{t}{\tau_1}} + a_2 e^{-\frac{t}{\tau_2}}, \tag{6.7}$$

where T_1 is the heater temperature, T_2^{∞} is the average substrate temperature at an infinity separated from the heater point, and a_1, a_2, τ_1 and τ_2 are parameters that depend on the length and height of the heater and the rest of the parameters involving the transport equations of the heater and the semiconductor (we provide their analytical expressions and their corresponding derivation at [65]). Equation (6.7) present two-time scales, as expected from the results of Figure 6.11.a.

From a microscopic perspective, the two-box model can be interpreted as follows. Just below the heater, in the so-called dam region, the flux is perpendicular to the surface and constant throughout it. This implies that there are no flux derivatives. For that case, the term $\overline{\overline{G}}_\lambda : \vec{\nabla}\vec{q}$ of the phonon distribution function (Equation (3.15)) is negligible, and f_λ results in $f_\lambda \approx f_\lambda^{eq} + \vec{\beta}_\lambda \cdot \vec{q}$. This last shape of the distribution, as seen in Section 3.2, is the one that recovers Fourier's law. This means that, from the heater to the dam region, the heat is rapidly evacuated as Fourier and is limited by the TBR.

When we consider a point far from the heater, for instance, the limiting region of the dam region, the heat flux starts to curve. At this point, $\overline{\overline{G}}_\lambda : \vec{\nabla}\vec{q}$ is not negligible, and we

recover a GKE behavior instead of Fourier's one observed just below the heater. Then, hydrodynamic effects are dominant, and evacuation is much slower, consistent with the two-box model.

6.1.4 Frequency domain thermoreflectance

In collaboration with Centre de Recerca Matemàtica (CRM) and Institut de Ciència de Materials de Barcelona (ICMAB)

In the present section, we analyze the experiment of FDTR [14] with FDF. This FDTR experiment consists of an oscillating laser that heats a thin metal film on top of a substrate, and the temperature evolution of the metal is obtained through the FDTR techniques [10, 14, 15, 129, 139–141]. The results of these experiments, which predict a non-Fourier behavior, are typically interpreted as a reduction of the thermal conductivity in Fourier's law related to the suppression of phonons with a large MFP [14, 129]. Nevertheless, this interpretation leads to non-physical results, as we will show in this section [63], and we will demonstrate that the non-Fourier behavior is related to phonon hydrodynamics since the GKE can predict the experimental results.

In the FDTR experiments, the interface boundary resistance (the TBR) between the metal and the substrate (see Section 3.4.1) plays a very important role. The DMM is a typical approach to modeling the interface, which provides an orienting upper bound. In [14], a TBR with significantly smaller conductance than the expected at room temperature is used ($210 MW/m^2K$ in front of $723 MW/m^2K$ of the DMM). Figure 6.12 shows the effective Fourier's law predictions in the substrate with this TBR. The experiment outputs two observables: the phase shift φ and the oscillation amplitude ΔT. Even with this fitted TBR, if we fit with an effective thermal conductivity the experiment's phase shift, the amplitude of oscillation predictions are significantly worse, and the other way around, as seen in Figure 6.12. This implies that, with an effective Fourier's law, one can not predict the physics of the FDTR experiment even if we use effective parameters.

In the present time-dependent situation, the GKE predicts a non-Fourier behavior because of the nonlocal effects. One may think that the memory effects $\tau \frac{\partial \vec{q}}{\partial t}$ should play an important role in a FDTR experiment. However, the influence of the TBR and the mentioned nonlocal effects eclipse them

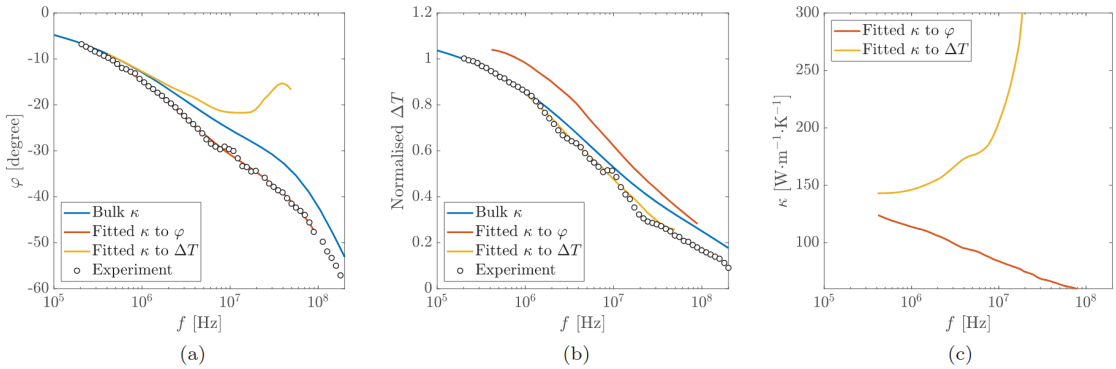

Figure 6.12: Failure of effective Fourier's law in the FDTR experiment. The presented results are for a temperature of 311 K. a) Phase shift φ and b) normalized oscillation amplitude ΔT as a function of the laser heating frequency. Bulk Fourier's law fails in the prediction of both experimental magnitudes. When an effective thermal conductivity is used to fit the phase shift, it fails to fit the oscillation amplitude, and the other way around, as shown in c). *Image extracted from [63].*

and only allow memory effects to be observed at temperatures below 200 K, providing very small corrections [63]. Here, we would like to mention that, due to this negligible effect, the *ab initio* heat-flux relaxation time in silicon can not be validated with this experiment, as we will point out in Section 6.4.

Including the nonlocal effects of the GKE allows studying the interface with deeper insight. In previous works, Fourier's law with a size-dependent TBR is used to interpret similar experimental results [18]. The size-dependent TBR is unnecessary in the present modelization case since the effects are captured with the GKE. Then, in order to characterize the TBR, we use the DMM. Since this model represents a lower bound and does not consider the experimental defects of the interface, it is reasonable to assume that the R in the interface (see Section 3.4.1) is proportional to the ideal situation. The experimental results at low frequencies are used to scale this value. Then, it results that $R = 2.71 R_{DMM}$, where R_{DMM} is the value obtained in the ideal DMM case. As seen in Figure 6.13, this new R (which has a temperature dependence given by R_{DMM}) predicts all the temperatures and frequencies without introducing parameters that depend on the situation [63]. We want to remark that this method to obtain the TBR is completely analogous to the one used in Section 6.1.3: we use a value proportional to the DMM value, which is obtained at low frequencies where Fourier's law is valid. Thus, we capture the experimental defects of the interface. When we increase the frequency, we do not change the value for the TBR. Then, it does not depend on the oscillation frequency.

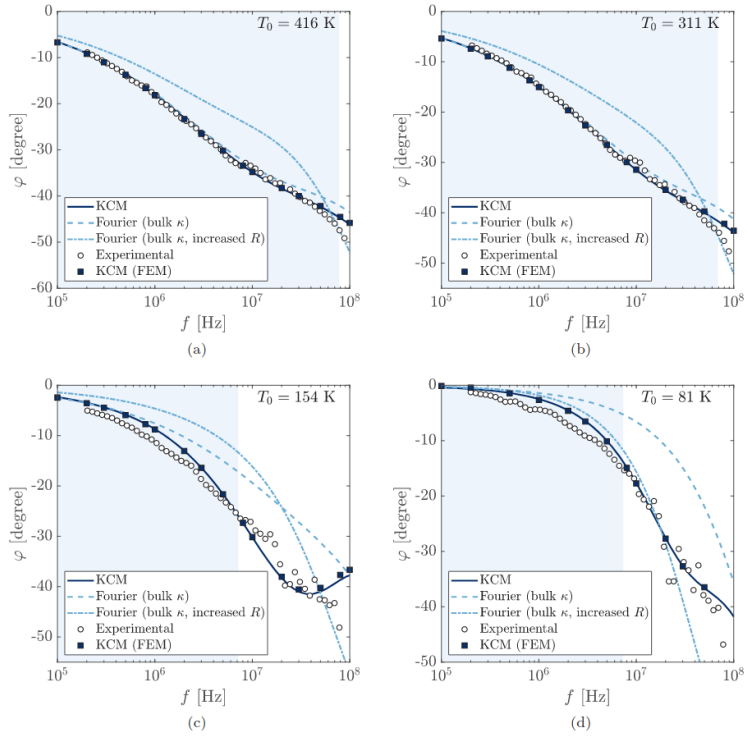

Figure 6.13: Phase shift ϕ as a function of the heating frequency for a) 416 K, b) 311 K, c) 154 K, and d) 81 K. In the figure is compared the experimental results with bulk Fourier's law, Fourier's law with a fitted TBR, and the GKE prediction (analytical and numerical (FEM) solutions). Fourier's law can not predict the results at all frequencies, especially at low temperatures. On the other hand, GKE predicts it for all the frequencies with *ab initio* parameters. *Image extracted from [63].*

Figure 6.13 shows the GKE and Fourier's prediction of the FDTR experiment for different temperatures and frequencies. Fourier's law fails to predict the experimental results as the frequency increases, while the GKE prediction reproduces the experiment for all the temperatures and frequencies with *ab initio* parameters.

In [131], the same experiment with germanium is performed, leading to the same modeling and conclusions as in the silicon results [63].

6.2 Memory effects in germanium

In the previous section of this chapter (Section 6.1), we analyzed the nonlocal effects of the GKE, going from time-independent (Sections 6.1.1 and 6.1.2) to time-dependent situations (Sections 6.1.3 and 6.1.4). This is, analyzing the effects of the $\ell^2(\nabla^2\vec{q} + \alpha\vec{\nabla}(\vec{\nabla}\cdot\vec{q}))$ in the GKE. In these referenced sections, there are no relevant memory effects (the effects of the $\tau\frac{\partial\vec{q}}{\partial t}$ of the GKE are negligible). In the present section, we analyze the effects of this memory term. There is a wide range of experiments supporting the nonlocal effects (see Section 6.1). However, we only have experimental evidence for the memory term in a semiconductor at ordinary temperatures in germanium [66], which is developed in Section 6.2.1.

6.2.1 Second sound: frequency domain thermoreflectance without transducer

In collaboration with Institut de Ciència de Materials de Barcelona (ICMAB)

As mentioned in Section 4.3, second sound is a transport phenomenon where heat is propagated as temperature waves. The typical definition is that second sound is the regime where the time-derivative of the heat flux is not negligible to describe the heat transport [69, 142]. This will be the definition used in this section, even though other authors restricted the existence of second sound to cases where a complete oscillation of temperature is observed [143]. Typically, second sound is described with the energy conservation in combination with the Maxwell-Cattaneo equation (MCE):

$$C_v \frac{\partial T}{\partial t} + \vec{\nabla} \cdot \vec{q} = P, \tag{6.8a}$$

$$\vec{q} + \tau \frac{\partial \vec{q}}{\partial t} = -\kappa \vec{\nabla} T, \tag{6.8b}$$

where P is the power density source (see Appendix G for a deeper insight, where we also show that the momentum transfer from photons to phonons is generally negligible).

As previously mentioned, this phenomenon was first theoretically predicted [69, 74, 142] and experimentally observed [61, 123, 144] for the collective regime. Nevertheless, this is not a necessary condition to observe this phenomenology. In [69], it is defined as the drifting second sound, the case where normal collisions dominate; and it is postulated as the driftless second sound, the case where it is not necessary to be in the collective regime, which is the case of study in the present experiment since we will describe germanium that is a kinetic material. This is not at odds with Section 4.3, where we concluded that FDF obtains the drifting second sound, but it was in the collective limit. However, both kinds of second sound (drifting and driftless) should accomplish some conditions to be observed [69]. First, the excitation frequency f (related to the external heat source P) should be large enough to unlock the time derivative of the heat flux in Equation (6.8b):

$$f\tau \gtrsim 1. \tag{6.9}$$

The second condition for observing second sound is related

to the nonlocal effects. In [69], it is postulated that, for the appearance of second sound, the drift operator must be negligible in front of the collision operator, meaning that the distribution function has no spatial variations. With this condition, it can be demonstrated that, by using the FDF, the MCE is recovered. Then, in conclusion, the source term P should have an oscillating frequency f large enough to accomplish both conditions. Figure 6.14 illustrates these conditions for initial Gaussian temperature distribution.

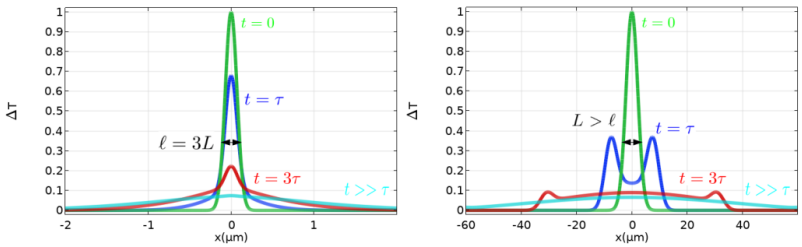

Figure 6.14: Evolution of Gaussian temperature distribution for different times with the GKE. On the left, the size of the system L is $\ell = 3L$, and on the right, the size is $L > \ell$. Second sound is only observed when $t \sim \tau$ and $L > \ell$. *Image extracted from [131].*

In the present section, we present a FDTR experiment without a metallic transducer [66]. Besides the experiments shown in Section 6.1.4, where the laser heats a transducer, and the heat is released from the transducer to the semiconductor, in this experiment, the laser directly heats the germanium substrate. Notice that, in all the previous modeled experiments reported in the present chapter, the heat source is not in the semiconductor, and heat is introduced from the boundary conditions. Then, it is the first experiment of this chapter where an energy source is directly introduced in the semiconductor.

We will predict the experimental results using the MCE instead of the GKE [66]. This guarantees the absence of nonlocal effects (the term $\ell^2(\nabla^2 + \alpha\vec{\nabla}(\vec{\nabla}\cdot\vec{q}))$ of the GKE), allowing the accomplishment of the necessary conditions for the second-sound observation. As introduced in Section 6.1.3, when the characteristic length of the experiment is reduced to sizes below the nonlocal length, the former is effectively reduced [65] (see Chapter 7 for a deeper insight). In this FDTR experiment, the only characteristic size is the optical penetration depth of the laser into the semiconductor, which is very small compared to ℓ [66]. Thus the effective nonlocal length should be negligible due to its reduction. Then, under these conditions, the GKE naturally results in the MCE.

From a microscopic point of view, we interpret this suppression of the nonlocal length as follows. Since the optical penetration depth is much smaller than the MFPs of the phonons, the phonon distribution function of these modes

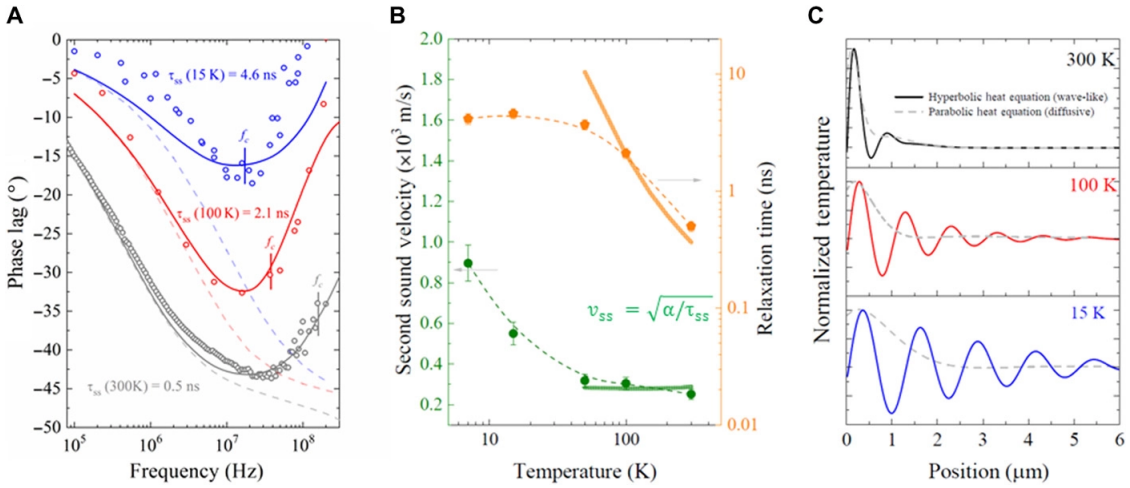

Figure 6.15: A) Phase lag depends on the frequency for 15 K, 100 K, and 300 K. Solid lines represent the Maxwell-Cattaneo prediction and the dashed line represents Fourier's prediction. B) Relaxation times and second-sound velocities at different temperatures. The dashed lines are guides to the eyes, and the solid lines are the theoretical predictions. C) Predicted Maxwell-Cattaneo's (solid line) spatial distribution of the temperature field at approximately 300 MHz compared with the diffusive case (dashed line). *Image extracted from [66].*

can not be accommodated to this large spatial variation. Then, it results in an effective suppression of their spatial derivative, which can not contribute to the nonlocal length. Consequently, the ℓ is reduced. This phenomenon is strongly related to the limited derivation of the FDF to moderate Knudsen numbers.

Figure 6.15.a shows the experimental results for the phase lag at different temperatures. Fourier's law and MCE predict the same result for low frequencies, reproducing the experimental result. This is because the memory term has no significant contribution since Equation (6.9) is not accomplished. When the frequency is increased to $f\tau \sim 1$, we observe a larger difference between Fourier's law and the MCE. MCE, with *ab initio* parameters, reproduces the experimental results at all frequencies. Thus, second sound is observed since the memory term has a relevant effect. Moreover, Figure 6.15.c shows the predicted spatial temperature distribution, where damped oscillations are observed.

Finally, Figure 6.15.b compares the predicted and the observed second-sound velocity and heat-flux relaxation time. As mentioned in Chapter 3, typically, the heat-flux relaxation time is considered to be $\tau_k \equiv d\kappa/(C_v \langle v_\lambda^2 \rangle)$, while the FDF predicts a different result (see Section 3.3). These two times are generally very different: while the first one underpredicts the memory effects, the former matches the experimental results.

6.3 Other experiments

The predictability power of the FDF, shown in the previous sections of this chapter, has convinced some authors to use the GKE with the *ab initio* parameters calculated in Chapter 5 [70] to model its experiments. This is the case of Xiang et al. [130], who model a TDTR experiment in silicon. There, they compare the output signals of the experiment with an effective Fourier's law with a fitted (and reduced) thermal conductivity and the GKE predictions with bulk thermal conductivity. They show that the GKE results in a predictive model because it agrees with the experimental data with bulk parameters. Contrarily, Fourier's law requires fitting parameters depending on the situation.

This is a remarkable result since the authors of [130] have used our model, with the *ab initio* parameters [70], to predict an experiment that is completely different from the ones modeled by our group. Thus, another completely different physical situation supports the applicability of the FDF.

6.4 Summary of the experimental support of the FDF

In this chapter, we have provided experimental evidence for a wide range of experiments for silicon and germanium. Figure 6.16 shows the experimental values for the nonlocal length ℓ and the heat-flux relaxation time τ used to reproduce the experiments, where it is seen the predictability power of the parameters obtained through the FDF for the GKE.

In time-dependent situations, the term $\alpha\vec{\nabla}(\vec{\nabla}\cdot\vec{q})$ of the GKE should, in principle, contribute to the prediction of the experimental results. Nevertheless, as mentioned in [131], its effects are negligible for the modeled experiments. This is also the case of the $\tau\frac{\partial\vec{q}}{\partial t}$ for the FDTR with transducer (Section 6.1.4). Then, we will not use α and τ to validate the model in Figure 6.16.

Finally, we would like to remark on all the experiments described by the GKE with the FDF parameters:

- Silicon thin films going from 100 K to room temperature and sizes going from hundreds of nanometers to bulk sizes [62]: Section 6.1.1.
- Silicon holey thin films going from 100 K to room temperature with characteristic sizes of the order of

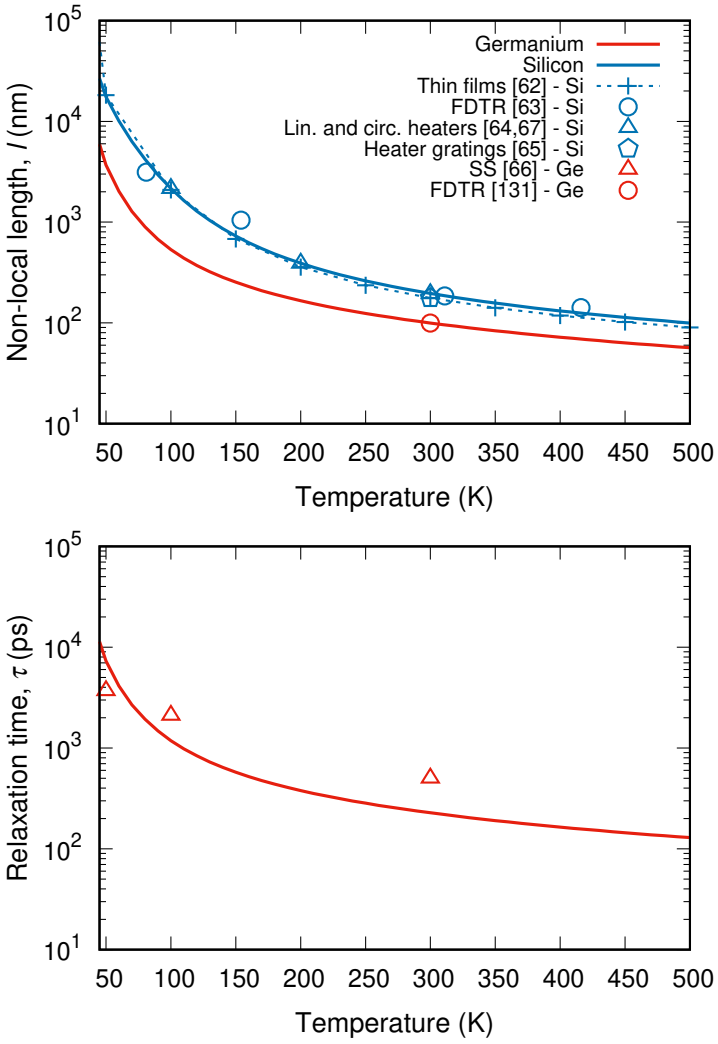

Figure 6.16: Summary of the experimental parameters used to describe the different situations in front of the predicted parameters in solid lines. In blue, silicon experiments, and in red, germanium experiments. The top figure represents the nonlocal. The blue and red solid lines represent the FDF nonlocal lengths for silicon and germanium, respectively. The blu dashed-cross line represents the ℓ values used in thin films [62], the blue hexagon is the one used in the heater gratings [65], blue triangles for the circular and linear heaters [64, 67], blue circles represent the nonlocal length used in the FDTR for silicon [63], and the red circle for germanium [131]. For the case of the heat flux relaxation time (bottom figure), the triangles represent the value used in the second sound in the germanium experiment [66].

microns [62]: Section 6.1.1.

- Linear and circular heaters on top of a silicon substrate. Temperatures range from 100 K to 300 K, and characteristic sizes of the heaters are of the order of microns [64, 67]: Section 6.1.2.
- Heater gratings: 1D- and 2D-confined heat sources on top of a silicon substrate. Characteristic sizes are in the range from hundreds of nanometers to microns [65]: Section 6.1.3.
- FDTR experiments in silicon and germanium with frequencies to hundreds of MHz and temperatures going from tens of Kelvin to room temperature [63, 131]: Section 6.1.4.
- Observation of second sound in germanium in a FDTR experiment with frequencies to hundreds of MHz and temperatures going from tens of Kelvin to room temperature [66]: Section 6.2.1.

- TDTR experiment in silicon with temperatures going from 80 K to room temperature [130]: Section 6.3.

Furthermore, since all these experiments have been predicted with a single characteristic length, the nonlocal length ℓ, it is reasonable to conclude that the thermal transport at these scales can be reproduced with a single-scale equation, the GKE (see Section 6.1.1.1 for an analysis of the difference between a single-scale and a multiscale behavior in silicon films). Moreover, the GKE's description of these experiments, since it resembles the NSE for fluids, suggests that hydrodynamic heat transport can be observed in kinetic materials.

Finally, we would like to mention that the GKE describes other experiments, although the parameters used are not calculated with the FDF. This is the case, for instance, of the InGaAs, where an experiment like the one presented in Section 6.1.2 with linear and circular heaters is performed [58]. Another example is the Bi2Te3, where the GKE is used to describe an interconnected nanowire network [145]. In both cases, the hydrodynamic equation describes the system's thermal behavior.

A similar example is molecular dynamics analysis. In [146] and in [147], they use the molecular simulation to observe, by means of the heat-flux profile, that the thermal behavior at scales of the order of tens of nanometers is reproduced with the GKE with effective parameters. These results, combined with the effective values used in Section 6.1.3 for heater gratings [65], open the door to justify using effective parameters when considering reduced length scales. Thus, it would increase the range of applicability of the FDF to larger Knudsen numbers.

An analysis of these phenomena out of the predictability region, presented in Section 6.1.1 [62], is performed in the next chapter.

7 Limitations of the model

In the previous chapter, we saw that the GKE with *ab initio* parameters obtained from the FDF explains a wide range of experiments. Nevertheless, there are some situations where the model is not predictive. In the present chapter, we present the model limitations reported in the different modelizations done (Section 7.1), and we provide some effective solutions to interpret the results (Section 7.2).

7.1 Model limitations

When sizes below twice the nonlocal length are considered, we fail to model silicon thin films with the GKE with *ab initio* parameters (Section 6.1.1) [62]. Then, we defined the applicability region as $W \gtrsim 2\ell$ or, by defining the Knudsen number as $\mathrm{Kn} \equiv \frac{\ell}{W}$, this condition writes $\mathrm{Kn} \lesssim \frac{1}{2}$. We use that W is the characteristic size of the experiment, for example, the width of the thin film, the radius of the nanowire, the width of a heater... Figure 6.2 shows this failure when $\mathrm{Kn} > \frac{1}{2}$ by comparing the GKE prediction and the experimental results.

This limitation is also present in other experiments apart from the thin films'. In Section 6.1.3, we considered the characteristic length of the experiment to be the distance between two consecutive heaters [65]. When $\mathrm{Kn} > \frac{1}{2}$, the nonlocal length ℓ has to be modified to reproduce the experimental results. We obtain a similar conclusion in Section 6.1.2 [67]: the GKE does not correctly predict the temperature profile for the lower temperature and the smaller circular heater

case.

From the perspective of our derivation, the reason for the model failure is the expansion of the distribution function. As mentioned in Chapter 3, the derivation of the GKE is valid for finite Knudsen numbers [70], i.e., we can not describe extreme nonequilibrium situations.

Figure 7.1 shows microscopic evidence of this failure. A circular heater is considered on top of a silicon substrate at 100 K. When the size of the heater is reduced, the GKE predicts some points near the heater with temperatures below 100 K, which is surprising. Interestingly, one can shed some light on this issue by studying the distribution function supplied by the FDF. When considering a point very close to the heater, the phonon distribution function has numerous phonon modes with a negative distribution function, with a non-negligible contribution to thermal conductivity. However, in the same experimental situation, the phonon distribution function is mainly positive considering a point far from the heater.

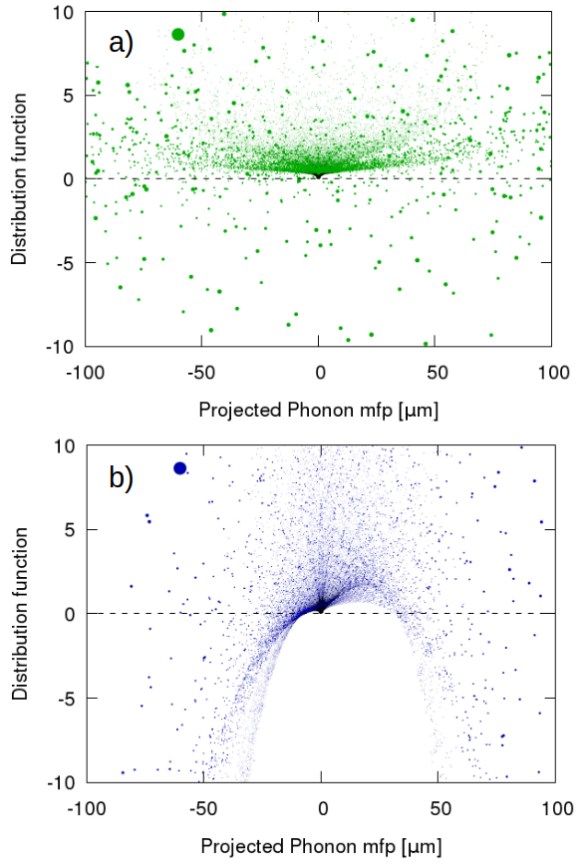

Figure 7.1: Phonon distribution function for a circular heater. The top figure (a) represents the distribution function at a point far from the heater and, then, not far from the equilibrium distribution function. The bottom figure (b) represents a point near the heater and then far from the equilibrium distribution function. The projected MFP refers to $v_{\lambda,x}\tau_\lambda$. It can be seen that the distribution function for the predictive (a) case has a positive distribution function for all the phonon modes (except for some of them that represent less than the 5 % of the contribution to the thermal conductivity [67]). When not in the predictive region, numerous phonon modes have a negative distribution function, which has no physical sense. *Image extracted from [67].*

This failure of the phonon distribution function indicates that the predicted reduced temperatures close to the heater

are an artifact of the model. It also suggests that a refinement of the GKE derivation through the FDF can be done.

7.2 Effective parameters modelization

To effectively overcome the limitation of the GKE to larger Knudsen numbers (Kn $> \frac{1}{2}$), we propose some solutions to improve our applicability region. These solutions use effective parameters instead of *ab initio* ones. Nevertheless, we would like to remark that a single effective parameter is used in every situation, and the thermal conductivity is always the bulk thermal conductivity.

7.2.1 Effective nonlocal length

In Section 6.1.3, we proposed to use an effective nonlocal length [65]. When the distance between the heaters is reduced below the applicability limit, we proposed a nonlocal length that is half of this distance (see Section 6.1.3 for the explanation of the experimental setup). The prediction of the GKE using this new nonlocal length matches the experimental results (see Figure 6.10). Notice that even though it is an effective parameter, we use simple geometrical arguments.

This result, combined with the underprediction of the thermal conductivity of the GKE with *ab initio* parameters for thin films, suggests that the viscous effects described by the nonlocal term in these situations are overpredicted. This supposition is supported by molecular dynamics experiments: in [148], they simulate through this technique an experiment of a heater grating, as in Section 6.1.3 [65]. They observe that when the distance between the heater lines is reduced to the sizes of the order of the MFPs of the phonons, there is an increase in the scattering rate between phonons. Since the nonlocal length is related to the average MFP (see Equation (5.2d)), when the scattering rate is increased, the phonon relaxation time τ_λ is decreased, and then, the ℓ is reduced.

7.2.2 Effective slip boundary condition

In the same direction as the previous section, we see in the present one that an effective C in the slip boundary condition can reproduce large Knudsen number situations for the silicon thin films' case.

To do so, it is helpful to plot the experimental results

and the GKE prediction depending on the Knudsen number $\mathrm{Kn} = \frac{\ell}{W}$, where W is the width of the thin film and ℓ is the *ab initio* nonlocal length, as shown in Figure 7.2. There, all the experimental points "collapse" in a single line. This suggests the next conclusion: the heat transport in silicon thin films, even at large Knudsen numbers, is characterized by a single length scale and, furthermore, this length scale is the *ab initio* nonlocal length ℓ provided by the FDF. However, the GKE with *ab initio* parameters underpredicts the experimental effective thermal conductivity for large Knudsen numbers, i.e., out of the applicability region, as seen in Figure 7.2. We attribute this underprediction to the overestimation of viscous effects.

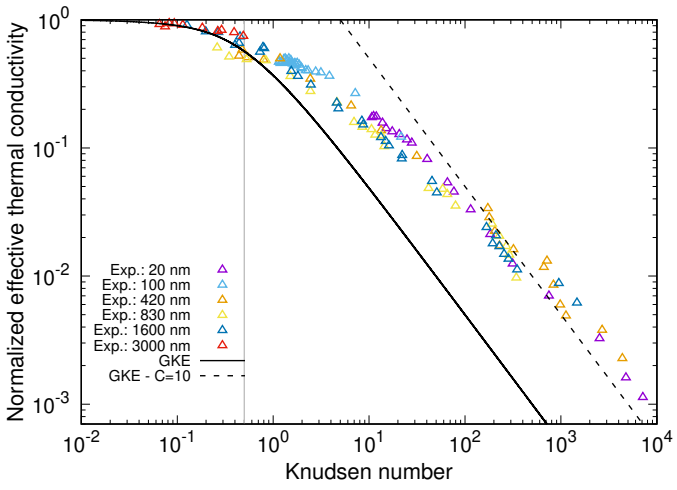

Figure 7.2: Effective thermal conductivity for silicon thin films as a function of the Knudsen number. The black-solid line represents the GKE prediction with *ab initio*, the black-dashed line represents the results of Equation (7.1) (only valid for large Knudsen numbers) with $C = 10$. The gray vertical line represents the limit of the applicability region ($\mathrm{Kn} = \frac{1}{2}$). Triangles are the experimental values for different thin film sizes [22, 23, 76].

As shown in Section 6.1.1, we have the expression for the effective thermal conductivity predicted by the GKE for thin films [136]: Equation (6.1). Since in this section we are focused on large Knudsen numbers, we use this equation to obtain the expression in the limit of $\mathrm{Kn} \to \infty$:

$$\frac{\kappa_{eff}}{\kappa} = \frac{C}{2\mathrm{Kn}}. \tag{7.1}$$

This equation shows that, by increasing the C, the effective thermal conductivity of the GKE prediction is also increased. Using an effective C for large Knudsen numbers, we can fit the experimental results and obtain the parameter that characterizes the system at these scales (in Figure 7.2, we use $C = 10$, which is an order of magnitude larger than the *ab initio* value). Figure 7.2 shows that the bulk C reproduces the experimental results for the applicability region ($\mathrm{Kn} \lesssim 1/2$). Nevertheless, this figure suggests a transition from the bulk C to the effective one when we increase the

Knudsen number.

Finally, a comment on the difference between the GKE's single scale and the RTA's multiscale is in order. In Equation (6.1), we have observed that the multiscale behavior seems not to reproduce the experimental results for small Knudsen numbers (Kn $\lesssim \frac{1}{2}$), and the results for large Knudsen numbers are in the same direction. The GKE underpredicts the effective thermal conductivity but captures the characteristic size of the experiment. On the contrary, the RTA prediction can not capture the behavior, as shown in Figure 7.3. This is another probe that suggests that, even at large Knudsen numbers, thermal transport for silicon thin films obeys a single-scale behavior.

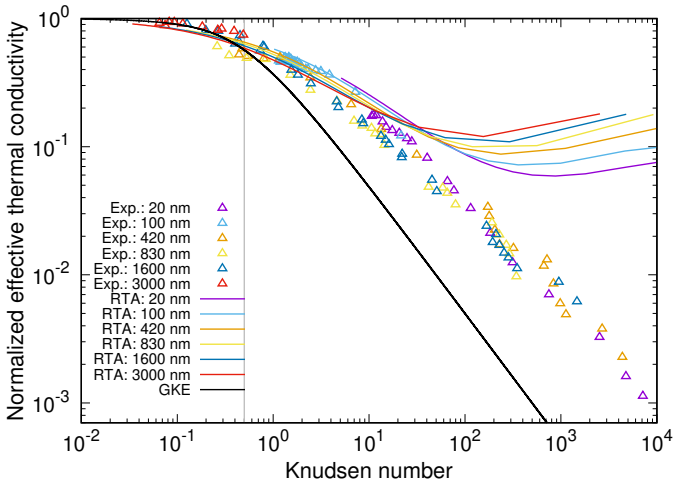

Figure 7.3: Effective thermal conductivity for silicon thin films as a function of the Knudsen number. The black-solid line represents the GKE, and the color lines represent the RTA predictions for different thin film sizes. Triangles are the experimental values for different thin film sizes [22, 23, 76].

8 Conclusions

The applicability of the GKE in kinetic materials like silicon, observed in many experiments performed in the last decade, urged for a theoretical formulation. The main conclusion of the present thesis is that the GKE can be derived from the BTE under quite general conditions, i.e., a general collisions operator and arbitrary dispersion relations for moderate Knudsen numbers. We have developed a brand-new method for solving the BTE, the Flux derivatives formalism (FDF), for this derivation. It provides microscopic expressions for all the transport parameters appearing in the GKE and can be calculated from *ab initio*.

The general belief in the thermal transport community is that hydrodynamic heat transport only appears in the collective limit since, in the original work, the GKE was derived when normal collisions dominate [52]. The FDF [70, 121], presented in Chapter 3, generalizes it and, moreover, guarantees the conservation of the energy without any assumption on the collision operator.

Furthermore, the FDF not only provides the mesoscopic equations (GKE and energy conservation equation) but also provides a solution for the BTE consistent with them. This solution is given by the distribution function (Equation (3.15)) and the corresponding weight functions (Equations (3.22a)-(3.22d)). This allows having a complete description of the system, not only from a mesoscopic point of view but also from a microscopic one. In fact, to our knowledge, we supply for the first time a simple expression for the phonon distribution under unsteady inhomogeneous conditions in terms of

first-principles quantities [70].

In addition, this distribution function allows to derive proper boundary conditions, using kinetic theory, consistent with the mesoscopic equations (see Section 3.4). Then, this "triangle" of the transport equations, the distribution function, and the boundary conditions provide a full picture to describe thermal transport in general dielectrics. Moreover, the GKE with the boundary conditions are very easy to numerically implement with FEM. Then, it is a powerful tool to model heat transport in dielectrics at the nanoscale.

This formalism is supported by two different perspectives: theoretical and experimental. From the theoretical perspective, we recover two well-known results in thermal transport. First, we obtain Fourier's law with a general collisions operator (Section 3.2). Second, we exactly recover the original results for the Guyer and Krumhansl equation, where it is used that normal collisions dominate (Chapter 4). Furthermore, in the collective limit, we solve a long-standing issue on drifting and driftless second-sound velocities.

From the experimental perspective, the FDF is supported for a wide range of situations, as shown in Chapter 6: for different materials (silicon and germanium), for stationary and time-dependent situations, for different sizes (going from hundreds of nanometers to bulk materials), different geometries (thin films, linear and circular heaters, thermal gratings, FDTR experiments...), and for different temperatures (going from tens of Kelvin to room temperature).

This experimental validation allows us to obtain three conclusions. First, even with an effective thermal conductivity, Fourier's law can not predict experimental results at nanoscale sizes, demonstrating that Fourier's law and its effective theories can not get all the physics beyond the nanoscale. Second, the *ab initio* parameters obtained from the FDF can reproduce quite a number of experiments when $L \gtrsim 2\ell$, with L the characteristic size of the experiment, in consistence with our GKE derivation, thus supporting the formalism. Third, a single scale, the nonlocal length ℓ, describes a wide range of experiments in silicon, which is a property of the GKE. In contrast, alternative derivations of the BTE, like RTA, predict a multiscale behavior for silicon thin films [31]. Since the GKE describes the experiments, we can conclude that thermal transport in silicon shows a hydrodynamic behavior with nonlocal effects given by the nonlocal length ℓ.

This last conclusion is supported even in situations out of our predictability region (when the characteristic size of the experiment is $L \gtrsim 2\ell$ [62]). In Chapter 7, it is shown that the characteristic length describing the effective thermal conductivity of silicon thin films is the nonlocal length ℓ even far away from the applicability region ($L < 2\ell$). There, we can predict the experimental results by increasing the C-parameter in the slip-boundary condition, but without changing the transport equation: the GKE. Thus, extending the hydrodynamic phenomena to large Knudsen numbers.

Finally, this last conclusion allows opening the study of the FDF out of the predictability region. The refinement of the formalism, especially by improving the derivation of the boundary conditions with *ab initio* calculation, as shown in Section 7.2, would enhance the region of applicability.

Appendix

Ab initio calculations A

The numerical values of the transport parameters presented in this thesis are performed using a version of the code presented in [149] developed by our group. Nevertheless, the code has been improved to implement the different expressions of the transport parameters presented in Chapters 4 and 5.

The transport parameters have been calculated from first principles using the Vienna Ab initio Simulation Package (VASP) [150–153], which implements Density Functional Theory (DFT). The potentials used are projected augmented wave (PAW) potentials under the Perdew-Burke-Ernzerhof (PBE) framework [154, 155]. The plane wave energy cutoff used is 10 % higher than the value proposed in the pseudopotential file. A 5x5x5 supercell created from an 8-atom cubic unit cell is used. Phonopy package is used for harmonic calculations [156], while for anharmonic calculations Phono3py is used [157]. For the case of BAs, we have used the calculations present in [158].

From the point of view of convergence, we perform a study as a function of the grid points in the wave-vector space. In Figure A.1, the parameters at room temperature (T=300K) are plotted as a function of the number of grid points in the wave-vector space. There, it can be seen that the parameters converged. Notice that the *hydrodynamic* parameters (τ, τ_p, ℓ and α) converge at larger meshes than the thermal conductivity. Under the RTA, this phenomenon is easily argued. The thermal conductivity is proportional to the relaxation time $\kappa \propto \langle \tau_\lambda \rangle$ (Equation (2.11)), while the other parameters have

a term proportional to the squared relaxation time, $\propto \langle \tau_\lambda^2 \rangle$ (Equations (5.2a)-(5.2e)). This implies that phonon modes of lower frequency ω_λ and larger relaxation time τ_λ have a larger contribution, and denser meshes are required.

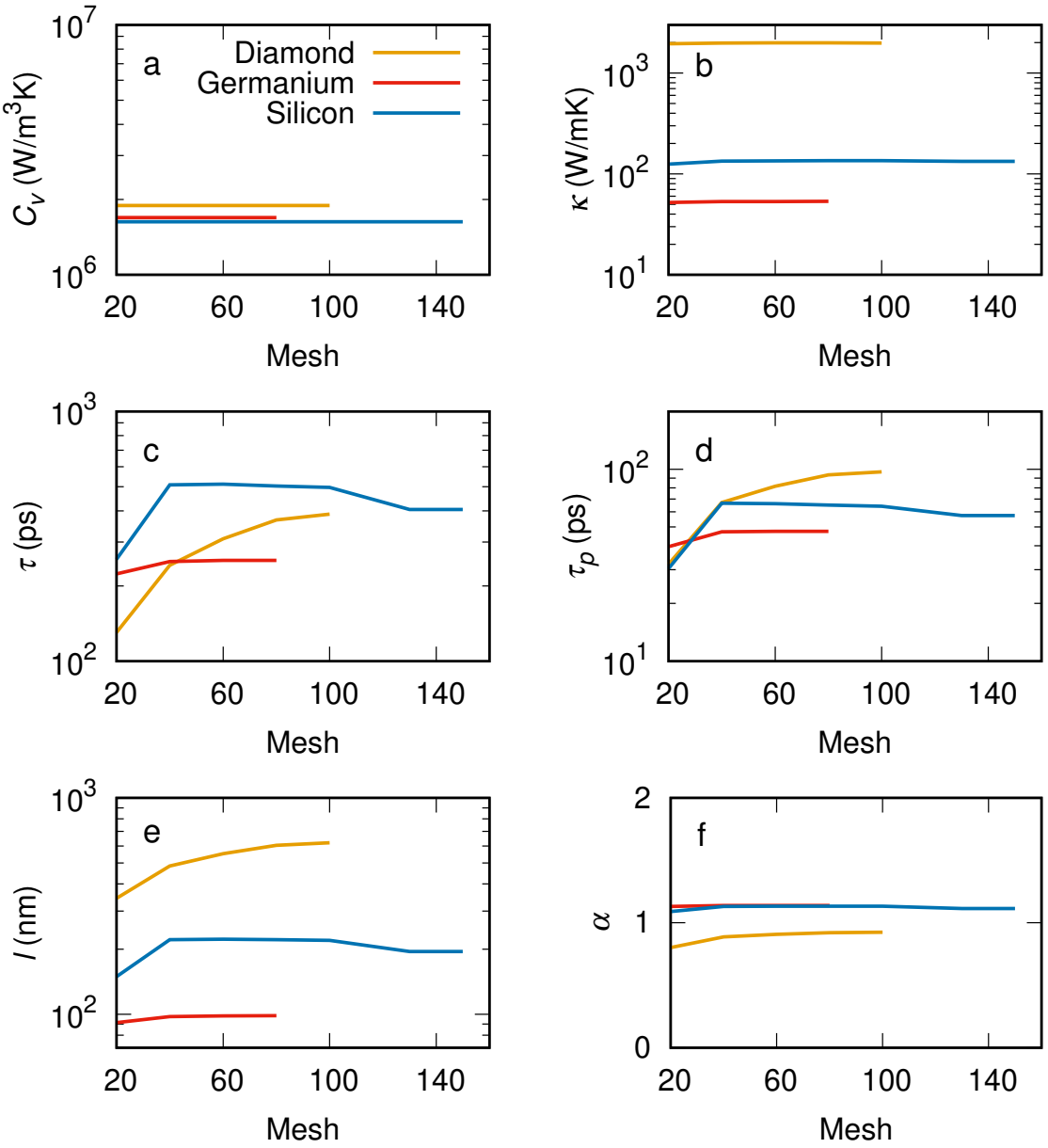

Figure A.1: First-principle macroscopic parameters as a function of the mesh for silicon (blue), germanium (red), and diamond (yellow) in RTA at room temperature (T = 300K). a) Specific heat C_v. b) Thermal conductivity κ. c) Relaxation time τ. d) Relaxation time τ_p. e) Non-local length ℓ. f) Parameter α. *Image extracted from [70].*

A.1 Convergence of low-dimension materials

The results presented in Section 3.3 are presented for arbitrary d-dimension materials. The applicability of the results requires that the integrals appearing therein do not diverge. This issue is delicate in low-dimensional systems due to the dispersion relations of flexural modes. In stress-free 2D materials, harmonic models of flexural modes display dispersion relations $\omega_{\lambda,flex} \propto k_\lambda^2$; as a result, the normalization constant of vectors $|\phi_i^1\rangle$ yields $\int k_\lambda^3/\omega_\lambda^2 dk \propto \int 1/k\, dk$, which diverges for infinite samples. This divergence led [28] to use the driftless expression for second sound in graphene. The coupling of out-of-plane and in-plane modes renormalizes the dispersion relation of flexural modes so that at low frequencies $\omega_{\lambda,flex} \propto k_\lambda^{3/2}$ [159, 160] and the divergence disappears. The renormalized dispersion relation was used in the numerical solution of the BTE performed in [126] obtaining in the collective limit thermal waves with propagation velocity equal to the drifting expression, in agreement with our formalism.

Nevertheless, the $\omega_\lambda \propto k_\lambda^{3/2}$ dependence and, in general, dispersion relations $\omega_\lambda \propto k_\lambda^\delta$ with $\delta > 1$ exhibit a problem when applied to the displaced distribution in the thermodynamic limit. The latter yields negative values for small frequencies [43, 114], so the displaced distribution cannot be a correct solution at these frequencies. This contrasts, however, with iterative solutions of the BTE for graphene and other 2D substances, which seem to provide displaced distributions [28, 54]. This might be due to the finite wavevector lower bound used in the discretization of the reciprocal space, which may not reach the region of negative values. The question arises of which is the appropriate phonon distribution in the collective limit in this situation. Whichever it is, substituting the corresponding $\vec{\beta}_\lambda^{col}$ in the root expressions of Section 3.3 would yield the transport coefficients. In a recent paper [161], the authors address this issue and find that for large 2D samples, the drift velocity is negligible, and SS propagates with a (driftless) velocity given by $v_{SS}^2 = \frac{\kappa}{C\tau_q}$, where τ_q is the relaxation time of the heat flux, in agreement with our Equation (4.21). Let us note in passing that the latter driftless velocity does not necessarily coincide with the classical expression of the driftless velocity, Equation (4.18).

Finally, under strain, dispersion relations of flexural modes in 2D materials seem to become linear at low wavevectors [162, 163] so that convergence of normalization constant is guaranteed. However, the convergence of the thermal conductivity, in this case, is still unclear both computationally and experimentally [114, 161, 163]. In 1D, also theoretical models often provide divergent thermal conductivities, though the inclusion of three-phonon scattering to second order seems to yield finite values [114]. The latter property is required to apply the present approach in its current form.

A.2 Relaxation times

Here, we show that the $\tau_p^2 \frac{\partial^2 \vec{q}}{\partial t^2}$ appearing on the GKE derived with the FDF is much smaller than the $\tau \frac{\partial \vec{q}}{\partial t}$. Thus, it can be neglected and the GKE derived recovers the original GKE shape [52]. This is shown in Figure A.2, where it can be seen that $\tau \gg \tau_p$. When considering an excitation of frequency ω

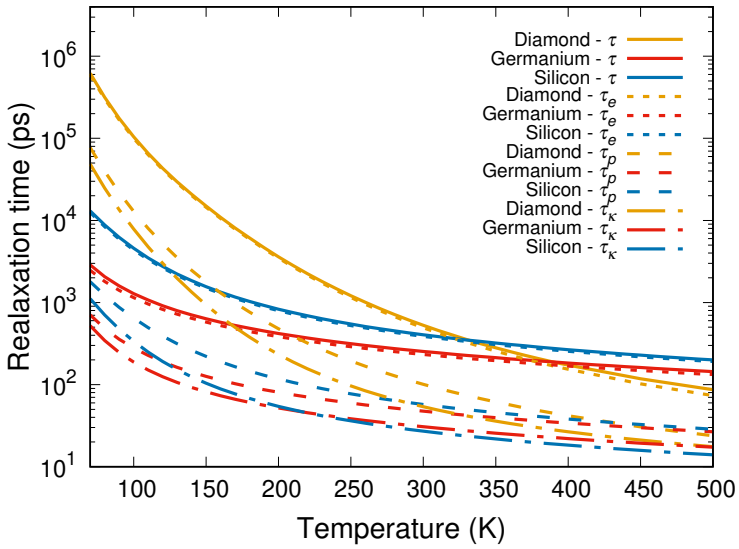

Figure A.2: Temperature dependence of the heat flux relaxation time τ, τ_e, τ_p and τ_κ parameters for diamond (yellow), germanium (red), and silicon (blue). τ and τ_e are an order of magnitude larger than τ_p and τ_κ.

and the situation where $\omega\tau < 1$, the $\tau_p^2 \frac{\partial^2 \vec{q}}{\partial t^2}$ and $\tau \frac{\partial \vec{q}}{\partial t}$ are $\omega^2\tau_p^2$ and $\omega\tau$, respectively. By comparing these two terms $\frac{\omega^2\tau_p^2}{\omega\tau}$, one can obtain that $\frac{\omega^2\tau_p^2}{\omega\tau} = \omega\tau_p\frac{\tau_p}{\tau} \ll \omega\tau_p \ll \omega\tau < 1$. Thus, concluding that $\omega^2\tau_p^2 \ll \omega\tau$ and then $\tau_p^2 \frac{\partial^2 \vec{q}}{\partial t^2} \ll \tau \frac{\partial \vec{q}}{\partial t}$.

Figure A.2 also shows that the usually used relaxation time in the Maxwell-Cattaneo equation or the GKE $\tau_\kappa \equiv \frac{d\kappa}{C_v\langle v_\lambda\rangle}$ is much shorter than the one predicted by the FDF τ. Then, memory effects appear at smaller frequencies.

Symmetrized scattering matrix

B

The linearized BTE can be symmetrized by introducing a reference temperature T_0, defining $f_\lambda^0 = f_\lambda^{eq}(T_0)$, and rescaling the phonon deviation from equilibrium $n_\lambda = f_\lambda - f_\lambda^0$ as follows

$$n_\lambda^* = \frac{n_\lambda}{\sqrt{f_\lambda^0(f_\lambda^0+1)}}. \tag{B.1}$$

Then the BTE writes

$$\frac{\partial n_\lambda^*}{\partial t} + \vec{v}_\lambda \cdot \vec{\nabla} n_\lambda^* = -\sum_{\lambda'} \Omega_{\lambda\lambda'}^* n_{\lambda'}^*, \tag{B.2}$$

where Ω^* is the symmetric, self-adjoint, scattering operator [52]

$$\Omega_{\lambda\lambda'}^* = \sqrt{\frac{f_{\lambda'}^0(f_{\lambda'}^0+1)}{f_\lambda^0(f_\lambda^0+1)}}\Omega_{\lambda\lambda'}. \tag{B.3}$$

Analogously, one can define the symmetrized normal N^* and resistive R^* scattering operators, with $\Omega^* = N^* + R^*$.

The distribution function can be expressed in terms of the eigenvectors of the symmetrized Normal scattering operator N^*, which is an orthogonal basis of the phase density space, and take advantage that four of these eigenvectors are known, namely ϕ_λ^0 and $\phi_{\alpha\lambda}^1$ (α is the index of the spatial component) [52]. They are related to the equilibrium and displaced Bose-Einstein distributions, respectively, and read

$$\phi_\lambda^0 = c_0\,\hbar\omega\sqrt{f_\lambda^0(f_\lambda^0+1)} \tag{B.4}$$

$$\phi^1_{\alpha\lambda} = c_1\,\hbar k_\alpha \sqrt{f^0_\lambda (f^0_\lambda + 1)}, \tag{B.5}$$

with c_i normalization constants so that $<\phi^0_\lambda|\phi^0_\lambda>=<\phi^1_{\alpha\lambda}|\phi^1_{\alpha\lambda}>=1$, and the scalar product is defined as $<f\mid g>= V\int f(\lambda)g(\lambda)\,d\lambda$. The eigenvalues of these eigenvectors are zero, which indicates that they describe equilibrium states under N scattering.

Energy and momentum projection

C

In Section 3.1, we have used the projections of the BTE to energy (Equation (3.1a)) and momentum (Equation (3.1b)) for the FDF. These projections can be physically argued through the conserved magnitudes of the energy and the crystal momentum of normal collisions, and this is what is done in this appendix.

In general, the BTE is written as (Equation (2.3))

$$\frac{\partial f_\lambda}{\partial t} + \vec{v}_\lambda \cdot \vec{\nabla} f_\lambda = C(f_\lambda). \tag{C.1}$$

The collisions operator can be separated as the momentum-conserving collisions (or normal collisions) $N(f_\lambda)$ and the momentum-destroying collisions (or resistive collisions) $R(f_\lambda)$, giving that $C(f_\lambda) = R(f_\lambda) + N(f_\lambda)$ without losing generality.

Then, we impose the two physical conditions required: the energy conservation of the collisions operator and the momentum conservation of normal collisions. From the first condition $\int \hbar\omega_\lambda C(f_\lambda) d\lambda = 0$, it is obtained that

$$\frac{\partial e}{\partial t} + \vec{\nabla} \cdot \vec{q} = 0, \tag{C.2}$$

which is Equation (3.1a). From the momentum conservation of the normal collisions, $\int \hbar\vec{k}_\lambda N(f_\lambda) = 0$ it is obtained

$$\frac{\partial \vec{p}}{\partial t} + \vec{\nabla} \cdot \overline{\overline{\Pi}} = \int \hbar\vec{k}_\lambda R(f_\lambda) d\lambda. \tag{C.3}$$

Nevertheless, in principle, the preservation of momentum in normal collisions must be guaranteed for any collisions operator, meaning that $\int \hbar\vec{k}_\lambda R(f_\lambda)d\lambda = \int \hbar\vec{k}_\lambda C(f_\lambda)d\lambda$ and, then, recovering the momentum projection used in the FDF (Equation (3.1b)).

A comment on the RTA collision operator. These two arguments to project to the energy and the momentum are valid as long as the collision operator imposes the corresponding energy and momentum conservation conditions. As in Equation (3.24), energy conservation is guaranteed for whatever the collision operator is.

Nevertheless, for the momentum conservation case, it is different. The typical RTA collisions operator does not guarantee $\int \hbar\vec{k}_\lambda N(f_\lambda)d\lambda = 0$. This is because there is no imposition in the vectorial component of the collisions operator since

$$N(f_\lambda) = -\frac{f_\lambda - f_\lambda^{eq}}{\tau_{N,\lambda}}, \tag{C.4}$$

which $\tau_{N,\lambda}$ is the normal collisions time that, combined with Mathiessen's rule, gives the typical RTA result τ_λ.

To give an example, the $\vec{\beta}_\lambda$ is treated. In the RTA, it is obtained (Equation (5.1)) that

$$\vec{\beta}_\lambda = \frac{\tau_\lambda}{\kappa}\frac{\partial f_\lambda^{eq}}{\partial T}\vec{v}_\lambda \tag{C.5}$$

and $N(\vec{\beta}_\lambda) = -\vec{\beta}_\lambda/\tau_{N,\lambda}$. Then the condition for the momentum conservation is

$$\frac{1}{\kappa}\int \hbar\vec{k}_\lambda \frac{\tau_\lambda}{\tau_{N,\lambda}}\frac{\partial f_\lambda^{eq}}{\partial T}\vec{v}_\lambda d\lambda = 0, \tag{C.6}$$

which gives the condition that $\left\langle \frac{v_\lambda}{v_{p,\lambda}}\frac{\tau_{R,\lambda}}{\tau_{R,\lambda}+\tau_{N,\lambda}} \right\rangle = 0$. Since all the appearing magnitudes in the RTA are positive, this condition cannot be accomplished, and the momentum conservation of the normal collisions is not satisfied.

Mathematical relations D

In this appendix, some mathematical relations used in previous chapters are derived. All these mathematical relations are derived assuming an isotropic material and assuming a d-dimensions material.

D.1 Second-order isotropic tensor

In an isotropic material, a second-order mode-independent tensor can be expressed as

$$\int A_\lambda v_{\lambda,i} v_{\lambda,j} d\lambda = B \int A_\lambda v_\lambda^2 d\lambda \, \delta_{ij}, \tag{D.1}$$

where $v_{\lambda,i}/v_\lambda$ is the unitary vector of the λ-mode at the i-direction, A_λ is a scalar that depends on the λ-mode, B is a constant that must be determined, and δ_{ij} is the Kronecker delta. If we define $A_{ij} \equiv \int A_\lambda v_{\lambda,i} v_{\lambda,j} d\lambda$ and $A' \equiv \int A_\lambda v_\lambda^2 d\lambda$, Equation (D.1) results in

$$A_{ij} = BA' \delta_{ij}. \tag{D.2}$$

From this relation, it can be obtained that $A_{xx} = BA'$ and $A_{xy} = 0$. Now, let us calculate A'

$$A' \equiv \int A_\lambda v_\lambda^2 d\lambda = \int A_\lambda \sum_{i=1}^{d} v_{\lambda,i}^2 d\lambda = \sum_{i=1}^{d} \int A_\lambda v_{\lambda,i}^2 d\lambda, \tag{D.3}$$

where it has been used that $v_\lambda^2 = \sum_{i=1}^{d} v_{\lambda,i}^2$. Since an isotropic material is considered, $\int A_\lambda v_{\lambda,i}^2 d\lambda = \int A_\lambda v_{\lambda,j}^2 d\lambda$ for what-

ever combination of any i and j, meaning that

$$A' = d \int A_\lambda v_{\lambda,i}^2 d\lambda = d \int A_\lambda v_{\lambda,x}^2 d\lambda, \tag{D.4}$$

which gives that $A' = dA_{xx}$ that combined with Equation (D.1), gives that

$$\int A_\lambda v_{\lambda,i} v_{\lambda,j} d\lambda = \frac{1}{d} \int A_\lambda v_\lambda^2 d\lambda \delta_{ij}. \tag{D.5}$$

D.2 Fourth-order isotropic tensor

In an isotropic material, the following fourth-order tensor can be expressed as

$$\begin{aligned} &\int A_\lambda v_{\lambda,i} v_{\lambda,j} v_{\lambda,k} v_{\lambda,l} d\lambda \\ &= B \int A_\lambda v_\lambda^4 d\lambda \left(\delta_{ij}\delta_{kl} + \delta_{ik}\delta_{jl} + \delta_{il}\delta_{jk}\right), \end{aligned} \tag{D.6}$$

where A_λ is a scalar that depends on the λ-mode and B is a constant that must be determined. If we define $A_{ijkl} \equiv \int A_\lambda v_{\lambda,i} v_{\lambda,j} v_{\lambda,k} v_{\lambda,l} d\lambda$ and $A' \equiv \int A_\lambda v_\lambda^4 d\lambda$, Equation (D.6) results in

$$A_{ijkl} = BA' \left(\delta_{ij}\delta_{kl} + \delta_{ik}\delta_{jl} + \delta_{il}\delta_{jk}\right). \tag{D.7}$$

From this relation, it can be obtained that $A_{xxxx} = 3BA'$ and $A_{xxyy} = BA'$. Now, let us calculate A'

$$A' \equiv \int A_\lambda v_\lambda^4 d\lambda = \int A_\lambda \sum_{i=1}^{d} v_{\lambda,i}^2 \sum_{i=j}^{d} v_{\lambda,j}^2 d\lambda, \tag{D.8}$$

where it has been used that $v_\lambda^2 = \sum_{i=1}^{d} v_{\lambda,i}^2$. The previous expression can be written as

$$A' = \int A_\lambda \left(\sum_{i=1}^{d} v_{\lambda,i}^4 + \sum_{i\neq j=1}^{d} v_{\lambda,i}^2 v_{\lambda,j}^2 \right) d\lambda, \tag{D.9}$$

where the diagonal and non-diagonal terms have been separated. Then, it can be seen that

$$A' = dA_{xxxx} + (d^2 - d)A_{xxyy}. \tag{D.10}$$

But we have already seen that $A_{xxxx} = 3A_{xxyy}$, then $A' = 3dA_{xxyy} + (d^2 - d)A_{xxyy}$. This, combined with $A_{xxyy} = BA'$, gives the result that

$$A_{ijkl} = \frac{1}{d(d+2)} A' \left(\delta_{ij}\delta_{kl} + \delta_{ik}\delta_{jl} + \delta_{il}\delta_{jk} \right). \qquad \text{(D.11)}$$

Alternative derivation of the GKE in the kinetic limit

E

In this appendix, the presented derivation is an alternative derivation of the GKE in the kinetic limit, i.e., using the RTA collisions operator. This derivation recovers exactly the results of Section 5.1 with a different procedure.

In order to overcome the drawbacks of the macroscopic equations obtained through the Chapman-Enskog (CE) and Grad moment methods beyond Navier-Stokes-Fourier equations, in the last decades it has been developed the so-called regularized moment method [109]. In this appendix, we present a regularized moment method that provides the same nonequilibrium distribution and macroscopic equations found in ref. [70] through the FDF.

A key difference of the present derivation with respect to the one in ref. [57] is the nonequilibrium function that is employed in the CE expansion. In ref. [57], the expansion was performed around a nonequilibrium distribution found from maximizing phonon entropy for a given energy density and heat flux, thus obtaining a four-moment nonequilibrium function. As in the case of the Grad moment distributions used in the kinetic theory of gases, the latter function is built independently of the BTE, which comes into play only through the moment equations. In contrast, we start from a nonequilibrium function that is close to a first-order solution of the BTE.

The BTE with the RTA collisions operator (Equation (2.10)),

$$\frac{\partial f_\lambda}{\partial t} + \vec{v}_\lambda \cdot \vec{\nabla} f_\lambda = -\frac{f_\lambda - f_\lambda^{eq}}{\tau_\lambda}, \tag{E.1}$$

is used with its projections onto energy and quasimomentum (Equations (3.1a)-(3.1b)).

To first order in the Knudsen number, the CE method yields for the distribution function the well known result $f_\lambda = f_\lambda^{eq} - \tau_\lambda \partial_T f_\lambda^{eq} \vec{v}_\lambda \cdot \vec{\nabla} T$, which directly supplies Fourier's law, $\vec{q} = -\kappa \vec{\nabla} T$. Note that a CE expansion of this function gives rise to second spatial derivatives of temperature and then to macroscopic equations of the Burnett type, which are unstable. Instead, we rewrite the distribution function as

$$f_\lambda^4 = f_\lambda^{eq} + \frac{\tau_\lambda}{\kappa} \frac{\partial f_\lambda^{eq}}{\partial T} \vec{v}_\lambda \cdot \vec{q}, \tag{E.2}$$

which is the four-moment distribution function around which we will perform the regularization. The transport equations associated with this distribution function are obtained by substituting it into energy and momentum projection of the BTE (Equations (3.1a)-(3.1b)), respectively, which we write below to simplify the present reasoning:

$$\frac{\partial e}{\partial t} + \vec{\nabla} \cdot \vec{q} = 0, \tag{E.3a}$$

$$\frac{\partial \vec{p}}{\partial t} + \vec{\nabla} \cdot \overline{\overline{\Pi}} = \int \hbar \vec{k}_\lambda C(f_\lambda) d\lambda. \tag{E.3b}$$

Then, one obtains:

$$C_v \frac{\partial T}{\partial t} + \vec{\nabla} \cdot \vec{q} = 0, \tag{E.4a}$$

$$\tau \frac{\partial \vec{q}}{\partial t} + \vec{q} = -\kappa \vec{\nabla} T, \tag{E.4b}$$

with τ a time parameter. Equation (E.4b) is the Maxwell-Cattaneo equation (MCE). These two equations are the first-order equations to be used for obtaining the next-order ones.

The first order CE expansion around f_λ^4 can be obtained by isolating the distribution function f_λ from the right-hand side of Equation (E.1) and introducing Equations (E.2)-(E.4b) into the perturbation [164].

$$f_\lambda = f_\lambda^{eq} - \tau_\lambda \left(\frac{\partial f_\lambda}{\partial t} + \vec{v}_\lambda \cdot \vec{\nabla} f_\lambda \right) \Bigg|_{f_\lambda^4}. \tag{E.5}$$

The distribution function thus obtained has the form of

Equation (3.15) with:

$$\vec{\beta}_\lambda = \frac{\tau_\lambda}{\kappa}\frac{\partial f_\lambda^{eq}}{\partial T}\vec{v}_\lambda, \tag{E.6a}$$

$$\vec{\gamma}_\lambda = \frac{\tau_\lambda}{\kappa}(\tau - \tau_\lambda)\frac{\partial f_\lambda^{eq}}{\partial T}\vec{v}_\lambda, \tag{E.6b}$$

$$\overline{\overline{G}}_{1,\lambda} = -\frac{\tau_\lambda^2}{\kappa}\frac{\partial f_\lambda^{eq}}{\partial T}\vec{v}_\lambda\vec{v}_\lambda, \tag{E.6c}$$

$$g_{2,\lambda} = \frac{\tau_\lambda}{C_v}\frac{\partial f_\lambda^{eq}}{\partial T}. \tag{E.6d}$$

These expressions are the same ones supplied in Section 5.1. This distribution reduces to the expression found by Guo and Wang for a gray model and identical Debye branches [57].

To obtain the transport equations associated with this new distribution function, one has to substitute it into Equations (E.3a)-(E.3b). This directly yields equations for the temperature and the heat flux of the form of the GKE, with parameters appearing on the transport equations

$$\kappa = \frac{1}{d}C_v\left\langle v_\lambda^2\tau_\lambda\right\rangle, \tag{E.7a}$$

$$\tau = \frac{\left\langle v_\lambda^2\tau_\lambda^2\right\rangle}{\left\langle v_\lambda^2\tau_\lambda\right\rangle}, \tag{E.7b}$$

$$\ell^2 = \frac{1}{d+2}\frac{\left\langle \frac{v_\lambda^3}{v_{p,\lambda}}\tau_\lambda^2\right\rangle}{\left\langle \frac{v_\lambda}{v_{p,\lambda}}\right\rangle}, \tag{E.7c}$$

$$\tau_e = \tau - \left\langle\tau_\lambda\right\rangle, \tag{E.7d}$$

$$\tau_p^2 = \tau\frac{\left\langle \frac{v_\lambda}{v_{p,\lambda}}\tau_\lambda\right\rangle}{\left\langle \frac{v_\lambda}{v_{p,\lambda}}\right\rangle} - \frac{\left\langle \frac{v_\lambda}{v_{p,\lambda}}\tau_\lambda^2\right\rangle}{\left\langle \frac{v_\lambda}{v_{p,\lambda}}\right\rangle}, \tag{E.7e}$$

$$\alpha = 2 - \frac{d+2}{d}\frac{\left\langle v_\lambda^2\tau_\lambda\right\rangle\left\langle \frac{v_\lambda}{v_{p,\lambda}}\tau_\lambda\right\rangle}{\left\langle \frac{v_\lambda^3}{v_{p,\lambda}}\tau_\lambda^2\right\rangle} - \frac{\kappa\tau_e}{C_v\ell^2}, \tag{E.7f}$$

which are the same expressions obtained in Section 5.1.

Under the assumptions of identical Debye branches and mode-independent relaxation time considered in ref. [57], one recovers the same results found therein.

Callaway's parameters

F

In Section 5.2, we have shown the values of the transport parameters considering Debye's approximation with a single branch for the seek of simplicity. This appendix shows its values for general dispersion relations and number of branches.

$$\tau = \frac{\left\langle v_\lambda^2 \tau_\lambda^2 \right\rangle + A' \left\langle \frac{v_\lambda}{v_{p,\lambda}} \frac{\tau_\lambda^2}{\tau_{N,\lambda}} \right\rangle + B' \left\langle \frac{v_\lambda}{v_{p,\lambda}} \frac{\tau_\lambda}{\tau_{N,\lambda}} \right\rangle}{\left\langle v_\lambda^2 \tau_\lambda \right\rangle + A' \left\langle \frac{v_\lambda}{v_{p,\lambda}} \frac{\tau_\lambda}{\tau_{N,\lambda}} \right\rangle}, \tag{F.1a}$$

$$\ell^2 = \frac{1}{d+2} \frac{\left\langle \frac{v_\lambda^3}{v_{p,\lambda}} \tau_\lambda^2 \right\rangle + A' \left\langle \frac{v_\lambda^2}{v_{p,\lambda}^2} \frac{\tau_\lambda^2}{\tau_{N,\lambda}} \right\rangle}{\left\langle \frac{v_\lambda}{v_{p,\lambda}} \right\rangle}, \tag{F.1b}$$

$$\begin{aligned} \tau_p^2 =& \frac{(\tau A' - B') \left\langle \frac{1}{v_{p,\lambda}^2} \frac{\tau_\lambda}{\tau_{N,\lambda}} \right\rangle - A' \left\langle \frac{1}{v_{p,\lambda}^2} \frac{\tau_\lambda^2}{\tau_{N,\lambda}} \right\rangle}{\left\langle \frac{v_\lambda}{v_{p,\lambda}} \right\rangle} \\ &+ \frac{\tau \left\langle \frac{v_\lambda}{v_{p,\lambda}} \tau_\lambda \right\rangle - \left\langle \frac{v_\lambda}{v_{p,\lambda}} \tau_\lambda^2 \right\rangle}{\left\langle \frac{v_\lambda}{v_{p,\lambda}} \right\rangle}, \end{aligned} \tag{F.1c}$$

$$\tau_e = \frac{\left\langle v_\lambda^2 \tau_\lambda^2 \right\rangle + A' \left\langle \frac{v_\lambda}{v_{p,\lambda}} \frac{\tau_\lambda^2}{\tau_{N,\lambda}} \right\rangle}{\left\langle v_\lambda^2 \tau_\lambda \right\rangle + A' \left\langle \frac{v_\lambda}{v_{p,\lambda}} \frac{\tau_\lambda}{\tau_{N,\lambda}} \right\rangle} - \langle \tau_\lambda \rangle \tag{F.1d}$$

$$\alpha' = 2 - (d+2)\frac{\kappa}{C_v}\frac{\left\langle \frac{v_\lambda}{v_{p,\lambda}}\tau_\lambda \right\rangle}{\left\langle \frac{v_\lambda^3}{v_{p,\lambda}}\tau_\lambda^2 \right\rangle + A'\left\langle \frac{v_\lambda^2}{v_{p,\lambda}^2}\frac{\tau_\lambda^2}{\tau_{N,\lambda}} \right\rangle}. \tag{F.1e}$$

Remember that α is the one of Equation (3.27) ($\alpha \equiv \alpha' - \frac{\kappa\tau_e}{C_v\ell^2}$). The values for A' and B' are shown in Equations (5.12a) and (5.12b), respectively.

Sources in the model G

In this appendix, the introduction of source terms in the transport equations (Equations (3.19a) and (3.19b)) is derived for a general collision operator. The procedure is completely analogous to the one presented in Section 3.3 but introduces into the BTE a term proportional to the introduced source. Section G.1 introduces a power density source into the system. In Section G.2, a flux of momentum is introduced into the system.

G.1 Power density source

As already mentioned, the procedure is completely analogous to the one presented in Section 3.3. However, a term proportional to the power density introduced to the system P is included in the BTE

$$\frac{\partial f_\lambda}{\partial t} + \vec{v}_\lambda \cdot \vec{\nabla} f_\lambda = C(f_\lambda) + p_\lambda P, \tag{G.1}$$

where p_λ is an unknown variable that can depend on the λ-mode. This variable must satisfy that

$$\int \hbar\omega_\lambda p_\lambda d\lambda = 1 \tag{G.2}$$

to guarantee that the density power introduced in a given point is P. By introducing the phonon distribution function related to the GKE (Equation (3.15)), the projection to the

energy of the BTE results in

$$C_v \frac{\partial T}{\partial t} - \tau_e \frac{\partial \vec{\nabla} \cdot \vec{q}}{\partial t} + \vec{\nabla} \cdot \vec{q} = P, \tag{G.3}$$

where it has been used Equation (G.2). The projection to the momentum recovers the expression of Equation (3.19b). By assuming that P is an independent variable and substituting Equations (G.3) and (3.19b) into the BTE, is obtained that

$$\begin{aligned} -\frac{1}{C_v}\frac{\partial f_\lambda^{eq}}{\partial T}\vec{\nabla} \cdot \vec{q} + \frac{1}{C_v}\frac{\partial f_\lambda^{eq}}{\partial T}P \\ +\vec{\beta}_\lambda \cdot \frac{\partial \vec{q}}{\partial t} + \frac{\partial f_\lambda^{eq}}{\partial T}\vec{v}_\lambda \cdot \vec{\nabla}T + \vec{\beta}_\lambda \vec{v}_\lambda : \vec{\nabla}\vec{q} \\ = C(\vec{\beta}_\lambda) \cdot \vec{q} + C(\vec{\gamma}_\lambda) \cdot \frac{\partial \vec{q}}{\partial t} \\ +C\left(\bar{\bar{G}}_\lambda\right) : \vec{\nabla}\vec{q} + C(h_\lambda)\vec{\nabla} \cdot \vec{q} + p_\lambda P, \end{aligned} \tag{G.4}$$

which recovers the expressions from Equations (3.22a)-(3.22d) and it is also obtained the expression for p_λ

$$p_\lambda = \frac{1}{C_v}\frac{\partial f_\lambda^{eq}}{\partial T}. \tag{G.5}$$

This gives that, in general, the BTE is (Equation (G.1))

$$\frac{\partial f_\lambda}{\partial t} + \vec{v}_\lambda \cdot \vec{\nabla} f_\lambda = C(f_\lambda) + \frac{1}{C_v}\frac{\partial f_\lambda^{eq}}{\partial T}P, \tag{G.6}$$

which means that the energy absorption by the system is proportional to the specific heat contribution of the λ-mode. This result agrees with other works, where this mode dependence is *a priori* assumed [32].

G.2 Momentum rate density source

The procedure to obtain the transport equations with a momentum rate density source is completely analogous to the one to obtain the power density source (Section G.1). It is considered that in the BTE, a source term of the momentum rate density $\vec{M}$ is introduced

$$\frac{\partial f_\lambda}{\partial t} + \vec{v}_\lambda \cdot \vec{\nabla} f_\lambda = C(f_\lambda) + p_\lambda P + \vec{m}_\lambda \cdot \vec{M}, \tag{G.7}$$

where $\vec{m}_\lambda$ is an unknown variable that can depend on the λ-mode. This variable must satisfy, in an isotropic material, that

$$\frac{1}{d}\int \hbar k_\lambda m_\lambda d\lambda = 1. \tag{G.8}$$

This relation must be fulfilled to guarantee that the projection of the BTE to the momentum recovers the total momentum rate density $\vec{M}$ introduced. Here we have identified the momentum with the quasi-momentum of the phonons, which is a reasonable approximation to get a physical insight into the momentum source.

If the distribution function considered is the one in Equation (3.15), the projection to the energy of the BTE is the same as in the previous section (Equation (G.3)), and the momentum projection of the BTE is

$$\vec{q} + A_m\vec{M} = -\kappa\vec{\nabla}T - \tau\frac{\partial\vec{q}}{\partial t} + \ell^2\left(\nabla^2\vec{q} + \alpha\vec{\nabla}(\vec{\nabla}\cdot\vec{q})\right), \tag{G.9}$$

where all the parameters are the ones obtained in Section 3.3, and A_m is defined as

$$A_m \equiv \frac{\int \hbar k_\lambda m_\lambda d\lambda}{\int \hbar k_\lambda C(\beta_\lambda) d\lambda}. \tag{G.10}$$

By assuming that $\vec{M}$ is an independent variable and substituting Equations (G.3) and (G.14) into the BTE, it is obtained that (neglecting higher-order derivatives)

$$\begin{aligned} &-\frac{1}{C_v}\frac{\partial f_\lambda^{eq}}{\partial T}\vec{\nabla}\cdot\vec{q} + \frac{1}{C_v}\frac{\partial f_\lambda^{eq}}{\partial T}P + \vec{\beta}_\lambda\cdot\frac{\partial\vec{q}}{\partial t} \\ &\qquad + \frac{\partial f_\lambda^{eq}}{\partial T}\vec{v}_\lambda\cdot\vec{\nabla}T + \vec{\beta}_\lambda\vec{v}_\lambda : \vec{\nabla}\vec{q} \\ &= C(\vec{\beta}_\lambda)\cdot\left(-A_m\vec{M} - \kappa\vec{\nabla}T - \tau\frac{\partial\vec{q}}{\partial t}\right) + C(\vec{\gamma}_\lambda)\cdot\frac{\partial\vec{q}}{\partial t} \\ &\quad + C\left(\bar{\bar{G}}_\lambda\right) : \vec{\nabla}\vec{q} + C(h_\lambda)\vec{\nabla}\cdot\vec{q} + p_\lambda P + \vec{m}_\lambda\cdot\vec{M}, \end{aligned} \tag{G.11}$$

which recovers the expressions from Equations (3.22a)-(3.22d) and Equation (G.5), and it is also obtained the expression for $\vec{m}_\lambda$

$$\vec{m}_\lambda = \frac{d}{C_v\left\langle\frac{v_\lambda}{v_{p,\lambda}}\right\rangle}\frac{\partial f_\lambda^{eq}}{\partial T}\vec{v}_\lambda. \tag{G.12}$$

The parameter A_m is also fully determined by

$$A_m = \frac{1}{d} \frac{\kappa}{C_v \left\langle \frac{v_\lambda}{v_{p,\lambda}} \right\rangle}. \tag{G.13}$$

For example, in a FDTR considered in Section 6.2.1 [66], a semiconductor is directly heated with a monochromatic laser. In that case, the momentum rate density is $\vec{M} = \frac{P}{c}\hat{M}$, where c is the speed of light, P is the power density and $\hat{M}$ is the unitary vector in the laser beam direction. Then, usually, the resulting expression is

$$\vec{q} + A_m \frac{P}{c}\hat{M} = -\kappa\vec{\nabla}T - \tau\frac{\partial\vec{q}}{\partial t} + \ell^2\left(\nabla^2\vec{q} + \alpha\vec{\nabla}(\vec{\nabla}\cdot\vec{q})\right). \tag{G.14}$$

To get a physical insight into the influence of this term, we use the reference values in the second sound experiment for germanium (Section 4.3) [66]. With these values, it is obtained that $q \sim 10^9 A_m M$, meaning that the transfer of momentum due to the photons does not affect the thermal transport since its contribution to thermal transport is various orders of magnitude smaller than the rest of the contributions.

Bibliography

Here are the references in citation order.

[1] Christopher J. Vineis et al. 'Nanostructured Thermoelectrics: Big Efficiency Gains from Small Features'. In: *Advanced Materials* 22.36 (2010), pp. 3970–3980 (cited on page 1).

[2] Gang Zhang and Wenhui Duan. 'Advanced Materials for Heat Energy Transfer, Conversion, Storage and Utilization'. In: *Advanced Functional Materials* 30.8 (2020), p. 1907882 (cited on page 1).

[3] Gordon E. Moore. 'Cramming more components onto integrated circuits'. In: *Electronics* 38.8 (1965), p. 114 (cited on page 1).

[4] M. Mitchell Waldrop. 'The chips are down for Moore's law'. In: *Nature* 530 (2016), p. 144 (cited on page 1).

[5] 'ITRS, International Technology Roadmap for Semiconductors 2.0: Executive Report'. In: *International technology roadmap for semiconductors* 79 (2015) (cited on page 1).

[6] Gang Chen. *Nanoscale energy transport and conversion: a parallel treatment of electrons, molecules, phonons, and photons*. Oxford University Press, 2005 (cited on page 1).

[7] J. M. Ziman. *Principles of the Theory of Solids*. 2nd ed. Cambridge University Press, 1972 (cited on pages 2, 3, 9, 14, 43).

[8] R. Peierls. 'Zur kinetischen Theorie der Wärmeleitung in Kristallen'. In: *Annalen der Physik* 395.8 (1929), pp. 1055–1101 (cited on pages 2, 3, 9, 10).

[9] Jean Baptiste Joseph Fourier. *The Analytical Theory of Heat*. Ed. by AlexanderTranslator Freeman. Cambridge Library Collection - Mathematics. Cambridge University Press, 2009 (cited on page 2).

[10] Yee Kan Koh and David G. Cahill. 'Frequency dependence of the thermal conductivity of semiconductor alloys'. In: *Phys. Rev. B* 76 (7 2007), p. 075207 (cited on pages 2, 88).

[11] Mark E. Siemens et al. 'Quasi-ballistic thermal transport from nanoscale interfaces observed using ultrafast coherent soft X-ray beams'. In: *Nature Materials* 9.1 (2010), pp. 26–30 (cited on pages 2, 8, 68, 70, 83).

[12] A. J. Minnich et al. 'Thermal Conductivity Spectroscopy Technique to Measure Phonon Mean Free Paths'. In: *Phys. Rev. Lett.* 107 (9 2011), p. 095901 (cited on page 2).

[13] Jeremy A. Johnson et al. 'Direct Measurement of Room-Temperature Nondiffusive Thermal Transport Over Micron Distances in a Silicon Membrane'. In: *Phys. Rev. Lett.* 110 (2 2013), p. 025901 (cited on pages 2, 3, 8, 9, 68, 73, 76).

[14] Keith T. Regner et al. 'Broadband phonon mean free path contributions to thermal conductivity measured using frequency domain thermoreflectance'. In: *Nature Communications* 4 (2013), p. 1640 (cited on pages 2, 3, 8, 9, 67, 68, 70, 76, 88).

[15] R. B. Wilson and David G. Cahill. 'Anisotropic failure of Fourier theory in time-domain thermoreflectance experiments.' In: *Nature communications* 5 (2014), p. 5075 (cited on pages 2, 8, 88).

[16] Yongjie Hu et al. 'Spectral mapping of thermal conductivity through nanoscale ballistic transport'. In: *Nature Nanotechnology* 10.8 (2015), pp. 701–706 (cited on pages 2, 3, 8, 68, 70, 84).

[17] Lingping Zeng et al. 'Measuring Phonon Mean Free Path Distributions by Probing Quasiballistic Phonon Transport in Grating Nanostructures'. In: *Scientific Reports* 5.1 (2015), p. 17131 (cited on page 2).

[18] Kathleen M. Hoogeboom-Pot et al. 'A new regime of nanoscale thermal transport: Collective diffusion increases dissipation efficiency'. In: *Proceedings of the National Academy of Sciences* 112.16 (2015), p. 4846 (cited on pages 2, 3, 8, 9, 68, 70, 76, 83, 89).

[19] Takafumi Oyake, Masanori Sakata, and Junichiro Shiomi. 'Nanoscale thermal conductivity spectroscopy by using gold nano-islands heat absorbers'. In: *Applied Physics Letters* 106.7 (2015), p. 073102 (cited on page 2).

[20] Xiangwen Chen et al. 'Quasiballistic Thermal Transport from Nanoscale Heaters and the Role of the Spatial Frequency'. In: *Phys. Rev. Appl.* 10 (5 2018), p. 054068 (cited on page 2).

[21] Travis D. Frazer et al. 'Engineering Nanoscale Thermal Transport: Size- and Spacing-Dependent Cooling of Nanostructures'. In: *Phys. Rev. Applied* 11 (2 2019), p. 024042 (cited on pages 2, 8, 68, 70, 83, 84).

[22] M. Asheghi et al. 'Temperature-Dependent Thermal Conductivity of Single-Crystal Silicon Layers in SOI Substrates'. In: *Journal of Heat Transfer* 120.1 (1998), pp. 30–36 (cited on pages 2, 8, 37, 38, 67–71, 74, 100, 101).

[23] W. Liu and M. Asheghi. 'Phonon–boundary scattering in ultrathin single-crystal silicon layers'. In: *Applied Physics Letters* 84.19 (2004), pp. 3819–3821 (cited on pages 2, 38, 67–71, 100, 101).

[24] Martin Maldovan. 'Micro to nano scale thermal energy conduction in semiconductor thin films'. In: *Journal of Applied Physics* 110.3 (2011), p. 034308 (cited on pages 2, 38, 70).

[25] Ethan A. Scott et al. 'Simultaneous thickness and thermal conductivity measurements of thinned silicon from 100nm to 17m'. In: *Applied Physics Letters* 118.20 (2021), p. 202108 (cited on pages 2, 8).

[26] Ludwig Boltzmann. 'Weitere Studien über das Wärmegleichgewicht unter Gas-molekülen'. In: *Wissenschaftliche Abhandlungen*. Ed. by FriedrichEditor Hasenöhrl. Vol. 1. Cambridge Library Collection - Physical Sciences. Cambridge University Press, 2012, pp. 316–402 (cited on pages 2, 10).

[27] Joseph Callaway. 'Model for Lattice Thermal Conductivity at Low Temperatures'. In: *Phys. Rev.* 113 (4 1959), pp. 1046–1051 (cited on pages 3, 13, 14, 23, 60, 61, 65).

[28] Andrea Cepellotti et al. 'Phonon hydrodynamics in two-dimensional materials'. In: *Nature Communications* 6.1 (2015), p. 6400 (cited on pages 3, 8, 49, 51, 110).

[29] Xun Li and Sangyeop Lee. 'Role of hydrodynamic viscosity on phonon transport in suspended graphene'. In: *Phys. Rev. B* 97 (9 2018), p. 094309 (cited on pages 3, 47).

[30] Denis L. Nika, Artur S. Askerov, and Alexander A. Balandin. 'Anomalous Size Dependence of the Thermal Conductivity of Graphene Ribbons'. In: *Nano Letters* 12.6 (2012), pp. 3238–3244 (cited on page 3).

[31] John Cuffe et al. 'Reconstructing phonon mean-free-path contributions to thermal conductivity using nanoscale membranes'. In: *Phys. Rev. B* 91 (24 2015), p. 245423 (cited on pages 3, 36, 73, 103).

[32] Bjorn Vermeersch et al. 'Superdiffusive heat conduction in semiconductor alloys. I. Theoretical foundations'. In: *Phys. Rev. B* 91 (8 2015), p. 085202 (cited on pages 3, 13, 16, 33, 126).

[33] Vazrik Chiloyan et al. 'Variational approach to solving the spectral Boltzmann transport equation in transient thermal grating for thin films'. In: *Journal of Applied Physics* 120.2 (2016), p. 025103 (cited on page 3).

[34] Chengyun Hua and Austin J. Minnich. 'Heat dissipation in the quasiballistic regime studied using the Boltzmann equation in the spatial frequency domain'. In: *Phys. Rev. B* 97 (2018), p. 014307 (cited on page 3).

[35] Chengyun Hua et al. 'Generalized Fourier's law for nondiffusive thermal transport: Theory and experiment'. In: *Phys. Rev. B* 100 (2019), p. 085203 (cited on pages 3, 9, 13, 16, 33, 57).

[36] Andrea Cepellotti and Nicola Marzari. 'Boltzmann Transport in Nanostructures as a Friction Effect'. In: *Nano Letters* 17 (2017) (cited on pages 3, 8).

[37] D. A. Broido, A. Ward, and N. Mingo. 'Lattice thermal conductivity of silicon from empirical interatomic potentials'. In: *Phys. Rev. B* 72 (1 2005), p. 014308 (cited on pages 3, 15, 16, 23, 24, 29, 42).

[38] D. A. Broido et al. 'Intrinsic lattice thermal conductivity of semiconductors from first principles'. In: *Applied Physics Letters* 91.23 (2007), p. 231922 (cited on pages 3, 15).

[39] Laurent Chaput. 'Direct Solution to the Linearized Phonon Boltzmann Equation'. In: *Phys. Rev. Lett.* 110 (26 2013), p. 265506 (cited on page 3).

[40] Wu Li et al. 'ShengBTE: A solver of the Boltzmann transport equation for phonons'. In: *Computer Physics Communications* 185.6 (2014), pp. 1747–1758 (cited on page 3).

[41] Andrea Cepellotti and Nicola Marzari. 'Thermal Transport in Crystals as a Kinetic Theory of Relaxons'. In: *Phys. Rev. X* 6 (4 2016), p. 041013 (cited on pages 3, 4, 9).

[42] Zhiwei Ding et al. 'Phonon Hydrodynamic Heat Conduction and Knudsen Minimum in Graphite'. In: *Nano Letters* 18.1 (2018). PMID: 29236507, pp. 638–649 (cited on pages 3, 8).

[43] Michele Simoncelli, Nicola Marzari, and Andrea Cepellotti. 'Generalization of Fourier's Law into Viscous Heat Equations'. In: *Phys. Rev. X* 10 (1 2020), p. 011019 (cited on pages 3–6, 23, 33, 43, 56, 65, 110).

[44] Giuseppe Romano. *OpenBTE: a Solver for ab-initio Phonon Transport in Multidimensional Structures*. 2021. URL: https://arxiv.org/abs/2106.02764 (cited on page 3).

[45] David Lacroix, Karl Joulain, and Denis Lemonnier. 'Monte Carlo transient phonon transport in silicon and germanium at nanoscales'. In: *Phys. Rev. B* 72 (6 2005), p. 064305 (cited on page 3).

[46] Jean-Philippe M. Péraud and Nicolas G. Hadjiconstantinou. 'Efficient simulation of multidimensional phonon transport using energy-based variance-reduced Monte Carlo formulations'. In: *Phys. Rev. B* 84 (20 2011), p. 205331 (cited on pages 3, 33, 36).

[47] Jean-Philippe M. Péraud and Nicolas G. Hadjiconstantinou. 'An alternative approach to efficient simulation of micro/nanoscale phonon transport'. In: *Applied Physics Letters* 101.15 (2012), p. 153114 (cited on page 3).

[48] Jean-Philippe M. Péraud and Nicolas G. Hadjiconstantinou. 'Extending the range of validity of Fourier's law into the kinetic transport regime via asymptotic solution of the phonon Boltzmann transport equation'. In: *Phys. Rev. B* 93 (4 2016), p. 045424 (cited on page 3).

[49] Martí Raya-Moreno, Xavier Cartoixà, and Jesús Carrete. 'BTE-Barna: An extension of almaBTE for thermal simulation of devices based on 2D materials'. In: *Computer Physics Communications* 281 (2022), p. 108504 (cited on page 3).

[50] Martı Raya-Moreno, Jesús Carrete, and Xavier Cartoixà. 'Hydrodynamic signatures in thermal transport in devices based on two-dimensional materials: An ab initio study'. In: *Phys. Rev. B* 106 (2022), p. 014308 (cited on page 3).

[51] Giuseppe Romano et al. 'Temperature-dependent thermal conductivity in silicon nanostructured materials studied by the Boltzmann transport equation'. In: *Phys. Rev. B* 93 (3 2016), p. 035408 (cited on pages 3, 9, 76).

[52] R. A. Guyer and J. A. Krumhansl. 'Solution of the Linearized Phonon Boltzmann Equation'. In: *Phys. Rev.* 148 (2 1966), pp. 766–778 (cited on pages 3, 5–7, 16–21, 23, 33, 35, 36, 43, 45–48, 50, 55, 60, 102, 111, 112).

[53] Yanbao Ma. 'A two-parameter nondiffusive heat conduction model for data analysis in pump-probe experiments'. In: *Journal of Applied Physics* 116.24 (2014), p. 243505 (cited on page 3).

[54] Sangyeop Lee et al. 'Hydrodynamic phonon transport in suspended graphene'. In: *Nature Communications* 6.1 (2015), p. 6290 (cited on pages 3, 4, 8, 29, 44, 46, 49, 51, 110).

[55] Sangyeop Lee and Lucas Lindsay. 'Hydrodynamic phonon drift and second sound in a (20,20) single-wall carbon nanotube'. In: *Phys. Rev. B* 95 (18 2017), p. 184304 (cited on pages 3, 8, 49–52, 54).

[56] Zhengxian Qu, Dadong Wang, and Yanbao Ma. 'Non-diffusive thermal transport and prediction of the breakdown of Fourier's law in nanograting experiments'. In: *AIP Advances* 7.1 (2017), p. 015108 (cited on page 3).

[57] Yangyu Guo and Moran Wang. 'Phonon hydrodynamics for nanoscale heat transport at ordinary temperatures'. In: *Phys. Rev. B* 97 (3 2018), p. 035421 (cited on pages 3, 5, 19, 22, 23, 36, 40, 41, 43, 57, 58, 119, 121, 122).

[58] Amirkoushyar Ziabari et al. 'Full-field thermal imaging of quasiballistic crosstalk reduction in nanoscale devices'. In: *Nature Communications* 9.1 (2018), p. 255 (cited on pages 3, 5, 6, 8, 20, 21, 67, 68, 77–79, 96).

[59] P. Torres et al. 'Emergence of hydrodynamic heat transport in semiconductors at the nanoscale'. In: *Phys. Rev. Materials* 2 (7 2018), p. 076001 (cited on pages 3, 5, 6, 20, 21, 41).

[60] Yo Machida et al. 'Observation of Poiseuille flow of phonons in black phosphorus'. In: *Science Advances* 4.6 (2018), eaat3374 (cited on pages 3, 8).

[61] S. Huberman et al. 'Observation of second sound in graphite at temperatures above 100 K'. In: *Science* 364.6438 (2019), pp. 375–379 (cited on pages 3, 8, 49, 91).

[62] A. Beardo et al. 'Hydrodynamic Heat Transport in Compact and Holey Silicon Thin Films'. In: *Phys. Rev. Applied* 11 (3 2019), p. 034003 (cited on pages 3, 5, 6, 20, 21, 37–39, 41, 68, 71–73, 80, 86, 94–97, 104).

[63] A. Beardo et al. 'Phonon hydrodynamics in frequency-domain thermoreflectance experiments'. In: *Phys. Rev. B* 101 (7 2020), p. 075303 (cited on pages 3, 5, 6, 8, 20, 21, 36, 38, 40, 80, 88–90, 95).

[64] Sami Alajlouni et al. 'Geometrical quasi-ballistic effects on thermal transport in nanostructured devices'. In: *Nano Research* 14.4 (2021), pp. 945–952 (cited on pages 3, 5, 6, 38–40, 67, 77–82, 95).

[65] Albert Beardo et al. 'A General and Predictive Understanding of Thermal Transport from 1D- and 2D-Confined Nanostructures: Theory and Experiment'. In: *ACS Nano* 15.8 (2021). PMID: 34328719, pp. 13019–13030 (cited on pages 3, 5, 6, 8, 20, 21, 38–40, 67, 83–87, 92, 95–97, 99).

[66] Albert Beardo et al. 'Observation of second sound in a rapidly varying temperature field in Ge'. In: *Science Advances* 7.27 (2021), eabg4677 (cited on pages 3, 5, 6, 8, 38–40, 49, 67, 90, 92, 93, 95, 128).

[67] Albert Beardo et al. 'Hydrodynamic thermal transport in silicon at temperatures ranging from 100 to 300 K'. In: *Phys. Rev. B* 105 (16 2022), p. 165303 (cited on pages 3, 5, 6, 8, 20, 21, 38, 67, 77, 78, 82, 95, 97, 98).

[68] Bolin Liao, ed. *Nanoscale Energy Transport*. 2053-2563. IOP Publishing, 2020 (cited on page 4).

[69] Robert J. Hardy. 'Phonon Boltzmann Equation and Second Sound in Solids'. In: *Phys. Rev. B* 2 (4 1970), pp. 1193–1207 (cited on pages 4, 23, 43, 48–51, 55, 91, 92).

[70] Lluc Sendra et al. 'Derivation of a hydrodynamic heat equation from the phonon Boltzmann equation for general semiconductors'. In: *Phys. Rev. B* 103 (14 2021), p. L140301 (cited on pages 5, 6, 23, 24, 31, 56, 57, 60, 65, 67, 69, 74, 94, 98, 102, 103, 109, 119).

[71] C. de Tomas et al. 'From kinetic to collective behavior in thermal transport on semiconductors and semiconductor nanostructures'. In: *Journal of Applied Physics* 115.16 (2014), p. 164314 (cited on pages 5, 20).

[72] C. de Tomas et al. 'Enhancing of optic phonon contribution in hydrodynamic phonon transport'. In: *Journal of Applied Physics* 118.13 (2015), p. 134305 (cited on pages 5, 20).

[73] P. Torres et al. 'First principles kinetic-collective thermal conductivity of semiconductors'. In: *Phys. Rev. B* 95 (16 2017), p. 165407 (cited on pages 5, 19–21).

[74] R. A. Guyer and J. A. Krumhansl. 'Thermal Conductivity, Second Sound, and Phonon Hydrodynamic Phenomena in Nonmetallic Crystals'. In: *Phys. Rev.* 148 (2 1966), pp. 778–788 (cited on pages 6, 16, 23, 35, 43, 46, 48, 49, 65, 91).

[75] David Jou, Casas-Vázquez José, and Georgy Lebon. *Extended Irreversible Thermodynamics*. 1996 (cited on pages 6, 23).

[76] M. Asheghi et al. 'Thermal conduction in doped single-crystal silicon films'. In: *Journal of Applied Physics* 91.8 (2002), pp. 5079–5088 (cited on pages 8, 38, 67–69, 71, 100, 101).

[77] Yo Machida et al. 'Phonon hydrodynamics and ultrahigh-room-temperature thermal conductivity in thin graphite'. In: *Science* 367.6475 (2020), pp. 309–312 (cited on page 8).

[78] Ashutosh Giri and Patrick E. Hopkins. 'A Review of Experimental and Computational Advances in Thermal Boundary Conductance and Nanoscale Thermal Transport across Solid Interfaces'. In: *Advanced Functional Materials* 30.8 (2020), p. 1903857 (cited on pages 8, 70).

[79] A. A. Maznev, Jeremy A. Johnson, and Keith A. Nelson. 'Onset of nondiffusive phonon transport in transient thermal grating decay'. In: *Phys. Rev. B* 84 (19 2011), p. 195206 (cited on pages 9, 76).

[80] Kimberlee C. Collins et al. 'Non-diffusive relaxation of a transient thermal grating analyzed with the Boltzmann transport equation'. In: *Journal of Applied Physics* 114.10 (2013), p. 104302 (cited on pages 9, 76).

[81] Sebastian Volz et al. 'Transient Fourier-law deviation by molecular dynamics in solid argon'. In: *Phys. Rev. B* 54 (1 1996), pp. 340–347 (cited on page 9).

[82] Sebastian G. Volz and Gang Chen. 'Molecular-dynamics simulation of thermal conductivity of silicon crystals'. In: *Phys. Rev. B* 61 (4 2000), pp. 2651–2656 (cited on page 9).

[83] Patrick K. Schelling, Simon R. Phillpot, and Pawel Keblinski. 'Phonon wave-packet dynamics at semiconductor interfaces by molecular-dynamics simulation'. In: *Applied Physics Letters* 80 (2002), pp. 2484–2486 (cited on page 9).

[84] A.J.H. McGaughey and M. Kaviany. 'Phonon Transport in Molecular Dynamics Simulations: Formulation and Thermal Conductivity Prediction'. In: ed. by George A. Greene et al. Vol. 39. Advances in Heat Transfer. Elsevier, 2006, pp. 169–255 (cited on page 9).

[85] D. P. Sellan et al. 'Size effects in molecular dynamics thermal conductivity predictions'. In: *Phys. Rev. B* 81 (21 2010), p. 214305 (cited on page 9).

[86] Arthur France-Lanord et al. 'Thermal properties of amorphous/crystalline silicon superlattices'. In: *Journal of Physics: Condensed Matter* 26.35 (2014), p. 355801 (cited on page 9).

[87] Lina Yang, Nuo Yang, and Baowen Li. 'Extreme Low Thermal Conductivity in Nanoscale 3D Si Phononic Crystal with Spherical Pores'. In: *Nano Letters* 14.4 (2014). PMID: 24559126, pp. 1734–1738 (cited on page 9).

[88] Maxime Verdier, David Lacroix, and Konstantinos Termentzidis. 'Thermal transport in two- and three-dimensional nanowire networks'. In: *Phys. Rev. B* 98 (2018), p. 155434 (cited on page 9).

[89] Donatas Surblys et al. 'Application of atomic stress to compute heat flux via molecular dynamics for systems with many-body interactions'. In: *Phys. Rev. E* 99 (2019), p. 051301 (cited on page 9).

[90] J.M. Ziman. *Electrons and Phonons: The Theory of Transport Phenomena in Solids*. 2001 (cited on pages 9, 11, 14, 19, 37, 44, 53).

[91] R.K. Pathria and P.D. Beale. *Statistical Mechanics*. 4th ed. Elsevier, 2021 (cited on page 9).

[92] Tianli Feng, Lucas Lindsay, and Xiulin Ruan. 'Four-phonon scattering significantly reduces intrinsic thermal conductivity of solids'. In: *Phys. Rev. B* 96 (16 2017), p. 161201 (cited on page 11).

[93] Navaneetha K. Ravichandran and David Broido. 'Phonon-Phonon Interactions in Strongly Bonded Solids: Selection Rules and Higher-Order Processes'. In: *Phys. Rev. X* 10 (2 2020), p. 021063 (cited on page 11).

[94] Yanguang Zhou and Ming Hu. 'Full quantification of frequency-dependent interfacial thermal conductance contributed by two- and three-phonon scattering processes from nonequilibrium molecular dynamics simulations'. In: *Phys. Rev. B* 95 (11 2017), p. 115313 (cited on page 11).

[95] A. Ward and D. A. Broido. 'Intrinsic phonon relaxation times from first-principles studies of the thermal conductivities of Si and Ge'. In: *Phys. Rev. B* 81 (8 2010), p. 085205 (cited on pages 12, 57).

[96] D. G. Onn et al. 'Some aspects of the thermal conductivity of isotopically enriched diamond single crystals'. In: *Phys. Rev. Lett.* 68 (18 1992), pp. 2806–2809 (cited on page 13).

[97] V. I. Ozhogin et al. 'Isotope effect in the thermal conductivity of germanium single crystals'. In: *Journal of Experimental and Theoretical Physics Letters* 63.6 (1996), pp. 490–494 (cited on page 13).

[98] A. V. Inyushkin et al. 'On the isotope effect in thermal conductivity of silicon'. In: *physica status solidi (c)* 1.11 (2004), pp. 2995–2998 (cited on page 13).

[99] P. Klemens. *Solid State Physics*. Academic Press, 1958 (cited on pages 14, 44).

[100] H.E. Hall. *Solid state physics*. 4th ed. John Wiley & Sons, 1974 (cited on page 14).

[101] M Omini and A Sparavigna. 'An iterative approach to the phonon Boltzmann equation in the theory of thermal conductivity'. In: *Physica B: Condensed Matter* 212.2 (1995), pp. 101–112 (cited on page 15).

[102] M. Omini and A. Sparavigna. 'Beyond the isotropic-model approximation in the theory of thermal conductivity'. In: *Phys. Rev. B* 53 (14 1996), pp. 9064–9073 (cited on page 15).

[103] A. Ward et al. 'Ab initio theory of the lattice thermal conductivity in diamond'. In: *Phys. Rev. B* 80 (12 2009), p. 125203 (cited on page 15).

[104] Yangyu Guo and Moran Wang. 'Phonon hydrodynamics and its applications in nanoscale heat transport'. In: *Physics Reports* 595 (2015), pp. 1–44 (cited on pages 19, 23, 36).

[105] W. Dreyer and Henning Struchtrup. 'Heat pulse experiments revisited'. In: *Continuum Mechanics and Thermodynamics* 5 (1993), pp. 3–50 (cited on pages 19, 23).

[106] Michael Fryer and Henning Struchtrup. 'Moment model and boundary conditions for energy transport in the phonon gas'. In: *Continuum Mechanics and Thermodynamics* 26 (2013), pp. 39– (cited on pages 19, 23, 43).

[107] Sydney Chapman and T. G. Cowling. *The Mathematical Theory of Non-uniform Gases. An Account of the Kinetic Theory of Viscosity, Thermal Conduction and Diffusion in Gases*. 1953 (cited on pages 21, 25).

[108] Harold Grad. *On the Kinetic Theory of Rarefied Gases*. 1949 (cited on pages 21, 25, 36).

[109] H. Struchtrup. *Macroscopic transport equations for rarefied gas flows*. Springer, 2005 (cited on pages 22, 25, 119).

[110] Vazrik Chiloyan et al. 'Green's functions of the Boltzmann transport equation with the full scattering matrix for phonon nanoscale transport beyond the relaxation-time approximation'. In: *Phys. Rev. B* 104 (24 2021), p. 245424 (cited on page 23).

[111] J Sussmann and A Thellung. 'Thermal Conductivity of Perfect Dielectric Crystals in the Absence of Umklapp Processes'. In: *Proceedings of the Physical Society* 81 (1963), p. 1122 (cited on pages 23, 43).

[112] Robert J. Hardy and Dennis L. Albers. 'Hydrodynamic approximation to the phonon Boltzmann equation'. In: *Phys. Rev. B* 10 (8 1974), pp. 3546–3551 (cited on pages 23, 34, 36, 43, 48).

[113] R. Gurzhi. 'Thermal conductivity of dielectrics and ferrodielectrics at low temperatures'. In: *J. Exp. Theor. Phys.* 19.2 (1964), pp. 719–724 (cited on pages 23, 43).

[114] Xiaokun Gu et al. 'Colloquium: Phononic thermal properties of two-dimensional materials'. In: *Rev. Mod. Phys.* 90 (4 2018), p. 041002 (cited on pages 25, 69, 110, 111).

[115] Colin D Landon and Nicolas G Hadjiconstantinou. 'Deviational simulation of phonon transport in graphene ribbons with ab initio scattering'. In: *Journal of Applied Physics* 116.16 (2014), p. 163502 (cited on page 36).

[116] Giorgia Fugallo et al. 'Thermal Conductivity of Graphene and Graphite: Collective Excitations and Mean Free Paths'. In: *Nano Letters* 14.11 (2014), pp. 6109–6114 (cited on page 36).

[117] Manuel Torrilhon and Henning Struchtrup. 'Boundary conditions for regularized 13-moment-equations for micro-channel-flows'. In: *Journal of Computational Physics* 227.3 (2008), pp. 1982–2011 (cited on page 36).

[118] P. L. Kapitza. 'Heat Transfer and Superfluidity of Helium II'. In: *Phys. Rev.* 60 (4 1941), pp. 354–355 (cited on page 40).

[119] E. T. Swartz and R. O. Pohl. 'Thermal boundary resistance'. In: *Rev. Mod. Phys.* 61 (3 1989), pp. 605–668 (cited on page 40).

[120] F. X. Alvarez, D. Jou, and A. Sellitto. 'Phonon hydrodynamics and phonon-boundary scattering in nanosystems'. In: *Journal of Applied Physics* 105.1 (2009), p. 014317 (cited on page 41).

[121] Lluc Sendra et al. 'Hydrodynamic heat transport in dielectric crystals in the collective limit and the drifting/driftless velocity conundrum'. In: *Phys. Rev. B* 106 (15 2022), p. 155301 (cited on pages 43, 49, 51–53, 55, 102).

[122] Howard E. Jackson, Charles T. Walker, and Thomas F. McNelly. 'Second Sound in NaF'. In: *Phys. Rev. Lett.* 25 (1 1970), pp. 26–28 (cited on page 49).

[123] V. Narayanamurti and R. C. Dynes. 'Observation of Second Sound in Bismuth'. In: *Phys. Rev. Lett.* 28 (22 1972), pp. 1461–1465 (cited on pages 49, 91).

[124] Dieter W. Pohl and V. Irniger. 'Observation of Second Sound in NaF by Means of Light Scattering'. In: *Phys. Rev. Lett.* 36 (9 1976), pp. 480–483 (cited on page 49).

[125] Zhiwei Ding et al. 'Observation of second sound in graphite over 200 K'. In: *Nature Communications* 13.1 (2022), p. 285 (cited on page 49).

[126] Xiao-Ping Luo et al. 'Direct simulation of second sound in graphene by solving the phonon Boltzmann equation via a multiscale scheme'. In: *Phys. Rev. B* 100 (15 2019), p. 155401 (cited on pages 52, 110).

[127] R. Peierls. *Quantum Theory of Solids*. Oxford University Press, 1955 (cited on page 53).

[128] David Song and Gang Chen. 'Thermal conductivity of periodic microporous silicon films'. In: *Applied Physics Letters* 84.5 (2004), pp. 687–689 (cited on pages 67, 70).

[129] K. T. Regner, S. Majumdar, and J. A. Malen. 'Instrumentation of broadband frequency domain thermoreflectance for measuring thermal conductivity accumulation functions'. In: *Review of Scientific Instruments* 84.6 (2013), p. 064901 (cited on pages 67, 88).

[130] Zeyu Xiang, Puqing Jiang, and Ronggui Yang. 'Time-domain thermoreflectance (TDTR) data analysis using phonon hydrodynamic model'. In: *Journal of Applied Physics* 132.20 (2022), p. 205104 (cited on pages 67, 94, 96).

[131] Albert Beardo Ricol, dir. Alvarez Calafell Francesc Xavier, and dir. Bafaluy Bafaluy Javier. 'Generalized Hydrodynamic Heat Transport in Semiconductors'. PhD thesis. 2021. DOI: http://hdl.handle.net/10803/673590 (cited on pages 67, 68, 90, 92, 94, 95).

[132] O.C. Zienkiewicz, R.L. Taylor, and J.Z. Zhu, eds. *The Finite Element Method: Its Basis and Fundamentals*. Seventh Edition. Oxford: Butterworth-Heinemann, 2013, p. iii (cited on page 68).

[133] Samuel Huberman et al. 'Unifying first-principles theoretical predictions and experimental measurements of size effects in thermal transport in SiGe alloys'. In: *Phys. Rev. Materials* 1 (5 2017), p. 054601 (cited on page 68).

[134] Changwook Jeong, Supriyo Datta, and Mark Lundstrom. 'Thermal conductivity of bulk and thin-film silicon: A Landauer approach'. In: *Journal of Applied Physics* 111.9 (2012), p. 93708 (cited on page 70).

[135] Puqing Jiang, Lucas Lindsay, and Yee Kan Koh. 'Role of low-energy phonons with mean-free-paths >0.8 μm in heat conduction in silicon'. In: *Journal of Applied Physics* 119.24 (2016), p. 245705 (cited on page 70).

[136] A. Sellitto, I. Carlomagno, and D. Jou. 'Two-dimensional phonon hydrodynamics in narrow strips'. In: *Proceedings of the Royal Society A: Mathematical, Physical and Engineering Sciences* 471.2182 (2015), p. 20150376 (cited on pages 73, 75, 100).

[137] Amirkoushyar Ziabari et al. 'Far-field thermal imaging below diffraction limit'. In: *Opt. Express* 28.5 (2020), pp. 7036–7050 (cited on page 77).

[138] Chengyun Hua et al. 'Experimental metrology to obtain thermal phonon transmission coefficients at solid interfaces'. In: *Phys. Rev. B* 95 (20 2017), p. 205423 (cited on page 82).

[139] Jun Liu et al. 'Simultaneous measurement of thermal conductivity and heat capacity of bulk and thin film materials using frequency-dependent transient thermoreflectance method'. In: *Review of Scientific Instruments* 84.3 (2013), p. 034902 (cited on page 88).

[140] David Rodin and Shannon K. Yee. 'Simultaneous measurement of in-plane and through-plane thermal conductivity using beam-offset frequency domain thermoreflectance'. In: *Review of Scientific Instruments* 88.1 (2017), p. 014902 (cited on page 88).

[141] Jeffrey L. Braun et al. 'A steady-state thermoreflectance method to measure thermal conductivity'. In: *Review of Scientific Instruments* 90.2 (2019), p. 024905 (cited on page 88).

[142] Marvin Chester. 'Second Sound in Solids'. In: *Phys. Rev.* 131 (5 1963), pp. 2013–2015 (cited on page 91).

[143] Marco Gandolfi et al. 'Accessing temperature waves: A dispersion relation perspective'. In: *International Journal of Heat and Mass Transfer* 143 (Aug. 2019), p. 118553 (cited on page 91).

[144] Akitoshi Koreeda, Ryuta Takano, and Seishiro Saikan. 'Second Sound in $SrTiO_3$'. In: *Phys. Rev. Lett.* 99 (26 2007), p. 265502 (cited on page 91).

[145] Alejandra Ruiz-Clavijo et al. '3D Bi2Te3 Interconnected Nanowire Networks to Increase Thermoelectric Efficiency'. In: *ACS Applied Energy Materials* 4.12 (2021), pp. 13556–13566 (cited on page 96).

[146] Claudio Melis et al. 'Indications of Phonon Hydrodynamics in Telescopic Silicon Nanowires'. In: *Phys. Rev. Appl.* 11 (5 2019), p. 054059 (cited on page 96).

[147] Paul Desmarchelier et al. 'Atomistic evidence of hydrodynamic heat transfer in nanowires'. In: *International Journal of Heat and Mass Transfer* 194 (2022), p. 123003 (cited on page 96).

[148] Hossein Honarvar et al. 'Directional thermal channeling: A phenomenon triggered by tight packing of heat sources'. In: *Proceedings of the National Academy of Sciences* 118.40 (2021), e2109056118 (cited on page 99).

[149] P. Torres. *Kinetic Collective Model*. URL: https://physta.github.io/ (cited on page 107).

[150] G. Kresse and J. Hafner. 'Ab initio molecular dynamics for liquid metals'. In: *Phys. Rev. B* 47 (1 1993), pp. 558–561 (cited on page 107).

[151] G. Kresse and J. Hafner. 'Ab initio molecular-dynamics simulation of the liquid-metal–amorphous-semiconductor transition in germanium'. In: *Phys. Rev. B* 49 (20 1994), pp. 14251–14269 (cited on page 107).

[152] G. Kresse and J. Furthmüller. 'Efficiency of ab-initio total energy calculations for metals and semiconductors using a plane-wave basis set'. In: *Comp. Mat. Sci.* 6 (1 1996), pp. 15–50 (cited on page 107).

[153] G. Kresse and J. Furthmüller. 'Efficient iterative schemes for ab initio total-energy calculations using a plane-wave basis set'. In: *Phys. Rev. B* 54 (16 1996), pp. 11169–11186 (cited on page 107).

[154] P. E. Blöchl. 'Projector augmented-wave method'. In: *Phys. Rev. B* 50 (24 1994), pp. 17953–17979 (cited on page 107).

[155] John P. Perdew, Kieron Burke, and Matthias Ernzerhof. 'Generalized Gradient Approximation Made Simple'. In: *Phys. Rev. Lett.* 77 (18 1996), pp. 3865–3868 (cited on page 107).

[156] A Togo and I Tanaka. 'First principles phonon calculations in materials science'. In: *Scr. Mater.* 108 (2015), pp. 1–5 (cited on page 107).

[157] Atsushi Togo, Laurent Chaput, and Isao Tanaka. 'Distributions of phonon lifetimes in Brillouin zones'. In: *Phys. Rev. B* 91 (9 2015), p. 094306 (cited on page 107).

[158] Pol Torres et al. 'Descriptors of intrinsic hydrodynamic thermal transport: screening a phonon database in a machine learning approach'. In: *Journal of Physics: Condensed Matter* 34.13 (2022), p. 135702 (cited on page 107).

[159] Eros Mariani and Felix von Oppen. 'Erratum: Flexural Phonons in Free-Standing Graphene [Phys. Rev. Lett. 100, 076801 (2008)]'. In: *Phys. Rev. Lett.* 100 (24 2008), p. 249901 (cited on page 110).

[160] Arnab K. Majee and Zlatan Aksamija. 'Length divergence of the lattice thermal conductivity in suspended graphene nanoribbons'. In: *Phys. Rev. B* 93 (23 2016), p. 235423 (cited on page 110).

[161] Man-Yu Shang et al. 'Unified theory of second sound in two-dimensional materials'. In: *Phys. Rev. B* 105 (16 2022), p. 165423 (cited on pages 110, 111).

[162] A. H. Castro Neto et al. 'The electronic properties of graphene'. In: *Rev. Mod. Phys.* 81 (1 2009), pp. 109–162 (cited on page 111).

[163] Youdi Kuang et al. 'Thermal conductivity of graphene mediated by strain and size'. In: *International Journal of Heat and Mass Transfer* 101 (2016), pp. 772–778 (cited on page 111).

[164] W. G. Vincenti and C. H. Krüger Jr. *Introduction to Physical Gas Dynamics*. John Wiley & Sons, 1965 (cited on page 120).

Acronyms

B

BTE Boltzmann Transport Equation. ix, 2–6, 9–12, 16, 17, 21, 22, 24–28, 32, 36, 42, 44, 49–53, 56, 68, 73, 80, 102, 103, 110, 112, 114, 119, 120, 125–127

C

CE Chapman-Enskog. 21, 25, 119, 120

D

DMM Diffuse mismatch model. 40, 80, 82, 88, 89

E

EIT Extended Irreversible Thermodynamics. 6, 23

EUV Extreme ultraviolet. xii, 83, 85

F

FDF Flux derivatives Formalism. x, 6, 7, 22–25, 42–44, 49, 52–56, 60, 65, 67–100, 102–104, 111, 114, 115, 119

FDTR Frequency-domain thermoreflectance. xii, 67, 70, 88–90, 92, 94, 95, 103, 128

FEM Finite-element methods. 67, 68, 77, 80, 90, 103

G

GKE Guyer-Krumhansl equation. xi–xiii, 5–7, 12, 18–20, 22, 24, 30, 31, 33, 35, 36, 41, 43, 47, 49, 52, 56, 57, 59, 60, 62, 65, 67–77, 80–90, 92, 94, 96–104, 111, 119–122, 125

K

KCM Kinetic-Collective Model. ix, xii, 5, 19–21, 58, 59

M

MCE Maxwell-Cattaneo equation. 91–93, 120

MFP Mean-free path. xii, 3, 9, 20, 58, 68, 69, 73, 74, 76, 88, 92, 98, 99

N

NSE Navier-Stokes equation. 5, 18, 41, 47, 96

R

RTA Relaxation Time Approximation. xii, xiii, 3, 7, 12, 13, 15, 16, 19, 22, 23, 25, 29, 33, 40, 43, 55–59, 61–65, 73, 74, 76, 101, 103, 107, 109, 115, 119

T

TBR Thermal boundary resistance. 8, 68, 84, 87–90
TDTR Time-domain thermoreflectance. 68, 94, 96
TRI Thermoreflectance imaging. 77, 78, 80, 82